Title

Additive Microfabrication with Holographic Optical Tweezers

Author

Shaw, Lucas

Publication Date

2018

UNIVERSITY OF CALIFORNIA

Los Angeles

Additive Microfabrication with Holographic Optical Tweezers

A dissertation submitted in partial satisfaction of the requirements for the degree Doctor of Philosophy in Mechanical Engineering

by

Lucas Andrew Shaw

2018

ABSTRACT OF THE DISSERTATION

Additive Microfabrication with Holographic Optical Tweezers

by

Lucas Andrew Shaw

Doctor of Philosophy in Mechanical Engineering

University of California, Los Angeles, 2018

Professor Jonathan B. Hopkins, Chair

The purpose of this research is to increase the speed with which holographic optical tweezers (HOT) can individually assemble microscale particles for fabricating useful volumes of mechanical metamaterials in reasonable build times. HOT systems are unique among other additive manufacturing approaches in their ability to create true-3D structures with multiple materials, microscale features, and overhanging geometries. To scale up HOT-based fabrication, this research focuses on four primary goals: *(1)* scaling the number of particles that can be handled simultaneously using scanning holographic optical tweezers (SHOT), *(2)* developing efficient path planning and automation algorithms for efficiently delivering particles to their destinations within the fabricated structure, *(3)* modeling the dynamics of discretely-stepped optically-trapped particles to reliably handle them at high speeds, and *(4)* efficiently joining adjacent particles to produce a permanent structure. In addition, this work also demonstrates a proof-of-concept system that combines the HOT approach with the two-photon lithography approach, which allows for simultaneous fabrication and manipulation of microscale mechanisms in the same system for the first time. By improving the number and speed of particles that can be handled with the HOT approach, this work provides a promising path towards automated and scalable manufacturing of materials with extraordinary properties, such as microgranular lattices or microstructures with embedded strain energy.

The dissertation of Lucas Andrew Shaw is approved.

Robert N. Candler

James S. Gibson

Tsu-Chin Tsao

Jonathan Hopkins, Committee Chair

University of California, Los Angeles

2018

Dedicated to Mom and Dad.

Table of Contents

List of Figures

List of Tables

Acknowledgments

I would like to dedicate this dissertation…

To my loving mother and father, who taught me the meaning of hard work and unconditional love. You gave me every opportunity to succeed and I am eternally grateful for the rationality, sense of humor, and life balance that you raised me with.

To my supportive advisor Jonathan Hopkins, whose trust gave me ample room to grow as a young and confident researcher, whose encouragement motivated me to keep learning, and whose excitement empowered me to love my work.

To my lab mates, especially Samira Chizari, James Simonelli, Adam Song, and Mike Porter, who made our small space in Boelter Hall an enjoyable and fulfilling environment in which to experiment and learn.

To my mentors and role models – Maxim Shusteff, Bob Panas, Chris Burgner, and Kimberly Turner – the confidence, positive attitudes, and tenacity that you radiated inspired me to want to be like you: the kind of person that can solve any problem that's thrown your way.

To Harsha Kittur, Sara Azzam, and Will Herrera, whose generosity and kindness in mentoring budding engineers made for an incredibly meaningful summer experience for everyone involved. Thanks to you, hundreds of HSSRP alumni have found their calling.

To Louis Tse, Lauren Dy, and the rest of the Bruin Shelter family, for reminding me about what's possible when you have a dream. Working with you on the shelter has been one of my most fulfilling experiences and the passion for serving those in need that you showed me is something that I hope to carry and emulate for the rest of my life.

To Pam Fusek, Zach Ballard, Darren Reis, Kishan Patel, Alex Bierach, and the rest of the LA crew who made my time at 1410 Bentley Ave., Apt. 204, so special. I will forever remember our conversations, dinner parties, and hikes as some of the best years anyone could ask for.

In addition, this work was generously supported by the UCLA Mechanical and Aerospace Engineering Departmental Fellowship, the Department of Energy via Lawrence Livermore National Laboratory (DE-AC52-07NA27344, LDRD 14-SI-004), the Air Force Office of Scientific Research (Grant No. FA9550-15-1-0321), and the Department of Energy via the Presidential Early Career Award for Scientists and Engineers (Grant No. B620630), and SEAS Café.

Vita

2018	UCLA Boeing Corporation Graduate Scholarship
2017	UCLA Edward A. Bouchet Graduate Honor Society
2017	UCLA Charles E. Young Humanitarian Award
2016	Best Poster Award, UCLA MAE Industry Advisory Board Poster Competition
2016	Co-founder, Students 4 Students
2016	Facilitator, UCLA High School Summer Research Program
2015	Co-founder, Bruin Shelter
2015	Facilitator, UCLA High School Summer Research Program
2015	Vice President, UCLA Engineering Graduate Students Association
2015	Best Fast-Forward Presentation, ASME DETC Compliant Mechanisms Symposium
2015	M.S., Mechanical Engineering, UCLA
2013	B.S., summa cum laude, Mechanical Engineering, University of California, Santa Barbara
2013	Tirrell Award for Distinction in Undergraduate Research
2012	Engineering Intern, Owl Biomedical, Santa Barbara, CA
2012	UCSB Boeing Corporation Scholarship
2011	UCSB Boeing Corporation Scholarship
2011	Undergraduate Researcher, Mechanics of Microscale Systems Laboratory, University of California, Santa Barbara
2010	Engineering Intern, Acea Biosciences, San Diego, CA
2009	University of California Regents Scholarship

Journal Publications

L. Shaw, S. Chizari, M. Shusteff, H. Naghsh-Nilchi, D. Di Carlo, J. Hopkins, Scanning Two-Photon Continuous Flow Lithography for Synthesis of High-Resolution 3D Microparticles, Optics Express, 2018

L. Shaw, S. Chizari, J. Hopkins, Improving the Throughput of Automated Holographic Optical Tweezers, Optics Express, 2018 (submitted)

L. Shaw, S. Chizari, M. Dotson, Y. Song, J. Hopkins, Compliant Rolling-contact Architectured Materials, Advanced Materials, 2018 (submitted)

M. Porter, B. Giera, R. Panas, **L. Shaw**, M. Shusteff, J. Hopkins, Experimental Characterization and Modeling of Optical Tweezer Particle Handling Dynamics, Applied Optics, 2018 (submitted)

Y. Song, S. Chizari, **L. Shaw**, R. Panas, J. Mancini, J. Hopkins, A. Pascall, Mechanical Logic Based on Additive Manufacturable Micro-mechanical Logic Gates, Adv. Mat., 2018 (submitted)

L. Shaw, J. Simonelli, A. Hatamizadeh, J. Hopkins, A Mold-based Approach for Fabricating Embedded-actuator Soft Systems, Journal of Mechanical Engineering and Sciences, 2018 (submitted)

A. Delissen, G. Radaelli, **L. Shaw**, J. Hopkins, J. Herder, Design of an Isotropic Metamaterial with Constant Stiffness and Zero Poisson's Ratio over Large Deformations, Journal of Mechanical Design, 2018 (submitted)

L. Shaw, R. Panas, C. Spadaccini, J. Hopkins, Scanning Holographic Optical Tweezers, Optics Letters, 2017

L. Shaw, S. Chizari, R. Panas, M. Shusteff, C. Spadaccini, J. Hopkins, Holographic Optical Assembly and Photopolymerized Joining of Planar Microspheres, Optics Letters 41, 2016

L. Shaw, J. Hopkins, An Actively Controlled Shape-Morphing Compliant Microarchitectured Material, Journal of Mechanisms and Robotics, 2016

J. Hopkins, **L. Shaw**, T. Weisgraber, G. Farquar, C. Harvey, C. Spadaccini, Design of Non-periodic Microarchitectured Materials that Achieve Graded Thermal Expansions, Journal of Mechanisms and Robotics, 2015

L. Li, E. Holthoff, **L. Shaw**, C. Burgner, K. Turner, Noise Squeezing Controlled Parametric Bifurcation Tracking of MIP-Coated Microbeam MEMS Sensor for TNT Explosive Gas Sensing, Journal of MEMS, 2014

Chapter 1

Introduction

1.1 Motivation

The purpose of this research is to improve the speed and parallel-handling capabilities of holographic optical tweezers (HOT) systems to enable a new 3D additive fabrication approach that can assemble structures with microscale features, complex geometries, and multiple constituent materials. The HOT approach uses light as the sole handling agent to precisely trap and position nano- or micro-scale particles with no mechanical contact forces. Current AM approaches are limited by their minimum feature size, overall throughput, or the geometries that can be fabricated; however, the HOT approach offers the ability to handle micron or submicron particles at high rates and assemble geometrically-complex microstructures, which ultimately stands to enable entirely new classes of engineered materials.

The most important application of this research is the fabrication of mechanical metamaterials, which are materials that primarily derive their bulk mechanical properties from their structure instead of their chemical composition. By carefully tailoring the microstructure of these engineered materials[1,2], designers can achieve a wide variety of extraordinary material properties that are not found in natural materials[3–7]. Examples of mechanical materials include lattices with zero or negative coefficients of thermal expansion[8,9], passive[10] or active[11,12] shape-reconfigurable materials, or materials designed to achieve a prescribed degree of freedom through the deformation of compliant elements[13]. HOT systems are particularly well-suited to fabricating an additional type of metamaterial known as a microgranular crystal, which is a closely-packed lattice of microparticles. Microgranular crystals achieve unique dynamical properties from the nonlinear stiffnesses of their closely-packed particles[14,15] and hold the potential to mitigate shock waves caused by impacts[16], to route or focus acoustic vibrations[17], or to passively manipulate photons in unique ways[18].

1.2 Background

Light carries both energy and momentum, and thus can exert significant forces on small objects as described by Newton's third law of motion. Experimental demonstration of radiation pressure on objects was first provided by Pyotr Lebedev in 1900[19], but light intensities were not high enough to demonstrate confinement of objects until later in the century. Optical trapping via laser-induced radiation pressure was first demonstrated by Arthur Ashkin in 1970[20] and was a precursor to the demonstration of an optical tweezers (OT) system as a unique scientific instrument for manipulating atomic-[21], nano-[22], and micro-scale objects[23]. Arthur Ashkin focused his subsequent research efforts on investigating laser trapping of biological cells[24] and paved the way for OT systems' wide application in biological studies, where they can be used to reposition, assemble, sort, or stress individual living cells[25–27], bacteria[28], viruses[29], or strands of DNA[30]. Meanwhile, Steven Chu, an early colleague of Arthur Ashkin, demonstrated the first optical trapping of atoms[31] that lead to his 1997 Nobel Prize in physics.

Within the past few decades, there have been several different approaches to parallelize OT systems for handling multiple particles simultaneously. Dufresne and Grier first demonstrated how diffractive optical elements (DOEs) could be used to create static arrays of simultaneous optical traps[32]. Soon after, Reicherter and colleagues demonstrated the first modern HOT system, which used a phase-only computer-controlled spatial light modulator (SLM) to dynamically update the wavefront of a laser beam for real-time beam shaping[33]. The holographic beam shaping capabilities of a phase-only SLM allows for the creation of arrays of hundreds of Gaussian traps[34], as well as more complex wavefronts like Bessel[35] or vortex[36] beams. The HOT approach remains the most popular technique for trapping multiple particles in parallel[34,37] and has found adoption in applications including biology[38], materials science[39], and more recently, additive fabrication[40].

Other approaches to parallelizing the handling capabilities of optical tweezers systems involve time-multiplexing of optical traps using active scanning components like mirror galvanometers[41] or acousto-optic modulators[42]. This approach is known as scanning optical tweezers (SOT), in which the active scanning element cycles between optically-trapped particles at rates much faster than the particles can diffuse due to Brownian motion[43]. A new approach that combines both scanning and holographic approaches, or scanning holographic optical tweezers[44] (SHOT), will be presented in Chapter 3 of this thesis.

One promising application for HOT systems, and the focus of this thesis, is additive microscale manufacturing. Traditional additive manufacturing approaches are often limited in available materials, the number of different materials that can be incorporated in a single part, the minimum feature size, maximum fabrication volume, speed, and fabrication complexity (e.g., the creation of overhanging features with or without sacrificial support material). Projection microstereolithography (PμSL)[45], large-area projection microstereolithography (LAPμSL)[46], and volumetric holographic lithography[47] are prominent methods for fabricating true-3D microstructures but are limited in the number of constituent materials that can be printed and by a feature-size-to-total-volume ratio that defines the printing speed. Two-photon lithography (TPL)[48–51] offers similar prospects, and this thesis will present a novel hybrid HOT/TPL system capable of simultaneous fabrication and manipulation of microscale mechanisms and structures.

However, the HOT approach provides a promising path towards complex microassembly due to several unique capabilities not possessed by traditional additive manufacturing technologies. HOT-based approaches have been demonstrated with both nano-[22] and micro-scale[23] particles of multiple materials[52] and shapes[53], and in 1D[54], 2D[55], and 3D[56] assemblies. The HOT approach is particularly amenable to a variety of methods of particle joining, including one-photon[54,55] and two-photon[56] polymerization, streptavidin-biotin bonding[57], and DNA linkages[58]. Furthermore, HOT approaches offer the added benefit of being able to work with a variety of existing microscale components, including living cells[59], nanowires[53], and TPL-fabricated polymer components[60,61] to produce unique structures that require assembly[62]. The HOT approach has already found many applications ranging from microassembly of mechanical components[62,63], to organoids[59], to MEMS devices[64].

Thus, the HOT approach may serve as a disruptive technology for microscale assembly of entirely new classes of mechanical metamaterials. One prominent example is the microgranular lattice[15,65] (Figure 1), which drives its unique nonlinear vibrational characteristics from the Hertzian contact between its closely-packed constituent microspheres. Microgranular lattices hold the potential to be used for acoustic lenses[17] and impact-absorbing materials[66].

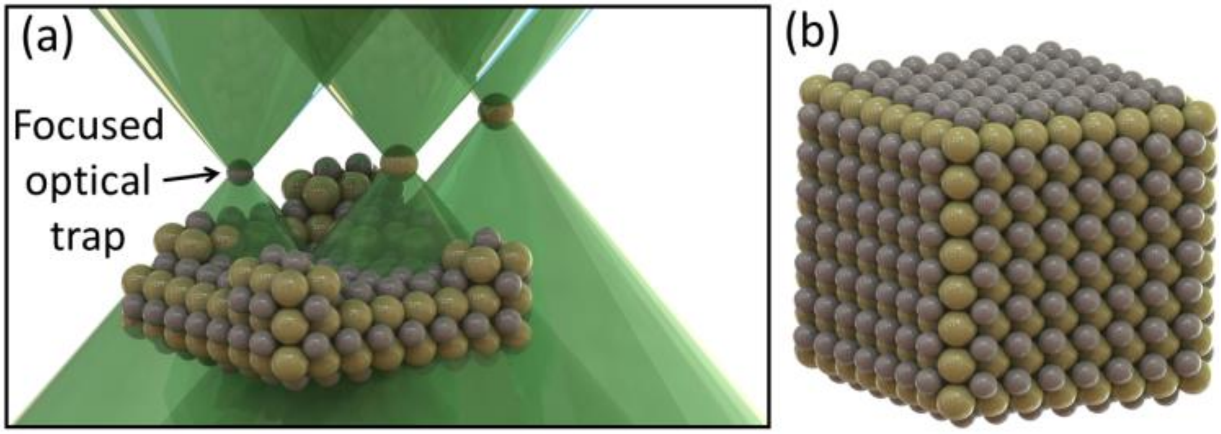

Figure 1: Construction of a microgranular crystal with the HOT approach (a) and completed microgranular lattice consisting of two particle diameters and material types (b)

1.3 Dissertation Overview

The purpose of this research is to demonstrate advances in the HOT approach for the purposes of additive fabrication of microstructures and micromechanisms. HOT-based fabrication methods are currently limited by their speed and scalability, so the results presented in this work are organized into four main categories for increasing the speed and number of particles that can be handled with the HOT approach: *(1)* increasing the number of particles that can be simultaneously trapped and handled with SHOT, *(2)* using path planning to increase the efficiency of assembly processes, *(3)* robustly controlling particle delivery by modeling the dynamics of optically-trapped particles, and *(4)* developing strategies for efficient joining of microparticles.

Chapter 2 provides an overview of OT physics, HOT operating principles, and HOT system layout considerations. Most notably, this chapter presents unique work in modeling the tradeoff between working area (i.e., the area over which the system can handle particles) and numerical aperture (which is related to trap stiffness) in HOT systems. This chapter is not meant to serve as a comprehensive overview of phase retrieval algorithms, potential system layouts, or design trade-offs, but does provide a practical overview of the most important information for those looking to recreate the HOT results presented in this work.

Chapter 3 addresses a new approach that increases the number of particles that can be trapped simultaneously handled with optical tweezers. Using a fast scanning mirror galvanometer to time-multiplex holographic trapping patterns enables the first SHOT system, in which tightly-focused optical traps can be created over a large working area.

Chapter 4 discusses efficient heuristic algorithms for path planning of HOT-based assembly processes. Additionally, this chapter presents an image-feedback-based controller that ensures that desired objects reach their destinations while rejecting undesired (e.g., misshapen) objects. The presented controller can run at 6Hz in closed-loop mode or 10Hz by using a combination of open- and closed-loop steps. The controller is used to assemble up to 100 particles simultaneously – a 2-4x improvement over existing literature covering dynamic HOT systems.

Chapter 5 provides a brief overview of OT and HOT dynamics modeling efforts. Investigating the dynamics of particles in continuously-slewed and discretely-stepped optical traps provides valuable insight into the optical operating conditions that increase speed and reliability during HOT assembly processes. Furthermore, the chapter introduces a novel method for mapping the full optical force profile for any HOT system and discusses practical limitations on Mie-regime optical force simulations.

Chapter 6 introduces a new one-photon photopolymerization chemistry that allows for particles to be adhered to a substrate or joined to one another to produce permanent structures.

This chapter also introduces an online process control for monitoring the photopolymerization reaction to determine when the reaction is complete. This work represents the first time that such approaches were used to create permanent planar arrangements of microparticles.

Chapter 7 introduces the concept of two-photon lithography (TPL), which offers a promising path towards improving the localization and scalability of the photopolymerization approach presented in Chapter 6. First, a novel hybrid TPL-HOT system is presented. Next, the TPL system is used for direct microscale 3D printing of microstructures and colloidal objects. Finally, the chapter concludes by offering an outlook on the flexibility of HOT-TPL fabrication.

Chapter 8 offers concluding remarks, including suggested future work and an outlook on HOT systems as a viable micromanufacturing technique.

The appendices include relevant supplementary material, including *(A)* a glossary of relevant optical equations, *(B)* an overview of the MATLAB-based control software, *(C)* a MATLAB script used to model the working area and numerical aperture trade-off as descripted in Chapter 2, and *(D)* a MATLAB script used to model the reflective and apodizing effects on a focusing trapping beam at a medium boundary as described in Chapter 5.

Chapter 2

An Overview of Holographic Optical Tweezers

2.1 Operating Principles

2.1.1 The Optical Trap

Optical tweezers (OT) made their debut in Ashkin's seminal 1970 paper[20] and have since become a powerful tool for manipulating micro- and nano-scale particles. A simplistic depiction of an optically-trapped particle is provided in Figure 2, in which a microsphere is displaced slightly from a focused laser's beam waist and experiences a restoring force (F) that is a function of its displacement from the beam's focal point (x). The spring constant in the equation $F = k_{trap} \cdot x$ is roughly constant for small displacements (i.e., for x less than 0.5-1.0 particle radii, depending on system parameters like numerical aperture, beam quality, particle size and shape, refractive indices, and laser wavelength). As the particle is displaced further than 0.5-1.0 particle radii, the spring constant becomes nonlinearly dependent on the displacement and the magnitude of the optical force reduces. The linear, small-displacement regime is most relevant to continuous-velocity optical traps (such as those found in single-trap OT systems), while the nonlinear, large-displacement regime is most relevant in the discrete-stepping operation of HOT systems. A more in-depth discussion of these dynamic regimes can be found in Chapter 5 of this thesis.

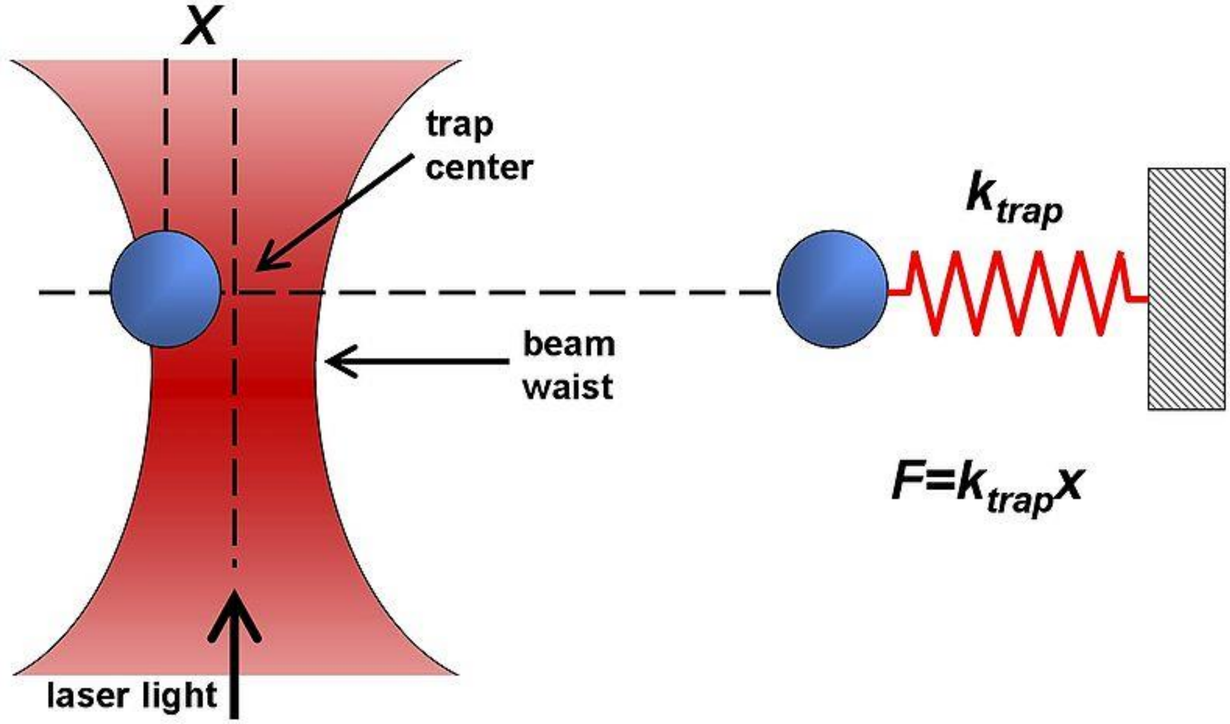

Figure 2: Diagram of an optically-trapped microsphere

Analysis of the optical forces on a trapped microparticle falls into one of three regimes depending on the particle's size with respect to the wavelength of the trapping laser[67,68]. The first regime is known as the Rayleigh regime, where particles are very small with respect to the trapping wavelength (i.e., $d \ll \lambda$, typically by 1-2 orders of magnitude)[52]. Rayleigh-regime modelling approaches typically involve treatment of particles as individual dipoles within the electromagnetic field of the laser beam. A gradient force arises from the dipole's attraction towards the point of maximum intensity (i.e., the laser's focal spot), creating a stable optical trap. The gradient force increases with laser intensity, particle volume, and the gradient of the electric field (i.e., a function of numerical aperture, M^2-value, and laser wavelength). As the dipole interacts with the oscillating electromagnetic field, it oscillates and reradiates energy uniformly in every direction. Metallic particles are also susceptible to other resonant effects such as those due to surface plasmons[69–71].

In the second regime known as the Mie regime, particle diameters are near the same order as the trapping wavelength (i.e., $d \sim \lambda$). The Mie regime, which most accurately describes the optical forces on the microparticles found in this thesis, features two competing forces: *(1)* a gradient force that attracts particles to the center of the beam waist, and *(2)* a scattering force that pushes particles downstream (akin to a fire hose of photons). Even in optical traps with very high gradient force fields, the stable equilibrium point for a trapped spherical particle is slightly downstream from the center of the beam waist because of the scattering force. The Mie regime requires a rigorous analytical approach such as that provided by generalized Lorenz-Mie theory (GLMT)[72]. A popular numerical approach for applying GLMT to spherical particles is the T-matrix formalism, which uses matrix operators to compute radial and axial trap stiffnesses[73]. Arbitrarily-shaped (i.e., non-spherical) particles in the Mie regime require more computationally intensive simulations[74].

In the third and final regime, known as the ray tracing or ray optics regime, particles are large with respect to the trapping wavelength (i.e., $d \gg \lambda$, typically by an order of magnitude)[75] and traditional ray tracing approaches are valid. Most optical tweezers research has been focused on trapping particles in the Rayleigh or Mie regimes, so a discussion of the ray optics regime is not included in this work but can be found in existing literature[76].

2.1.2 Parallelized Optical Trapping: The Holographic Optical Tweezers Approach

In the past few decades, two primary approaches (i.e., the scanning-optical-tweezers (SOT) and the holographic-optical-tweezers (HOT) approaches) have been pursued as a means of increasing the number of particles that can be handled simultaneously using optical tweezers. The SOT approach typically relies on a 2D mirror galvanometer or an acousto-optic modulator (AOM) to periodically time-share a single focused laser beam among multiple trapped particles more rapidly than the particles can diffuse due to Brownian motion[77,78]. Although this approach can achieve a large working area (WA), it is limited to Gaussian traps within the focal plane. In contrast, the HOT approach uses a computer-controlled spatial light modulator (SLM) to divide a single input beam into multiple continuously powered optical traps[34,40]. Although this approach can construct a diversity of structured traps beyond Gaussian[36,41] and these traps can be moved in and out of the focal plane, the HOT approach is limited by an inversely-proportional relationship between its largest WA and its smallest achievable trap size (this relationship is explored in Section 2.2.2). In this work, we primarily focus our discussion on the HOT approach, but Chapter 3 will introduce a new technique called scanning holographic optical tweezers (SHOT), in which a 2D mirror galvanometer is synchronized in serial with an SLM.

The insertion of a tailored phase or amplitude pattern at a plane conjugate to the trapping plane allows for a single input laser beam to be shaped into a custom holographic pattern. The most common device for introducing diffraction patterns is a computer-controlled phase-only spatial light modulator (SLM). SLMs have found wide adoption in applications including optical tweezers[34], pulse shaping[79], and beam splitting and steering[80]. The SLMs in this work consist of an array of nematic liquid crystals over discretely-addressable pixels on a silicon backplane (Figure

3). The electric field that forms between the pixel pixels on the silicon backplane and the conductive coverglass can reorient the liquid crystals in the intermediate layer, changing the effective optical path length of the light that enters and reflects within the device. By applying the proper voltages (typically provided by the SLM manufacturer in a factory-calibrated look-up table), the optical path length can be modulated from 0 to 2π at each pixel, resulting in a phase pattern imprinted on an illuminating laser beam.

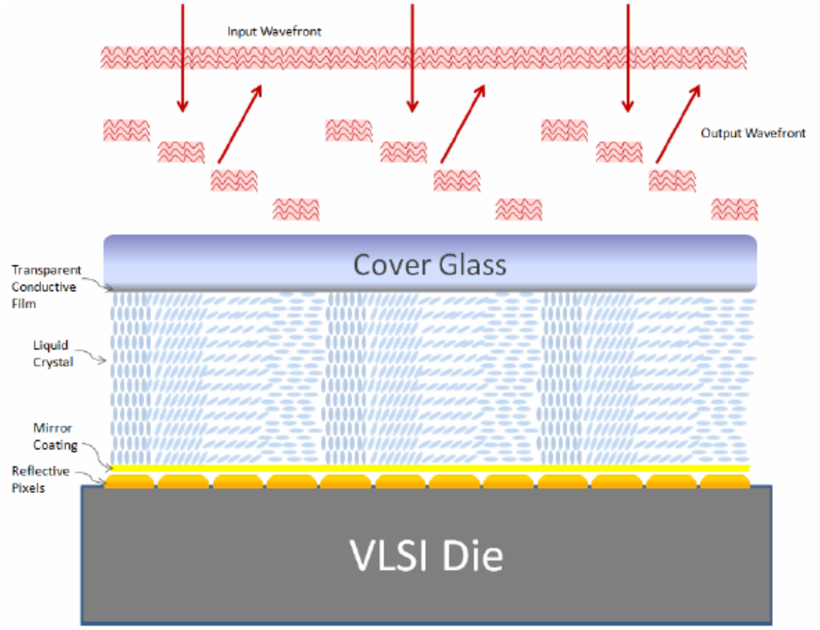

Figure 3: Working principles of an SLM (image courtesy of Meadowlark Optics)

A rigorous discussion of the Fourier-transforming property of a lens is well-described in Goodman's seminal textbook on Fourier optics[81] but two brief HOT-related examples are provided in Figure 4 and Figure 5. If a coherent continuous wave (CW) laser illuminates a ramp phase grating with nearly uniform intensity, the result is a single off-axis trap at the focal plane of the microscope objective (MO, Figure 4).

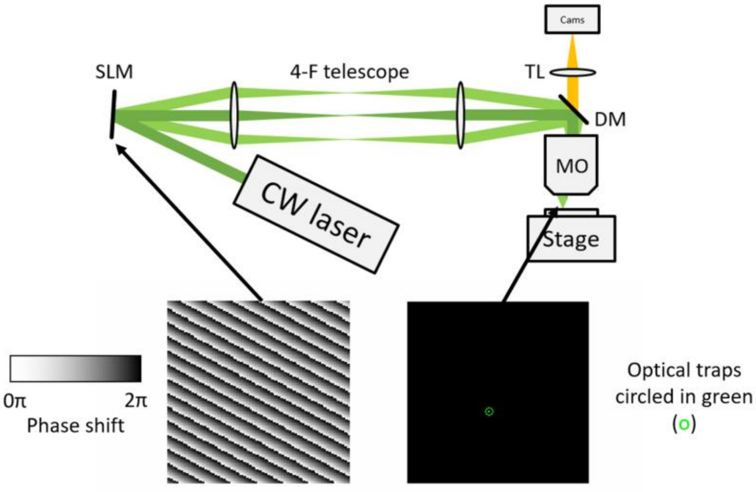

Figure 4: HOT system and phase pattern for a single off-axis optical trap

In a more complicated example, if the same laser is used to illuminate the non-intuitive phase-modulating pattern shown in Figure 5, a specific array of traps forms at the focal plane of the MO. Phase patterns are often calculated with the Gerchberg-Saxton phase retrieval algorithm[82], which is described in detail in Section 2.1.3.

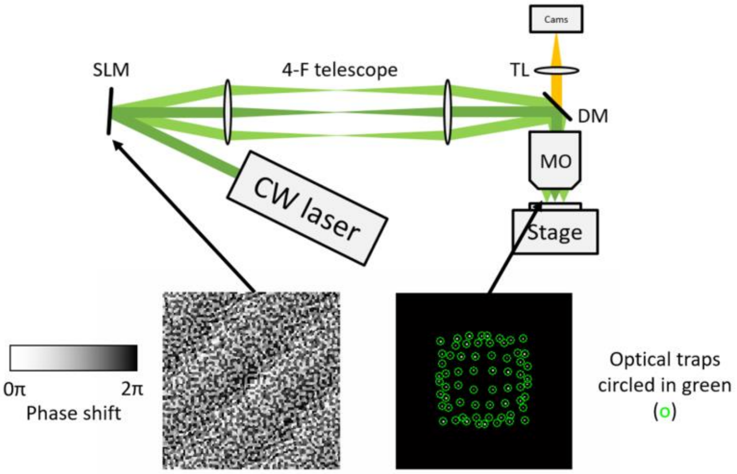

Figure 5: HOT system and phase pattern for multiple off-axis optical traps

2.1.3 The Gerchberg-Saxton Phase Retrieval Algorithm

In the 1970s, R. W. Gerchberg and W. O. Saxton introduced a highly-effective numerical approach for computing the phase of a wave provided only intensity measurements in the imaging and Fourier planes[82] (i.e., the SLM and trapping planes). The GS algorithm begins with an initial phase 'guess' and proceeds by iteratively propagating back and forth between the imaging and Fourier planes. At each plane, the respective amplitude distribution is imposed while the phase converges on a final state. In the experiments described in this thesis, the initial guess was a matrix of zeros and the number of iterations typically ranged from one to three depending on the complexity of the desired optical trapping pattern. In practical terms, the amplitude distribution at the SLM is provided by the laser source's Gaussian profile, and the desired amplitude distribution at the trapping plane is provided by features (e.g. nonzero values) at the locations of each trap.

The steps of the standard Gerchberg-Saxton phase retrieval algorithm (Figure 6) proceed as follows:

1. An initial phase distribution, $\Phi_{SLM}(x, y)$, is created, either from an arbitrary matrix or via estimation (e.g., from a previous state). The field at the SLM is formed by combining the phase with the SLM's prescribed amplitude distribution as: $U'_{SLM}(x, y) = A_{SLM}(x, y)e^{j\Phi_{\mathrm{SLM}}(x,y)}$
2. The field at the trapping plane is obtained by computing a zero-frequency centered Fourier transform: $U_{trap}(u, v) = F\left(U'_{SLM}(x, y)\right) = A(u, v)e^{j\Phi_{trap}(u,v)}$
3. The desired amplitude at the trapping plane is imposed on the field: $U'_{trap}(u, v) = A_{trap}(u, v)e^{j\Phi_{\mathrm{trap}}(u,v)}$

4. Back-propagation to the SLM plane proceeds via an inverse Fourier transform: $U_{SLM}(x,y) = F^{-1}\left(U'_{trap}(u,v)\right) = A(x,y)e^{j\Phi_{SLM}(x,y)}$
5. The SLM's amplitude distribution is imposed on the field as: $U'_{SLM}(x,y) = A_{SLM}(x,y)e^{j\Phi_{SLM}(x,y)}$
6. Steps 2-5 are iterated until $\Phi_{SLM}(x,y)$ has converged, typically after 1-10 iterations for simple arrays of individual Gaussian optical traps. The final phase pattern is then uploaded to the SLM hardware.

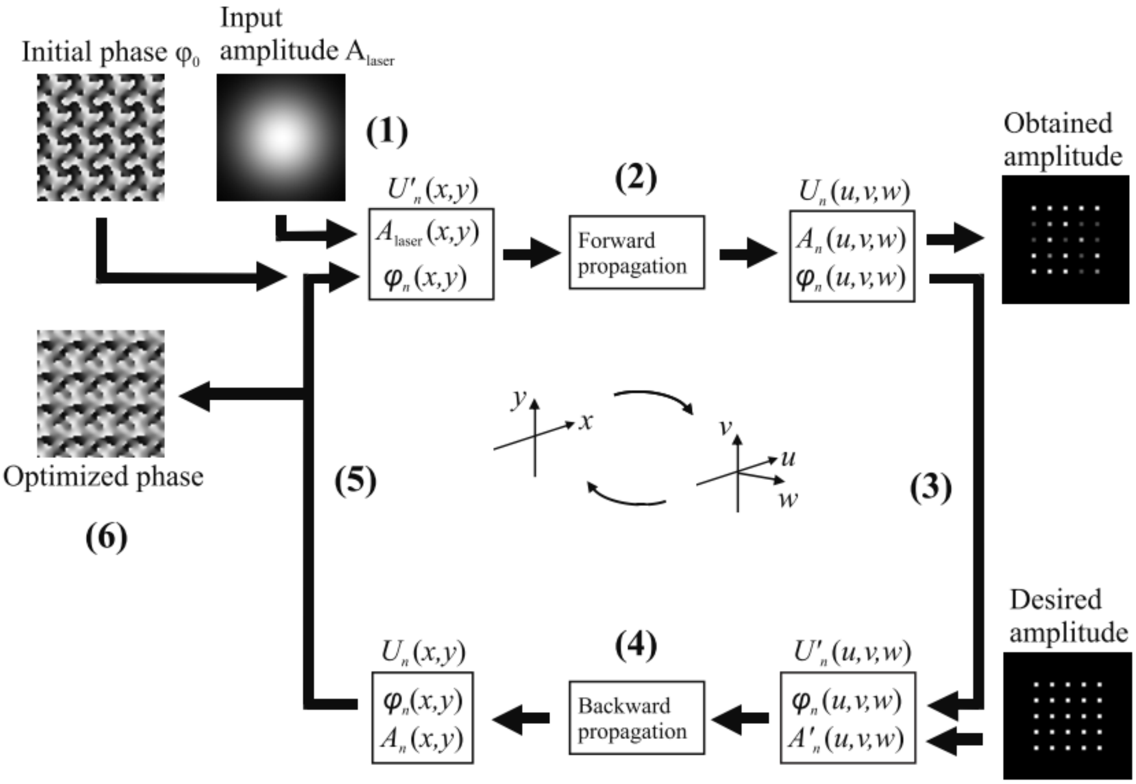

Figure 6: The standard Gerchberg-Saxon algorithm (image courtesy M. Persson[83])

The adaptive-additive Gerchberg-Saxton (AAGS) algorithm[84] (Figure 7) is a popular variation that includes a feedback term when imposing the desired trapping amplitude:

$$U'_{trap}(u,v) = \left[\alpha A_{trap}(u,v) + (1-\alpha)A(u,v)\right]e^{j\Phi_{trap}(u,v)} \tag{1}$$

When $1 < \alpha \leq 2$, the uniformity of the hologram increases at the expense of overall diffraction efficiency. When $0 < \alpha \leq 1$, the diffraction efficiency is increased at the expense of uniformity[85]. If $\alpha = 1$, the AAGS algorithm reverts to the standard GS algorithm.

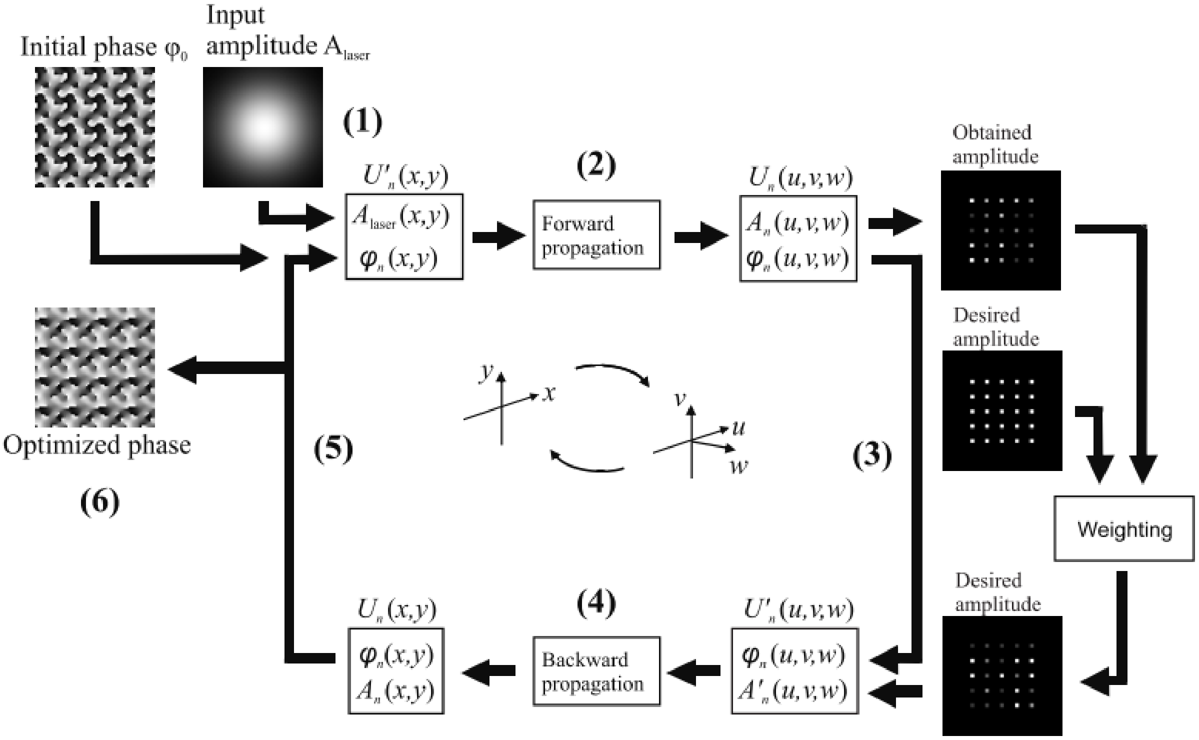

Figure 7: The adaptive-additive Gerchberg-Saxon algorithm (image courtesy M. Persson[83])

The GS or AAGS algorithms can also be used to compute holograms with optical traps located in 3D space[84]. Rather than propagating the field from the SLM plane to a single trapping plane via a standard Fourier transform, the SLM field is propagated via a diffraction kernel to each of *n* planes on which traps are to be prescribed. The full 3D GS algorithm (Figure 8) proceeds similarly to the standard GS algorithm, except for differences in steps 2-4:

1. An initial phase distribution, $\Phi_{SLM}(x,y)$, is created, either at random or via estimation (e.g. from a previous state). The field at the SLM is formed by combining the phase with the SLM's prescribed amplitude distribution as: $U'_{SLM}(x,y) = A_{SLM}(x,y)e^{j\Phi_{\mathrm{SLM}}(x,y)}$
2. The field at each of *n* trapping planes is obtained by computing a zero-frequency centered Fourier transform: $U_{trap,n}(u,v) = F\left(h_n(x,y) * U'_{SLM}(x,y)\right) = A(u,v)e^{j\Phi_{trap}(u,v)}$, where $h_n(x,y) = \exp\left(-\pi\frac{x^2+y^2}{\lambda^2}\right)$ is the diffraction kernel[86]
3. The phase at each of n trapping planes is: $\Phi_{trap,n}(u,v) = angle\left(U_{trap,n}(u,v)\right)$. The desired amplitude at each of n trapping planes is imposed on each field: $U'_{trap,n}(u,v) = A'_{trap,n}(u,v)e^{j\Phi_{trap,n}(u,v)}$
4. The fields at each of *n* trapping planes are back-propagated to the SLM plane and summed: $U_{SLM}(x,y) = \sum_n U_{SLM,n}(x,y) = \sum_n F^{-1}\left(h_n^* * U'_{trap,n}(u,v)\right)$, where h_n^* is the complex conjugate of the diffraction kernel in step 2
5. The SLM's amplitude distribution is imposed on the field as: $U'_{SLM}(x,y) = A_{SLM}(x,y)e^{j\Phi_{SLM}(x,y)}$
6. Steps 2-5 are iterated until $\Phi_{SLM}(x,y)$ has converged. This phase pattern is uploaded to the SLM.

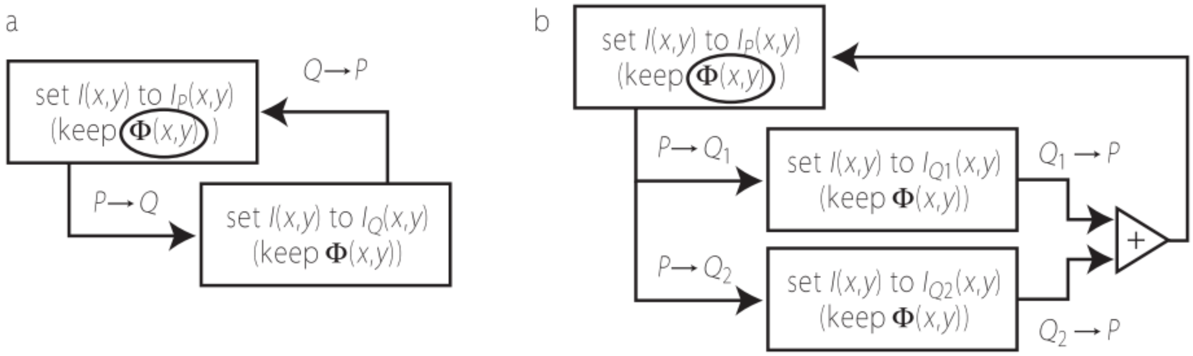

Figure 8: Comparison between the standard GS (a) and multiplane GS (b) algorithm (image courtesy of G. Sinclair, et. al.[87])

Following the GS algorithm or one of its variants, the retrieved phase distribution $\Phi_{SLM}(x, y)$ is converted into the correct data format (e.g., unsigned 8-bit integers) and uploaded to the SLM via MATLAB software.

Additional algorithms, including the direct search[88], random mask encoding[89], superposition[90], and weighted Gerchberg-Saxton[91], are not discussed or utilized in this work, but detailed comparisons can be found in existing literature[85].

2.2 Description of System Components

This section outlines the general experimental system used in this work (Figure 9), which can be broken into:

- The laser, power modulation, and beam shaping sub-systems (Section 2.2.1)
- The 4-F telescope relay (Section 2.2.2)

- The imaging system (Section 2.2.3)
- The sample chamber and motion control systems (Section 2.2.4)
- The microfluidic dispensing system (Section 2.2.5)

Subsequent chapters use a variant on this general system but include relevant details on the differences. The 690-1040nm ultrafast laser used in the two-photon lithography system described in Chapter 7 is not included, but the beam's injection location is depicted by the arrow on the righthand side of the figure.

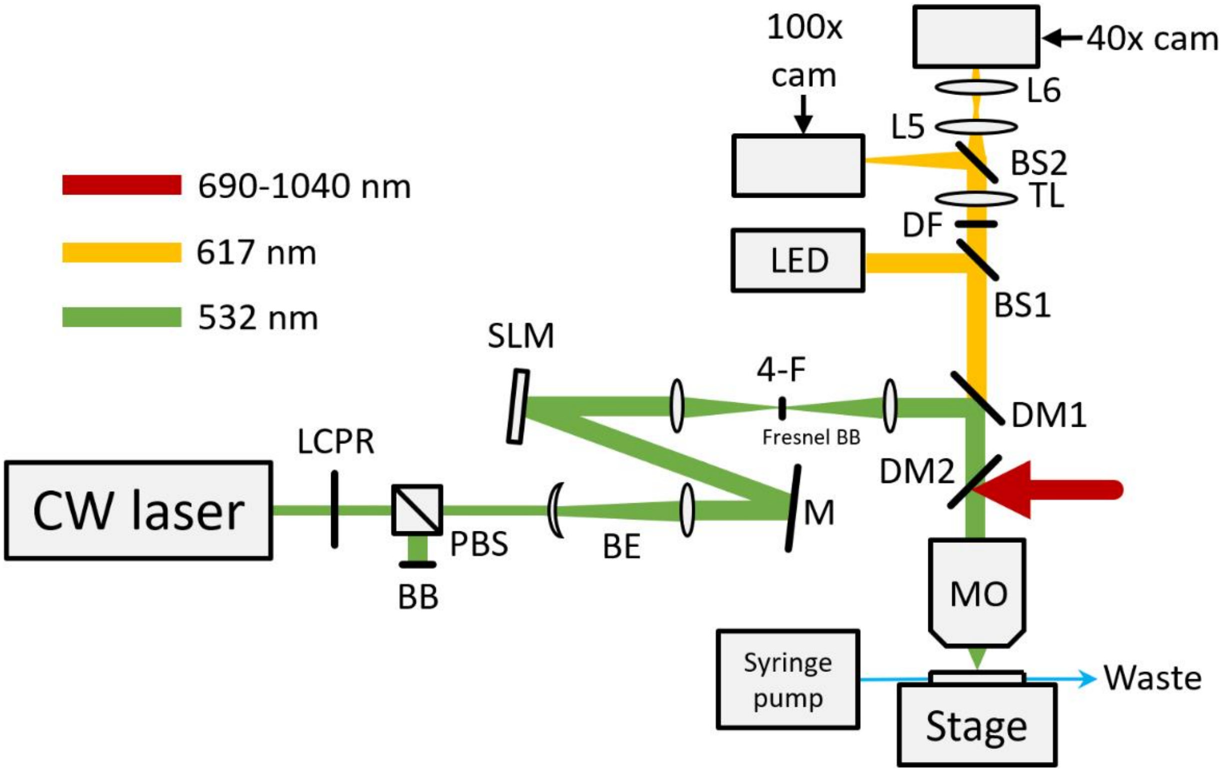

Figure 9: General HOT system diagram

2.2.1 The Laser, Power Modulation, and Beam Shaping

The standard HOT system used in this thesis (Figure 9) relies on a continuous-wave (CW) laser (Laser Quantum Opus, 3W at 532nm) for trapping. A liquid crystal polarization rotator (LCPR; Meadowlark Optics LPR-100-0532) used in conjunction with a polarizing beamsplitter (PBS) and beam block (BB) allow for rapid and computer-controlled attenuation of the total optical power fed into the system. This configuration provides a constant amount of power per optical trap as the number of optical traps changes during automation. By keeping individual traps at a constant and conservative power level (e.g., 2.5-5.0mW each), we prevent multiple particles from settling into a single trap, resulting in more reliable automation.

The beam expander (BE, Figure 9) consists of a negative and positive focal length doublet lens in a Galilean configuration. The lenses are selected to provide a 4x magnification to fully illuminate the face of the SLM. The lenses are f = -50mm and 200mm doublets with anti-reflective coatings (ARC) in the visible range (Thorlabs ACN254-050-A and AC254-200-A).

The first mirror (M, Figure 9) is a second-harmonic Nd:YAG laser-line mirror (Thorlabs NB1-K12) used to redirect the illumination beam onto the SLM’s face at a low angle of incidence (9°) as recommended by the SLM’s manufacturer.

2.2.2 The 4-F Telescope and Space-Bandwidth Product Calculations

A phase-only SLM (either a Boulder Nonlinear Systems HSP256-0532 or Meadowlark Optics 1920x1152, which is clarified in the experimental sections throughout each chapter of this thesis) provides the programmable phase modulation necessary to produce arbitrary arrays of optical traps at the focal plane of the microscope objective. In addition to transmitting the phase-modulated light that forms the optical traps, the SLM also transmits unmodulated light that forms an undesirable zero-order spot (ZOS)[92,93] at the center of the trapping plane. The light that forms the ZOS is a result of unmodulated reflections from the SLM's coverglass and backplane between pixels. To allow for optical trapping across the full working area of the SLM, the presented system uses a Fresnel block setup[94] consisting of a 200µm-diameter gold film deposited on a glass coverslip to block the SLM's undesired zero-order spot. Holograms for optical trapping are combined with an additional lens-phase term to focus in front of the Fresnel block.

The 4-F telescope is a two-lens relay system that is used to transfer the electric field distribution (i.e., both the phase and amplitude) from the SLM plane to the input aperture of the microscope objective (Figure 10). The 4-F relay consists of two lenses with focal lengths f_1 and f_2. The first lens is placed at a distance f_1 from the SLM, the second lens is placed at a distance of $f_1 + f_2$ from the first lens, and the microscope objective is located at a distance f_2 from the second lens (i.e., in Figure 10, the SLM would be located at the left-hand sinusoidal grating and the microscope objective's input pupil would be located at the right-hand image). The first lens in the 4-F relay performs a Fourier transformation and the second lens performs an inverse Fourier transformation, thus transporting the SLM's electric field to the microscope objective, which performs the final Fourier transform to the optical trapping plane.

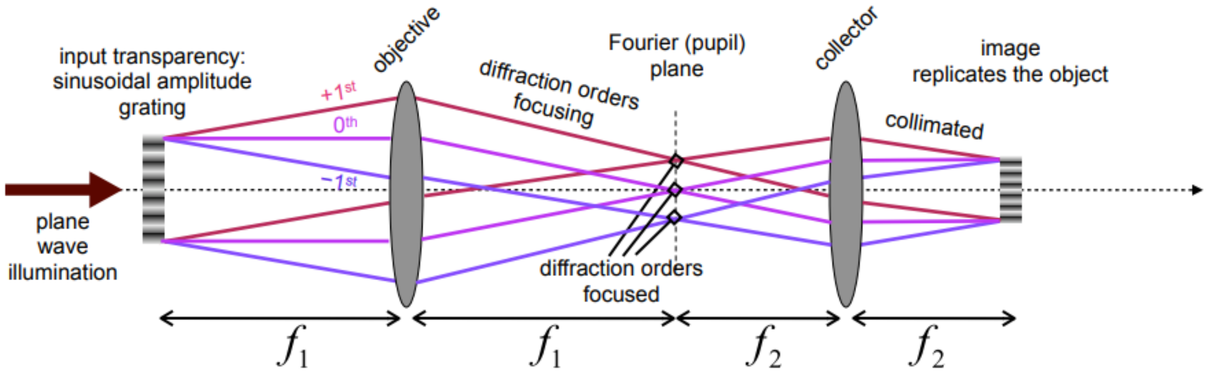

Figure 10: General representation of a 4-F telescope (image courtesy MIT[95])

The lateral magnification (i.e., the height of the object at the output divided by the height of the object at the input) is calculated from the ratio of the two 4-F relay lenses.

$$M_{lateral} = -\frac{f_2}{f_1} \tag{2}$$

In contrast, the angular magnification captures the factor that the angle subtended by the output objects changes with respect to the angle subtended by the input object. The angular magnification is inversely proportional to the lateral magnification.

$$M_{angular} = \frac{f_1}{f_2} \tag{3}$$

The focal lengths of the two lenses in the pre-SLM beam expander and the two lenses in the 4-F telescope must be carefully selected to produce a desirable balance between working area (WA) and effective numerical aperture (NA). The WA describes the maximum area over which the SLM can produce optical traps. A binary phase grating at the SLM's Nyquist frequency (i.e., a striped pattern in which adjacent pixels along one axis are π out-of-phase) produces an optical trap furthest off-axis. Thus, the maximum angle that the SLM can steer light, which bounds the system's WA, can be calculated using the grating equation for a square-wave pattern[96]:

$$\theta_m = \operatorname{asin}\left(n_{inc} \cdot \sin(\theta_{inc}) - \frac{m \cdot \lambda_0}{\Lambda \cdot n_{ref}}\right) \tag{4}$$

In this equation, θ_m represents the angle of reflection off the SLM for the m^{th}-order, θ_{inc} represents the angle of incidence of the illumination source on the SLM, n_{inc} and n_{ref} represent the indices of refraction of the incidence and reflection media respectively, Λ represents the grating period, and λ_0 represents the illumination wavelength. The maximum single-sided diffraction angle can be calculated by using $m = 1$ and $n_{inc} = n_{ref} = 1$ for free-space reflection (and using the SLM parameters provided in

Table **1**) as:

$$\theta_{ref} = \operatorname{asin}\left(\sin(\theta_{inc}) - \frac{\lambda_0}{\Lambda}\right) \tag{5}$$

Table 1: Parameters for SLM devices used in this work

SLM type	Boulder Nonlinear Systems HSP256-0532	Meadowlark Optics 1920x1152
SLM area	6.14 x 6.14mm	17.7 x 10.6mm
Pixel array size	256 x 256	1920 x 1152
Pixel size	24.0μm	9.21μm
Minimum grating period (Λ)[a]	48.0μm	18.4μm
Illumination wavelength (λ_0)[b]	532nm	532nm
Illumination angle (θ_{inc})[c]	9°	9°

[a] The grating period is twice the pixel size where each pixel is π out-of-phase from its neighbor for

[b] For the Laser Quantum Opus 3W trapping laser

[c] Set by the physical geometry of the experimental system

The SLM's maximum diffraction angle, θ_{ref}, is then magnified or demagnified by the 4-F relay system (i.e., by a factor of $M_{ang,4F}$) before reaching the microscope objective's input aperture. The WA is then calculated from the off-axis trap distance at the focal plane created by a maximum-frequency grating by using the following equation and the parameters in

Table 2:

$$r_{max} = f_{MO} \cdot \tan\left(\theta_{ref} \cdot M_{ang,4F}\right) \tag{6}$$

$$WA = 4r_{max}^2$$

Table 2: Microscope objective parameters

Olympus Plan Apo Lambda 100x	
Numerical aperture (NA_{MO})	1.45
Input aperture (d_{MO})	5.8mm
Focal length (f_{MO})	2mm

Another important system parameter is the effective NA (which differs from the microscope objective's design NA as printed on the side of the objective) describes the angle at which the individual optical traps focus, where larger focusing angles produce smaller trap diameters, larger electric-field gradients, and higher trapping forces. In the general case of a fully-filled microscope objective, the focusing angle is a function of the microscope objective's design NA and the index of refraction of the medium (e.g., $n_{water} = 1.33$):

$$NA_{MO} = n \cdot \sin\theta \tag{7}$$

However, the effective (i.e., actual) NA is a function of the fill factor of the microscope objective (α),

$$NA_{effective} = \alpha \cdot NA_{MO} \tag{8}$$

$$\alpha = \frac{d_{SLM} \cdot M_{lat,4F}}{d_{MO}}$$

$$d_{SLM} = d_{laser} \cdot M_{lat,BE}$$

where d_{laser} represents the output diameter of the laser (d_{laser} = 1.85mm for the Laser Quantum Opus 3W used in this work) and $M_{lat,BE}$ and $M_{lat,4F}$ represent the lateral magnifications of the beam expander and 4F relay, respectively. The fill factor, α, is constrained by the physical stops of the microscope objective such that $0 \leq \alpha \leq 1$.

Therefore, the following relationships hold:

$$r_{max} \cong f_{MO} \cdot \theta_{ref} \cdot M_{ang,4F} \tag{9}$$

$$NA_{effective} = NA_{MO} \cdot \frac{d_{SLM}}{d_{MO}} \cdot M_{lat,4F}$$

$$M_{lat,4F} \cdot M_{ang,4F} = -1$$

$$r_{max} \cdot NA_{effective} \cong c(d_{SLM})$$

Thus, the system's effective NA (related to peak trap force) is inversely proportional to the side length of the system's working area (i.e., the maximum area over which particles can be trapped), and their product is product is proportional to the diameter of the beam illuminating the active area on the SLM. A MATLAB script that uses these relationships to model the NA-WA relationship is provided in Appendix A.

From the relationships given in Eq. (9), the HOT 4-F relay lens selection rules can be summarized as follows:

1. The SLM should be as fully illuminated as possible to maximize the NA-WA product. However, excessive overfilling should be avoided to prevent adding power to the SLM's ZOS.
2. The focal lengths of the 4-F telescope lenses (i.e., f_1 and f_2) should be selected such that their ratio produces the desired balance between effective NA and SLM WA. The focal lengths must be selected from the discrete values offered by a chosen vendor. NA and WA values for any combination of lenses can be simulated simultaneously using a MATLAB script like the one provided in Appendix A. Lenses with excessively short focal lengths (e.g., $f < 40mm$) are highly sensitive to aberrations that arise from slight misalignments, while lenses with excessively long focal lengths (e.g., $f > 1m$) may also produce aberrations due to free-space diffraction.
3. Proper lens diameters should be selected to ensure that the lens apertures can accommodate the required lateral and angular magnifications (this work primarily used 1"-diameter lenses for lens focal lengths between 100-300mm).

2.2.3 The Imaging System

The imaging system (Figure 11 and Table 3) consists of a 100x oil immersion microscope objective (MO, Olympus Plan Apo Lambda, NA = 1.45) and two cameras (Thorlabs DCC1545M) that allow for simultaneous imaging at 40x and 100x magnification. A longpass dichroic mirror (DM1) allows the 532nm HOT light to reflect into the microscope objective while passing the 617nm illumination light. A shortpass dichroic mirror (DM2) allows the 690-1040nm near-infrared/infrared light from the TPL laser (as discussed in Chapter 7) to reflect into the microscope objective while also transmitting the 617nm illumination light. The first nonpolarizing beamsplitter (BS1, 50:50 R:T) reflects in light from the 617nm darkfield LED source. A stock tube lens (Thorlabs ITL200) begins focusing the light after the MO's infinity space and the second nonpolarizing beamsplitter (BS2, 90:10 R:T) splits light to the high-magnification (100x) camera. Imaging light transmitted through BS2 enters the custom tube lens system before the low-magnification (40x) camera. The focal lengths and locations of the four demagnification lenses (L1, L2, L3, and L4) were optimized using Zemax software to produce near-diffraction-limited performance, as shown in the spot diagrams in Figure 11.

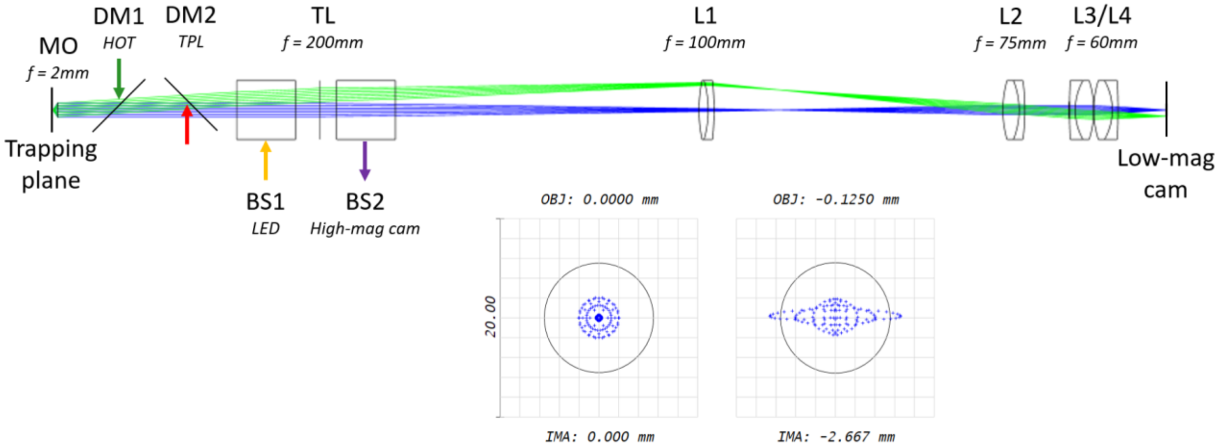

Figure 11: Schematic and spot diagrams of custom low-magnification tube lens system

Table 3: Lens location data of custom low-magnification tube lens system

Label	**Focal length (mm)**	**Type**	**Distance to next lens (mm)**
MO	2	Olympus Plan Apo Lambda 100x	113.4 (infinity space)
TL	200	Thorlabs ITL200	163.7
L1	100	Thorlabs AC254-100-A	124.8
L2	75	Thorlabs AC254-75-A	19.3
L3	60	Thorlabs AC254-60-A	0
L4	60	Thorlabs AC254-60-A	20.9 (to low-mag cam)

The optical illumination configuration (i.e., brightfield or darkfield) is dependent on the indices of refraction of the medium and the objects that are to be imaged. The imaging system used in this work features a combination of switchable darkfield and brightfield illumination sources (Thorlabs M617L3), which produce different images that are useful for different purposes (Figure 12).

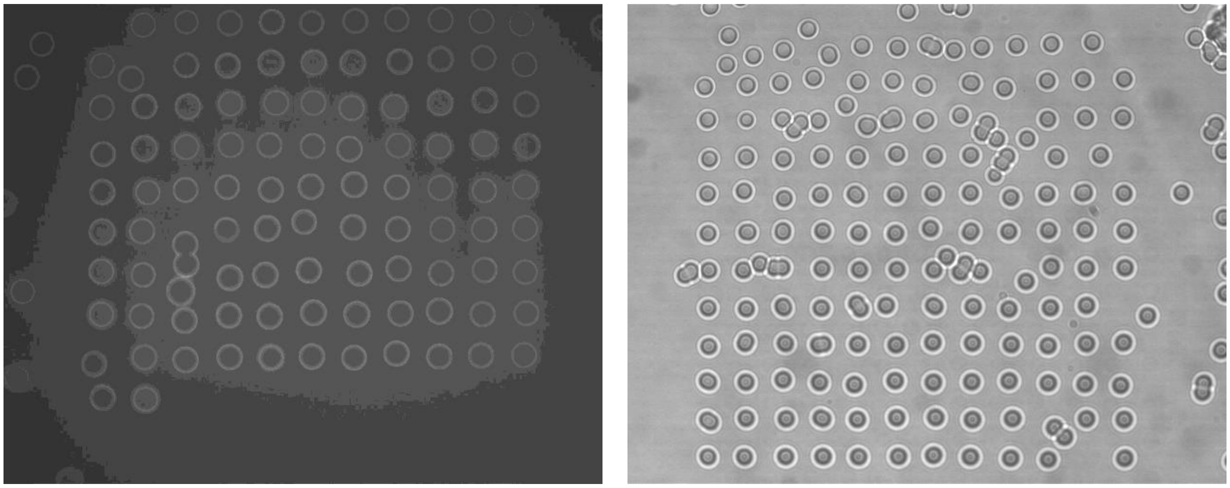

(a) (b)

Figure 12: 6.0µm polystyrene microspheres in darkfield (a) and brightfield (b) illumination

Darkfield imaging (Figure 12a and Figure 13) relies on back-scattered light from the objects to produce a signal at the camera sensor. Darkfield images of microspheres are advantageous when using an automated detection routine as the bright halos of reflected light produce sharp features that are reliably tracked. This illumination modality is best for particles with a much higher refractive index than the surrounding medium. Furthermore, darkfield imaging produces the best images when objects are one characteristic length above or below the camera's focal plane. For these reasons, darkfield images are used in the HOT chapters (i.e. chapters 2-6) of this work.

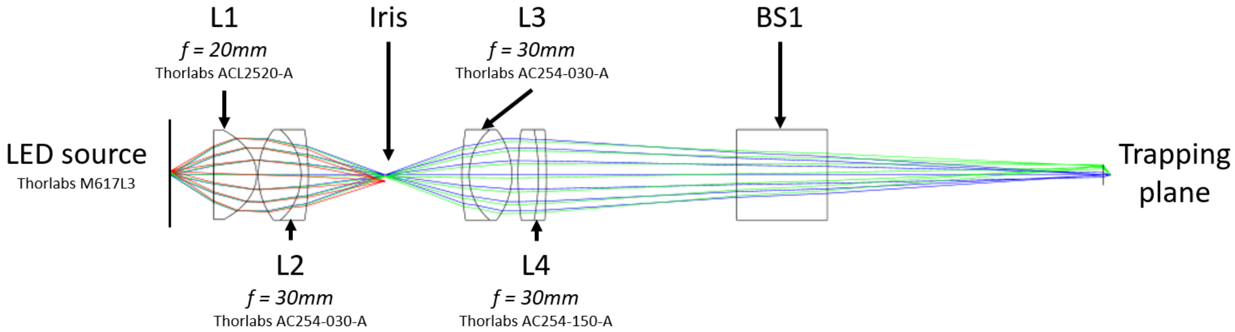

Figure 13: Physical optical layout of the darkfield illumination source

Brightfield imaging (Figure 12b and Figure 14) relies on light transmitted through the sample to produce contract at the camera sensor. The images produced using a brightfield source provide more contrast to smaller differences in refractive index and can imagine particles that are further above or below the camera's focal plane. Brightfield imaging is the preferred method for imaging low-refractive-index-difference objects fabricated with two-photon lithography, such as in chapter 7 of this work.

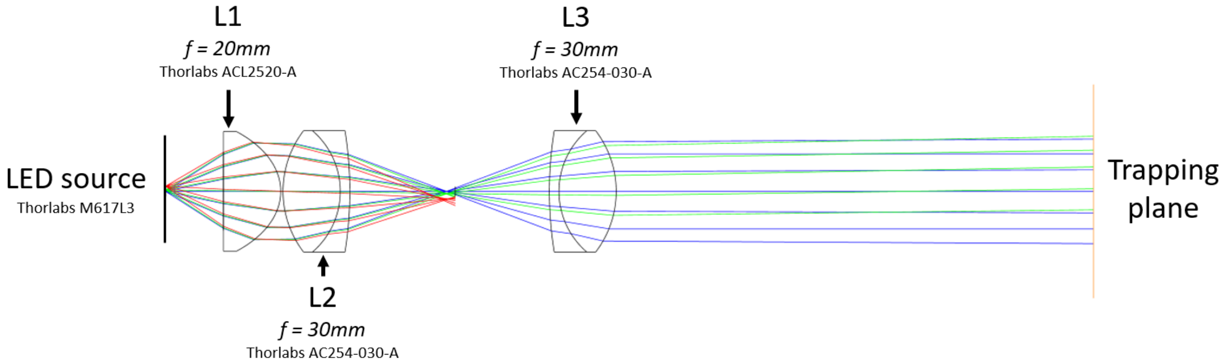

Figure 14: Physical optical layout of the brightfield illumination source

2.2.4 Sample Chamber and Motion Control

The sample chamber consists of a standard microscope slide and coverslip separated by one layer of 60μm-thick double-sided tape. The microscope slide containing the sample is positioned using a 3-axis micropositioning stage and stepper motors (Thorlabs MAX341 and BSC203).

Additional tip-tilt control for the sample positioning system was used in select experiments where large and flat areas were needed (e.g., in dynamic drag testing). To achieve this, a flexure-based goniometric stage was designed using the Freedom and Constraint Topologies methodology[1]. Three micrometer drives provide three independent actuation points, resulting in tip, tilt, and piston degrees of freedom. However, the stepper- and piezo-driven micropositioning stage that sits atop the goniometric stage feature Z-direction piston movement, so this degree of freedom was redundant. The Solidworks design is shown in Figure 15. The structure was produced from parts cut out of 1/8”-thick aluminum sheeting on a waterjet cutter, as shown in Figure 16. The final assembly is positioned between the three-axis micropositioning stage and the long-travel breadboard below, as shown in Figure 17.

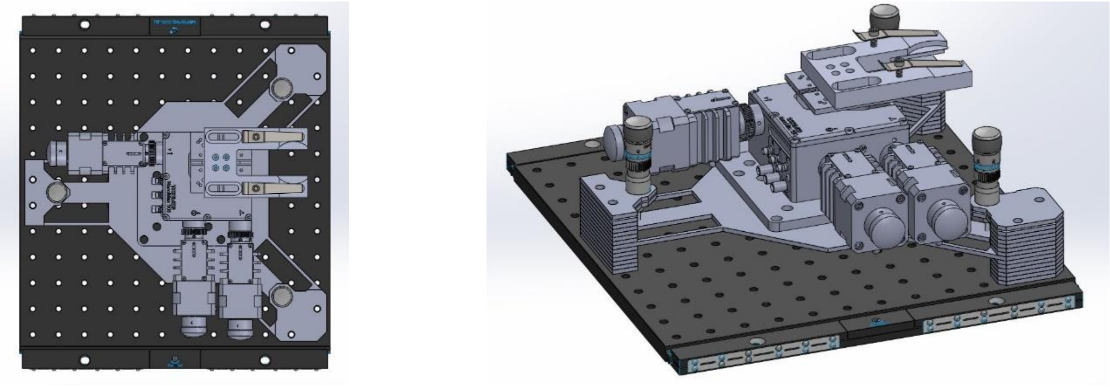

Figure 15: Solidworks part files for the goniometric micropositioner

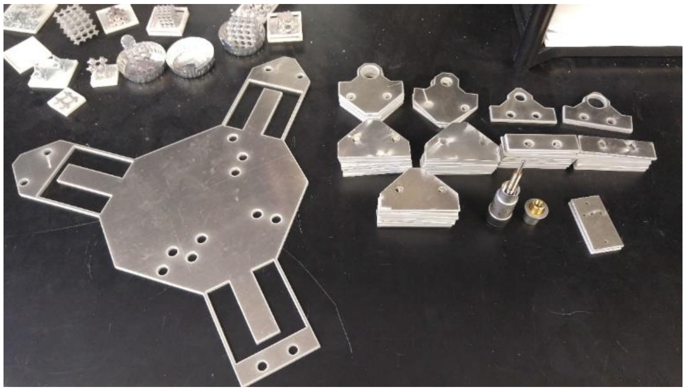

Figure 16: Pre-assembled goniometric micropositioner

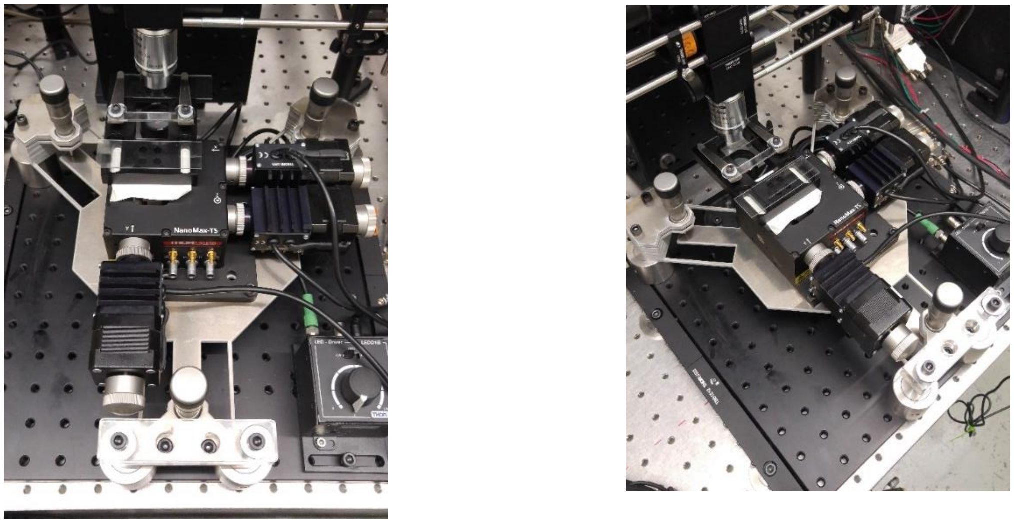

Figure 17: Installed goniometric micropositioner

2.2.5 Microfluidic Dispensing System

The HOT system also includes an optional system for driving microfluidic flow through a sample chamber via a programmable syringe pump (Chemyx Fusion 100) and custom microfluidic chips (Figure 18). The syringe pump is integrated in the MATLAB control software describe in Appendix B.

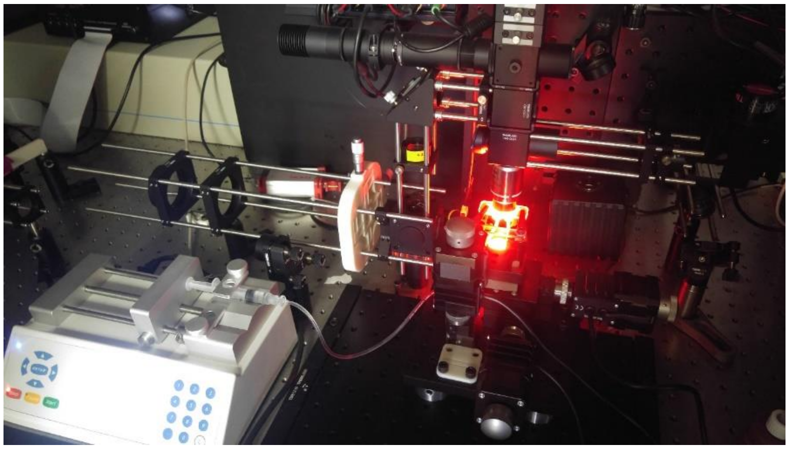

Figure 18: Photo of the microfluidic dispensing system in use

Traditional microfluidic devices often require cleanroom-based lithographic procedures, chemical etching, and tightly-controlled bonding[97] to create microscale channel geometry. However, many HOT experiments only require straight and shallow channels (i.e., less than 100µm) while the width and length do not need to be tightly dimensioned. This work used a rapidly-prototyped custom microfluidic chip consisting of a laser-cut acrylic substrate and coverslip separated by a single piece of 50µm-thick double-sided tape. The double-sided tape features a hand-cut pattern that can be tailored to a specific application (e.g., single-channel delivery or multi-channel fluidic mixing). Fabrication steps for the rapid-prototyped chip are summarized in

Table **4**.

Table 4: Steps in rapid prototyping of tape-based microfluidic chips

Step	Description	Equipment needed
1	Cut an acrylic substrate that is roughly the same size as a traditional microscope slide. The substrate should feature inlet and outlet through-holes that are wide enough to accommodate tubing or a tubing adapter.	Laser cutter (e.g., Trotec Speedy100 60W)
2	Cut a channel mask from regular printer paper. The mask should have the same planar geometry as the desired channel features, including the inlet and outlet ports.	Laser cutter or scalpel
3	Place the channel mask over the acrylic substrate, lining up the inlet and outlet features. Adhere a piece of double-sided tape over the mask, leaving the tape backing on the outside.	Double-sided tape
4	Using a scalpel, score the double-sided tape along the perimeter of the tape mask. Remove the paper mask and the double-sided tape attached to it.	Scalpel
5	Remove the backing from the outside of the double-sided tape and adhere a coverslip over the channel. Ensure that the coverslip has bonded around the full channel geometry by illuminating the glass at an angle.	Coverslip

Although this work uses such particles in a rapidly-prototyped custom microfluidic chip, the experimental methods of this paper are compatible with a variety of particle types and microfluidic devices[98].

Chapter 3

Simultaneous Handling with Scanning Holographic Optical Tweezers

The aim of this chapter is to introduce a new optical-tweezers approach, called scanning holographic optical tweezers, which drastically increases the working area of the HOT approach while maintaining tightly focused laser traps. A twelve-fold increase in working area is demonstrated. The SHOT approach achieves its utility by combining the large working area of the SOT approach with the flexibility of the HOT approach for simultaneously moving differently structured optical traps in and out of the focal plane. This chapter also demonstrates a new heuristic control algorithm for combining the functionality of the SOT and HOT approaches to efficiently allocate the available laser power among a large number of traps. The proposed approach shows promise for substantially increasing the number of particles that can be handled simultaneously, which would enable optical-tweezers additive-fabrication technologies to rapidly assemble microgranular materials and structures in reasonable build times.

3.1 Motivation

In the past few decades, two primary approaches (i.e., the SOT and HOT approaches) have been pursued as a means of increasing the number of particles that can be handled simultaneously using optical tweezers. The SOT approach typically relies on a 2D mirror galvanometer or an acousto-optic modulator (AOM) to periodically time-share a single focused laser beam among multiple trapped particles more rapidly than the particles can diffuse due to Brownian motion[77,78]. Although this approach can achieve a large working area (WA), it is limited to Gaussian traps within the focal plane. In contrast, the HOT approach uses a computer-controlled SLM to divide a single input beam into multiple continuously powered optical traps[34,40]. Although this approach can construct a diversity of structured traps beyond Gaussian[36,41] and these traps can be moved in and out of the focal plane, the HOT approach is limited by a proportional relationship between its largest WA and its smallest achievable trap size.

The purpose of this chapter is to introduce a new approach, called scanning holographic optical tweezers (SHOT), which combines the strengths of both the SOT and HOT approaches for simultaneously handling particles while overcoming their limitations. The SHOT approach generates dynamic trapping holograms using a phase-only SLM, and it rapidly time-shares those holograms by periodically scanning them across the WA using a 2D mirror galvanometer. The SHOT approach drastically increases the overall reach (i.e., the WA in which microparticles can be handled) of current optical-tweezers systems while maintaining sufficiently small trap sizes and while permitting a diversity of structured traps (e.g., optical vortices[36]) that can be moved in and out of the focal plane. Although others have demonstrated impressive dynamic handling of 10s of particles simultaneously using other optical-tweezers approaches[99,100], this paper utilizes the SHOT approach for the first time to demonstrate the dynamic handling of similar numbers of particles simultaneously but within significantly larger WAs (>12 fold).

This increase in simultaneous particle handling, coupled with a suitable method for particle joining[55,56], could enable an advanced optical-tweezers additive-fabrication technology[55,64] that could assemble practical volumes of custom engineered microgranular crystals[14,101] in reasonable build times. The closely packed spheres that constitute these crystals give rise to nonlinear dynamic properties that are favorable for controlling stress waves that propagate through the crystal's lattice[102]. An optical-tweezers approach similar to SHOT could enable the flexibility necessary to fabricate sophisticated designs while still achieving large volumes in reasonable build times.

3.2 Heuristic Grouping Algorithm

The SHOT approach generates different groups of time-shared hologram traps by synchronizing a phase-only SLM with a 2D mirror galvanometer. The SLM divides a laser beam into multiple optical traps and the galvanometer directs these traps to a desired location within the WA to temporarily trap a group of corresponding particles. The SLM then divides the laser beam into a new set of optical traps and the galvanometer directs those traps to a new location within the WA to temporarily trap a different group of particles. This process cycles through different groups of particles rapidly such that a time-averaged wide-field trapping pattern emerges that can cleanly trap and handle many particles within a significantly larger WA than could be achieved by the SLM alone. The SHOT approach is graphically depicted in Figure 19 for a scenario where 10 particles are trapped within a large WA. The blue dashed squares shown in the right side of the figure represent the reach of the system's SLM as its different trapping holograms are cyclically scanned to each of the four locations where the particles in each of the groups are trapped. Although the SHOT approach is not the first to use an SLM in series with a galvanometer or AOM[103,104], it is the first approach that synchronizes an SLM with a galvanometer to enable dynamic handling of particles.

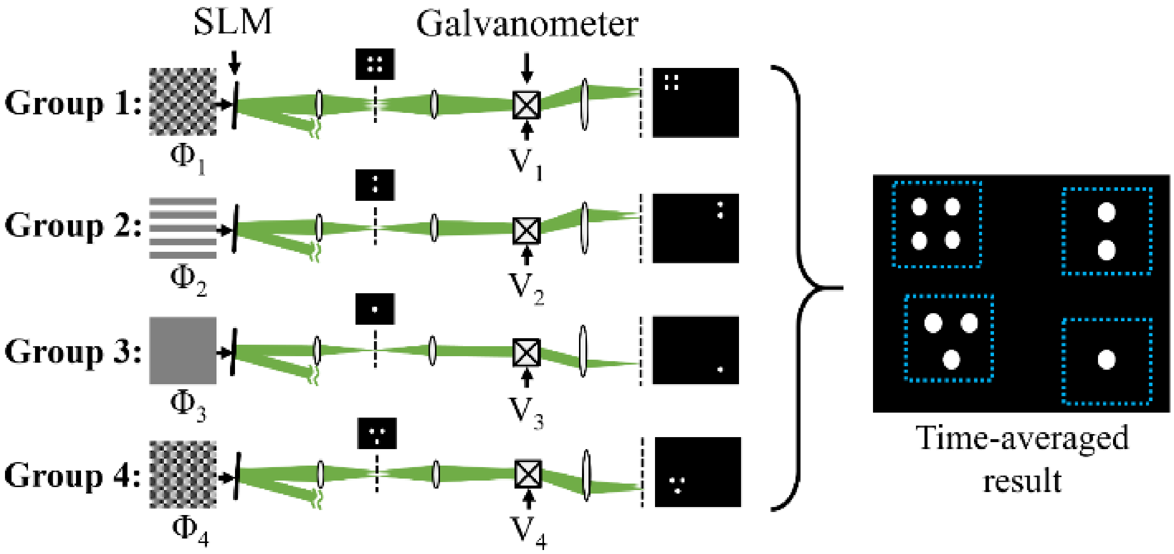

Figure 19: SHOT time-sharing principle

The SHOT approach requires a sophisticated grouping algorithm to computationally coordinate the task of scanning each trap group generated by the SLM for handling all the particles in the WA as efficiently and effectively as possible. To this end, this grouping algorithm should attempt to calculate the minimum number of trap groups necessary for trapping all the intended particles within the WA for a given SLM reach (e.g., the size of all the blue dashed squares in Fig. 1). The algorithm should also determine the location of each of those trap groups as well as attempt to calculate the most efficient sequence in which their corresponding trap holograms should be cyclically scanned. Finally, this algorithm should be computationally efficient to the extent that it can perform its calculations in less time than is required for the SLM and galvanometer to perform the instructions generated by the algorithm (i.e., the algorithm should not be the system's bottleneck so that the hardware can be driven to its limits).

There are many heuristic grouping algorithm solutions that could sufficiently satisfy these requirements for enabling the SHOT approach, but no single algorithm exists for determining the absolute optimal solution for general scenarios. Determining the absolute minimum number of trap groups, for instance, is an NP-hard problem that cannot be solved directly. Although it is possible that a near-minimum solution could be determined by relaxing an NP-hard Boolean linear programming (LP) problem, a different heuristic approach was used for the algorithm of this paper. Additionally, identifying the optimal scanning sequence of trap groups is similar to the well-known traveling-salesman problem (TSP), which currently has no optimal solution and is also NP-hard. Furthermore, note that although traditional grouping algorithms (e.g., k-means clustering[105]) provide efficient solutions for calculating the location of different-sized groups for a given number of groups, the problem that the SHOT-approach algorithm attempts to solve is the reverse problem. Its grouping algorithm should calculate the minimum number and location of groups required to trap all the particles within the WA for a given fixed group size, which corresponds with the SLM's reach. This reach is determined by the number of SLM pixels and the system's 4-f magnification optics, which are fixed values once the system is built.

The heuristic grouping algorithm introduced in this paper rapidly calculates the near-minimum number, n, of trap groups necessary to trap all the particles in the WA as well as the locations of these groups and a near-optimal sequence in which they should be cyclically scanned. This information is produced in the form of *(i)* SLM phase values, Φ_i, for each of the sequentially numbered trap groups labeled 1 through n, and *(ii)* galvanometer voltage values, $V_i=[v_{xi}, v_{yi}]$, that correspond with the x and y coordinates to which the center of the corresponding trap group's square area will be directed by the galvanometer's mirror (these parameters are labeled in Fig. 1).

The algorithm produces this information when given *(i)* the desired locations of every trap in the WA, which is labeled in Step 1 of Fig. 2, *(ii)* the size of the full WA, and *(iii)* the size of the fixed SLM reach. The SLM reach of this paper's system was set to a 50 µm x 50 µm square so that each trap could be focused tightly within the system's full WA. These inputs are provided to the algorithm in the form of a large sparse matrix and a smaller matrix fully filled with ones only. The components of the large sparse matrix represent locations where traps could be placed in the WA. Values of zero within the matrix represent locations where no traps are intended, and values of one represent locations where desired traps are intended. The sparse matrix for our system's WA is a 1024x1280 matrix. Its size is limited by our camera's field-of-view. The components within the smaller matrix filled with ones represent the locations where the SLM could place traps (i.e., it represents the SLM's reach depicted as the grey dashed square in Step 1 of Fig. 2). This matrix is 356x356 for our system's SLM reach.

Once the algorithm receives these matrix-based input values, it performs the steps shown in Figure 20 to calculate its output SLM phase and galvanometer voltage values as discussed in the previous paragraph. Step 1 of the algorithm convolves the SLM's small matrix of ones over the WA's larger sparse matrix to produce a new density-map matrix that possesses the same dimensions as the WA's sparse matrix. Each component within this density-map matrix contains an integer that represents the number of desired traps that would lie within the reach of the SLM if the center of its square area had been placed at the location that corresponds with the component's location within its matrix and the WA's sparse matrix. Step 2 of the algorithm uses this density-map matrix to then assign the location where the center of the first group of holographic traps will be directed by the galvanometer such that the largest number of desired traps will fall within the SLM's reach. This location corresponds with the component of the density-map matrix that is the largest number in the matrix and is near the center of the locations of the other equal-valued components within the same matrix. Once this location is found, a new WA sparse matrix is constructed that is equivalent to the previous sparse matrix but changes the components that correspond with the locations of the traps within the first assigned trap group from one to zero. Step 3 of the algorithm repeats Steps 1 and 2 using this updated WA sparse matrix to find the next trap group that contains the second largest number of desired optical traps. Step 4 of the algorithm continues to iterate these steps until all the locations of the trap groups have been identified and sequentially numbered. Since, however, a scanning sequence with a cycle that begins with the highest density trap group and ends with the lowest density trap group is not likely to be optimally efficient, Step 5 renumbers these trap groups in a clockwise order so the galvanometer repositions its mirror a near-minimum distance between each trap group. Although this clockwise-sequence approach is an acceptable heuristic TSP solution, other TSP heuristic solutions [106,107] with comparable computational efficiency could also be applied to enable the SHOT approach. Step 6 uses the standard gratings and lenses algorithm to rapidly calculate the SLM phase pattern, Φ_i, of each trap group to generate tightly focused traps where they are desired within each group. Step 6 also uses a calibration constant to convert the x and y coordinates of the center locations of each trap group's square area to voltage values, $V_i=[v_{xi}, v_{yi}]$, that drive the pointing direction of the galvanometer so the trap groups can be scanned to their correct locations. The first five steps of the algorithm took our system approximately 1 millisecond per trap group to calculate, and the last step took an additional 2 milliseconds per trap group.

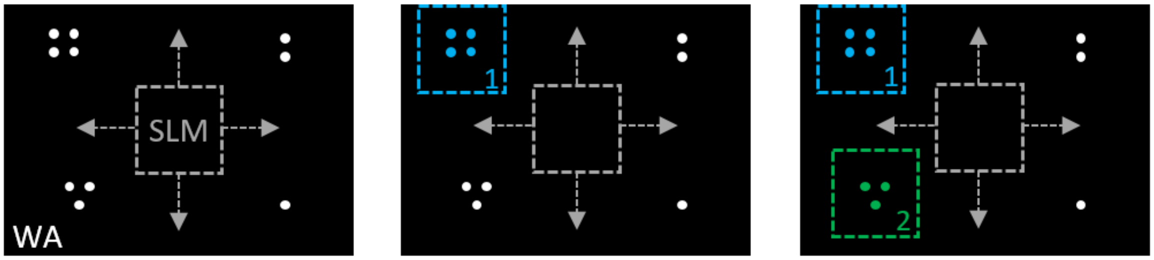

Step 1: Convolve SLM reach matrix over WA sparse matrix

Step 2: Assign location of the first densest group using the resulting density-map matrix

Step 3: Iterate to find the second-densest group using the refined WA matrix

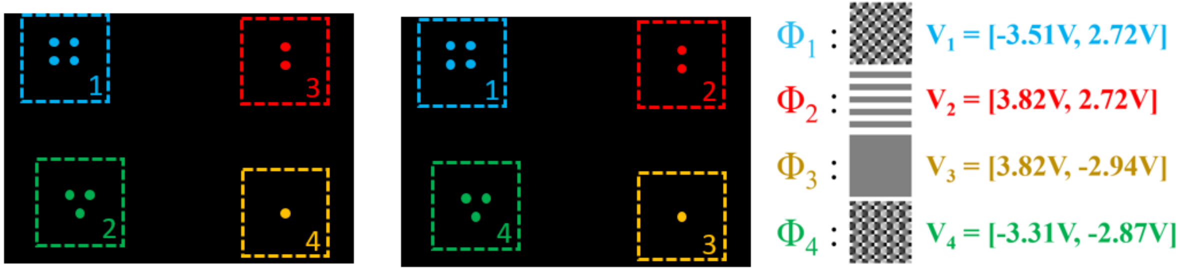

Step 4: Iterate until the locations of all trap groups are identified

Step 5: Reorder the scanning sequence clockwise.

Step 6: Calculate each group's SLM phase and galvanometer voltages

Figure 20: Heuristic grouping algorithm steps for enabling SHOT

For scenarios in which multiple traps need to be moved within a large WA for simultaneously repositioning particles from one configuration to another, an additional strategy was implemented to improve the computational speed of the SHOT algorithm by as much as 50%. The strategy utilizes information pertaining to previously calculated trap groups so that only groups that possess moving traps are updated with new SLM phases and galvanometer voltages. The algorithm conducts a full system update (i.e., the steps of Fig. 2 are performed on every trap within the WA) after every 10 such partial updates to allow the traps to occasionally switch to other more favorable groups and scanning sequences.

The SHOT approach should also be configured to scale the dwell time of the holograms on each trap group according to the number of particles within that group. In this way, the average power allotted to each particle in high-density trap groups will be similar to the average power allotted to each particle in low-density trap groups so that every particle in the WA can be handled using similarly stiff traps. The dwell time for each trap group within our system is scaled to 5 milliseconds per particle within its group. If more than 10 particles are in any one group, the group is divided into smaller groups so that no group's dwell time is long enough to allow particles in other trap groups to defuse due to Brownian motion. A time-averaged trap uniformity measurement (using a Thorlabs BC106N-VIS intensity profiler) showed the 10-trap, 4-group pattern of Figure 20 to have a uniformity value, *u*, of 0.84, as defined by Eq. 4 in[108].

3.3 Scanning Holographic Optical Tweezers Hardware

The schematic diagram of our current SHOT system is shown in Figure 21 and includes a 256-by-256-pixel phase-only SLM (Boulder Nonlinear Systems HSP0532-256). The 2D scanning-mirror galvanometers (Thorlabs GVS012) are driven by 14-bit, ±10 V analog outputs from a standard USB data acquisition card (NI USB-6001). They offer a minimum scanning-step size of approximately 43 nm at the focal plane of the 100x oil-immersion microscope objective.

Scanned holograms are able to reach a 200-µm-diameter circular region, which is limited by the objective lens, while the 20x camera is able to view a 210-by-180 µm region. The positioning accuracy of the SLM is approximately 350 nm, but the system's overall positioning accuracy is approximately 750 nm due to Brownian motion. Our system's optical efficiency from the laser to the trapping plane (including the first-order diffraction efficiency of the SLM and power lost due to the Fresnel beam block), is 20.5%. The maximum number of traps that can be created with the SHOT approach is primarily limited by the amount of power that reaches the trapping plane. We limited the amount of laser power on our SLM to 1.2 W to avoid damaging its backplane, which translates to a maximum available trapping power of 246 mW. We observed that approximately 5 mW is necessary to dynamically handle a 4-6 µm microsphere at a reasonable speed of ~3 µm/sec. Thus, using our power-limited SLM, our SHOT system is currently capable of simultaneously moving upwards of 50 such microspheres. Typical trap stiffness values for 30 mW traps range between 0.62-1.17 pN/µm. We measured these trap stiffness values using a calibration method that equates particle displacements measured from video feedback to viscous drag forces induced by constant-speed micro-positioning stage motion, and included a Faxén’s law term to account for proximity to the cover slip[109].

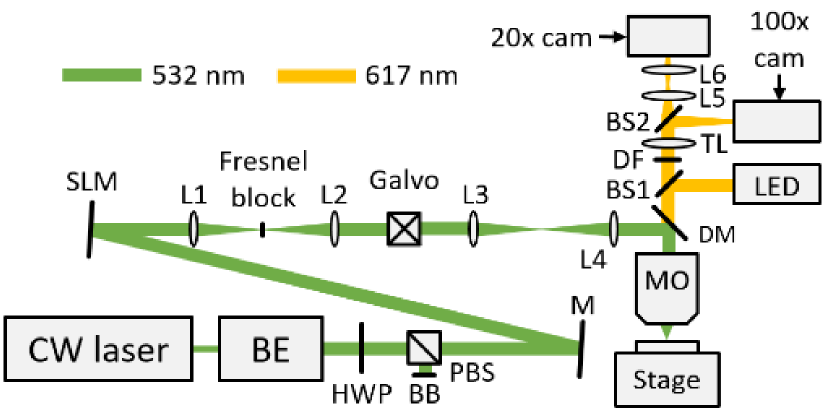

BE: 3x expander
L1: f = 250 mm
L2: f = 250 mm
L3: f = 100 mm
L4: f = 125 mm
L5: f = 100 mm
L6: f = 60 mm
TL: f = 200 mm
MO: 100x, NA 1.45
DM: longpass (λ_c = 567 nm)
BS1: 50-50
BS2: 90-10 (R-T)
DF: ND 6.0 (532 nm)

Figure 21: SHOT system schematic diagram

Particle manipulation was performed within a sample chamber consisting of a standard microscope slide and coverslip separated by two pieces of single-sided adhesive tape with a thickness of approximately 80 μm. The unfunctionalized polystyrene microspheres (Bangs Laboratories, Inc.) were manipulated in an aqueous solution with approximately 0.05% Tween 20 surfactant.

Our system's hardware is controlled by a MATLAB graphical user interface running on a Dell Precision T3600 computer (3.0 GHz quad-core, 12 GB RAM). The SLM and scanning galvanometer are updated to scan between holographic trap groups at rates of 160 Hz. Laser power is diverted away from the trapping plane during galvanometer movements to prevent streaks from appearing in the time-averaged profile. Three steps are conducted to prevent this issue and to enable the SHOT approach: (1) the SLM displays a blank pattern with no lens phase to temporarily steer all laser power into the Fresnel beam block, (2) the galvanometer angle is updated, and (3) the group's trapping phase pattern is sent to the SLM with a superimposed lens phase. Capture of user input commands and calculation of system control actions including the grouping algorithm described previously are performed in separate functions so that the SLM and galvanometer update loop runs in parallel for achieving high system efficiency.

3.4 Results

The SHOT system was used to produce a series of real-time screen shots of various particles being trapped and manipulated to form ordered configurations using the SHOT approach, as well as the ability to capture free-floating particles for directing the self-assembly of desired bulk configurations over large WAs (Figure 22). The approach was able to simultaneously trap and handle multiple particles within a WA that is more than twelve times larger than the reach of its SLM.

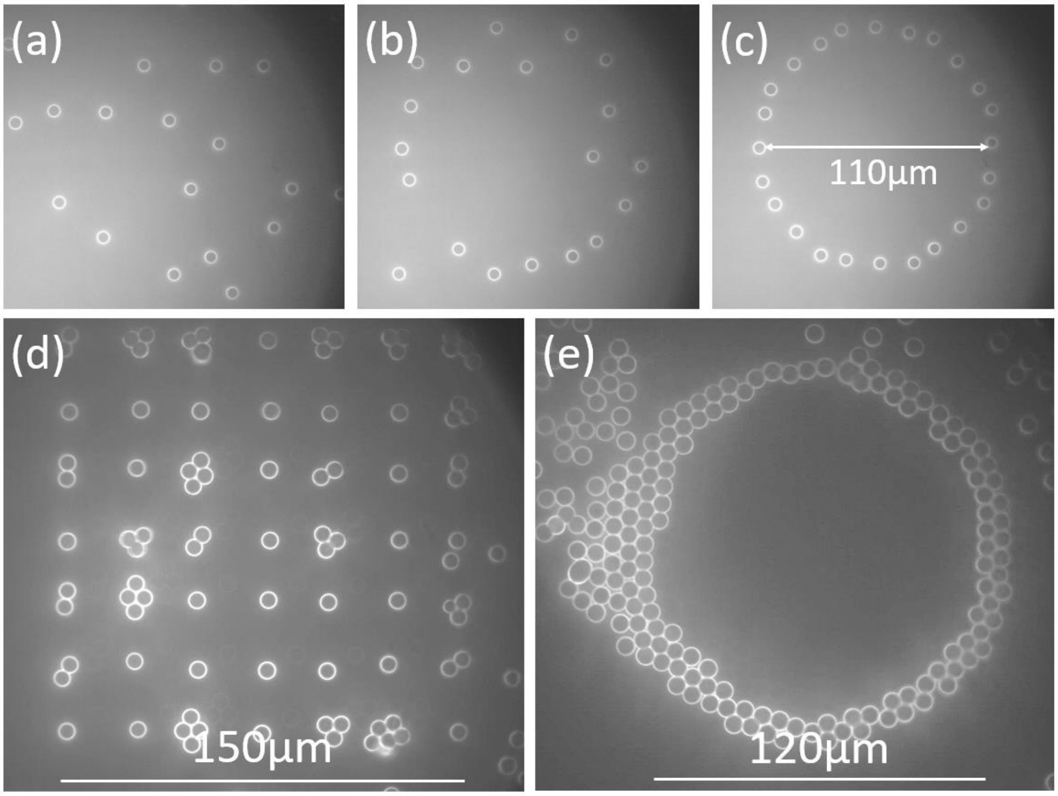

Figure 22: 4.2μm-diameter polystyrene microspheres positioned by the SHOT approach

In this chapter, the SHOT approach was introduced, which combines the strengths of the SOT and HOT approaches for generating large numbers of time-shared tightly focused traps of any optical structure that can be moved in and out of the trapping plane over a significantly larger WA than is possible using the HOT approach alone. A grouping algorithm is introduced for efficiently coordinating the SLM and scanning galvanometer to enable the SHOT approach and details pertaining to our system are provided.

Chapter 4

Path Planning and Automation of Holographic Optical Tweezers Systems

The purpose of this chapter is to introduce three improvements to automated holographic-optical-tweezers systems that increase the number and speed of particles that can be manipulated simultaneously. First, addressing path planning by solving a bottleneck assignment problem can reduce total move time by up to 30% when compared with traditional assignment problem solutions. Next, a new strategy is presented to identify and remove undesired (e.g. misshapen or agglomerated) particles. Finally, a controller that combines both closed- and open-loop automation steps is shown to increase the overall loop rate and average particle speeds while also utilizing necessary process monitoring checks to ensure that particles reach their destinations. These improvements are used to show fast reconfiguration of 100 microspheres simultaneously with a closed-loop control rate of 6Hz, and 10Hz by employing both closed- and open-loop steps. Additionally, this presented approaches are used in the closed-loop assembly of a large pattern in a continuously-flowing microchannel-based particle-delivery system.

4.1 Motivation

The purpose of this chapter is to introduce three improvements that can be applied to automated HOT systems to improve throughput: (1) efficient path planning via solutions to the bottleneck assignment problem (BAP), (2) a new strategy for identifying and sorting undesired particles, and (3) utilization of both closed- and open-loop automation steps, which can increase speed while still ensuring that particles reach their destinations. This work is important because it simplifies the system operator's task of highly-parallelized coordination of large numbers of objects, thereby improving HOT's potential as a viable method for microfabrication.

This work had three primary goals in formulating a controller for high-throughput HOT-based assembly: *(1)* to incorporate closed-loop process monitoring so that particles are sure to reach their destinations, *(2)* to route particles along efficient (i.e. minimum time) paths, and *(3)* to utilize rapid computations that can be scaled to many particles in parallel. However, no previously-published works have achieved these three conditions simultaneously. Numerous examples of open-loop reconfiguration processes have been demonstrated that leverage pre-computed holograms[100,110], but these controllers are not robust to environmental perturbations like collisions or ambient microfluidic flow within the sample chamber. Closed-loop controllers have been presented using A-star[111] or D-star-lite[112] path planning algorithms to route particles to their destinations, yet these approaches have not been scaled beyond three particles in parallel due to the computational complexity of the path planning algorithms. A closed-loop flocking controller applied to a HOT system was demonstrated for sorting visually-different particles[113,114], and although this control scheme avoids collisions, it does not continually track a minimum-time solution. Finally, a specialized control scheme was developed for using microspheres for indirect pushing of single biological cells[115], but the approach presented in our work assumes the ability to directly manipulate microparticles, which allows for a greater number of particles to be handled simultaneously.

Our approach was inspired by Chapin and colleagues, who first demonstrated efficient closed-loop heuristic algorithms for assembling and sorting up to 25 microspheres[116]. Chapin's controller featured particle recognition, path planning, collision avoidance, and wavefront design at each step with control loop rates less than 3Hz. Our approach uses a similar controller structure, but we demonstrate improvements in detection, path planning, and overall computational efficiency that enables a four-fold increase in the number of particles handled simultaneously (i.e. 100 microparticles in parallel) and a two-fold improvement in controller loop rate (i.e., 6Hz, including calculating minimum-time paths at each closed-loop step).

4.2 Control Algorithm

We now discuss the five steps of the closed-loop automation algorithm (Figure 23a) that organizes a random dispersion of microparticles into a desired pattern. All computations are performed in MATLAB on a desktop computer (3.0GHz quad-core, 12GB RAM) with a built-in graphic processing unit (GPU; GIGABYTE GeForce GTX 1060, 3GB).

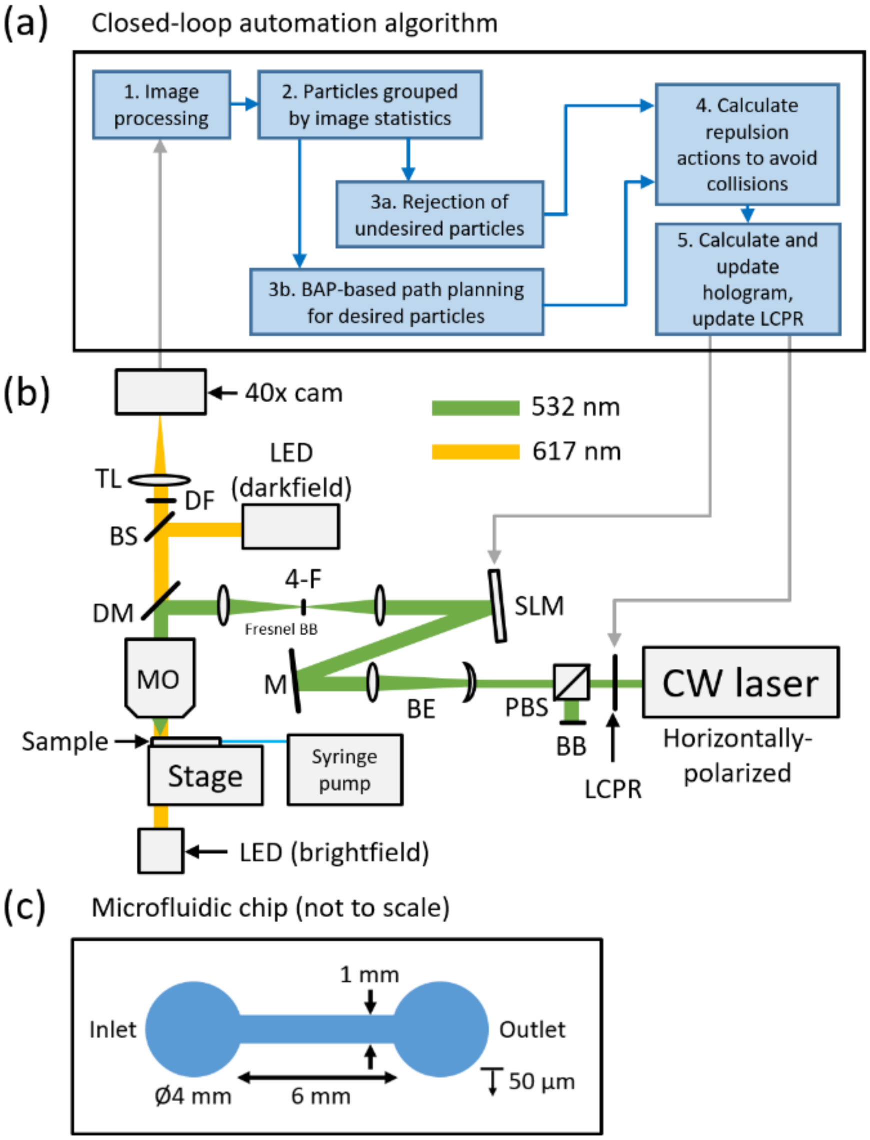

Figure 23: Automation algorithm and HOT system, including microfluidic chip.

The automation algorithm's first step involves performing a GPU-based image processing routine to detect all visible particles. The image processing routine proceeds as follows: *(1)* an image is captured from the system's 40x camera (Figure 24a), *(2)* a low-pass-filtered image is computed (Figure 24b), *(3)* the low-pass-filtered image is subtracted from the original captured image to increase contrast against the background signal (Figure 24c), *(4)* the background-subtracted image is converted to a binary format via thresholding (Figure 24d), and *(5)* MATLAB's *imfill* flood-fill operation is used to create filled features (Figure 24e). From the final filled image, MATLAB's *regionprops* command returns centroid location, area, and perimeter values for each detected particle. Using our GPU with this approach, upwards of 250 particles can be detected in less than 50ms.

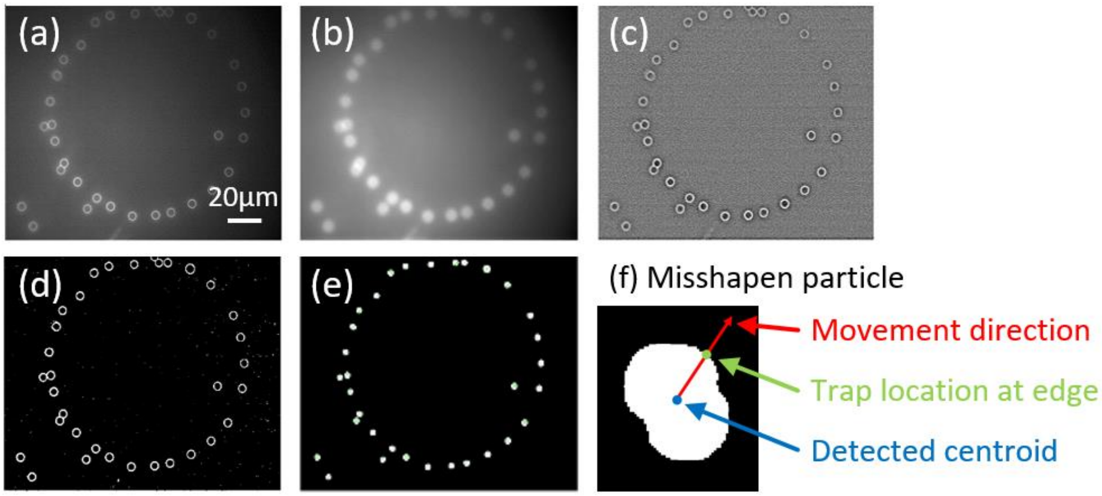

Figure 24: Steps in the particle detection and removal process

The automation algorithm's second step (Figure 23a) involves screening particles of uniform size and spherical shape. This step is important in the fabrication of microgranular structures, which are highly dependent on the morphology of the constituent components[117]. Stock solutions of polymer microspheres are readily available, but a range of particle diameters is present within each sample as well as aspherical shapes that result from manufacturing defects and stochastic microparticle agglomerations. Using the particle statistics calculated from the image processing routine (i.e., centroid location, area, perimeter values), the automation algorithm groups all detected particles into sets of either desirable (i.e., uniformly sized and spherical) particles or undesirable (i.e., misshapen or agglomerated) particles. The algorithm screens for undesirable particles according to whether they satisfy any one of three conditions: *(1)* the particle's detected area in the image is outside the bounds of an expected threshold range, which indicates unacceptably small, large, or agglomerated particles, *(2)* the distance between the particle and its closest adjacent particle is below an expected value (i.e. less than or equal to two particle radii from centroid-to-centroid), which indicates agglomeration, or *(3)* the particle's circularity ratio is less than 0.9 (circularity is computed as $4\pi A/P$, where A is the particle's image area and P is the particle's perimeter), which indicates unacceptable particle deformity. This approach calculates particle diameters with single-pixel precision (i.e., 122nm).

The automation algorithm's third step (Figure 23a) involves assigning directional movement vectors to particles deemed undesirable or desirable. Particles deemed undesirable are removed from the SLM's working area by displacing them in a direction radially outwards using an optical trap placed near the edge of the particle. We rely on the empirical observation that optical traps placed at the edges of the semi-spherical deformed particles produce similar trapping behavior[118] as that suggested by Mie-regime optical trapping simulations of spherical particles[119]. To locate the edge of an aspherical particle, the automation algorithm computes a vector from the particle's centroid facing outwards from the center of the SLM's working area. The algorithm subsequently locates the intersection between this vector and the edge of the detected particle's profile in the binary filled image and places an optical trap at this location (Fig. 2f).

The automation algorithm's third step (Figure 23a) simultaneously computes how desired particles will be assigned to destination locations in the final pattern (e.g., the assembly process in Fig. 3a). An assignment of trapped particles to respective destinations can be reached by solving an assignment problem (AP), which produces a matching between initial particle locations and desired final destinations that minimize a cost function. One common AP approach is the well-established Hungarian algorithm[120] (Figure 25a), which minimizes the total distance travelled by all particles from their initial to final locations. However, since particles move at a constant average speed, our automation algorithm instead reduces overall move time by solving a bottleneck assignment problem (BAP) to minimize the longest single path (Figure 25a). BAP solutions require a few extra milliseconds to compute when compared with the Hungarian algorithm, but the BAP solution's longest single path can be up to 30% shorter than that of the Hungarian algorithm for the same inputs as shown in Figure 25a. The BAP approach[121] computes rapidly enough to run at each closed-loop automation step (e.g., 39ms for the 100-particle pattern in Figure 25b) meaning that the automation algorithm is able to recalculate an optimal minimum-move-time assignment set even in the presence of environmental perturbations. From the calculated assignment set, each particle is assigned to move along a straight path towards its corresponding destination.

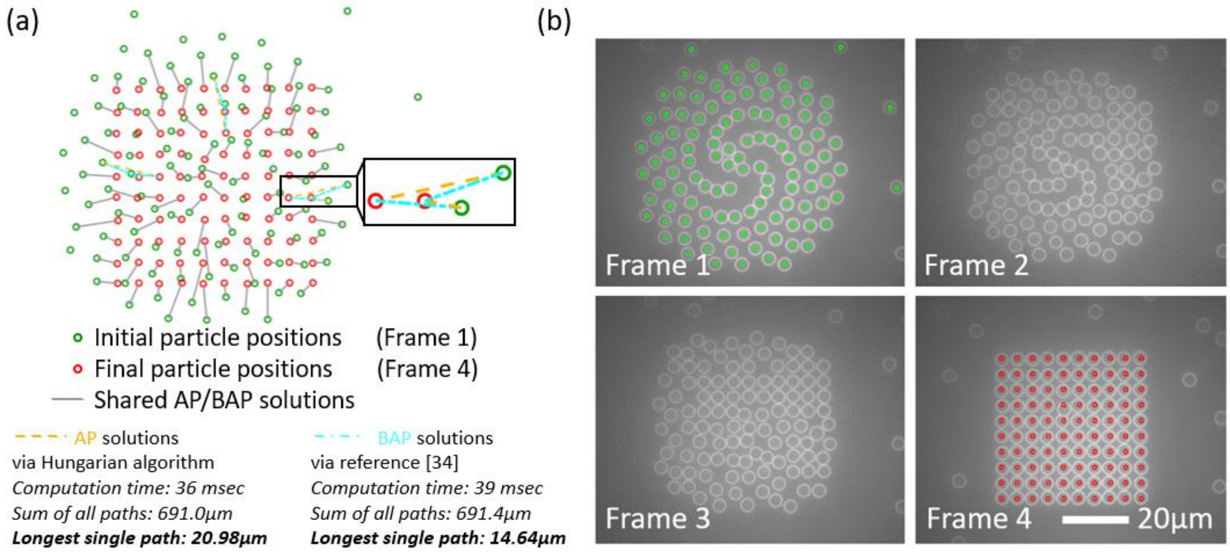

Figure 25: A comparison of the AP and BAP approaches

The automation algorithm's fourth step (Figure 23a) calculates a repulsive direction vector between adjacent particles to prevent their collision. To perform this calculation, a cost matrix is computed where each matrix entry, *(i, j)*, represents the Euclidean distance from the centroid of detected particle *i* to the centroid of detected particle *j*. The algorithm uses the off-diagonal elements of the cost matrix to identify any particles that have approached each other within a threshold of three particle radii and then computes an equal-and-opposite repulsive direction vector for these adjacent particles. This repulsive direction vector is summed with the directional movement vectors (i.e., those generated in the third step of the automation algorithm) to determine the actual direction in which each particle will advance for each algorithm iteration.

The automation algorithm's fifth and final step (Figure 23a) computes updated trap locations for each particle, calculates a corresponding hologram using the standard Gerchberg-Saxton algorithm[82] with three iterations, and updates the LCPR to scale the laser power to the number of active optical traps required. The control loop continues until all the particles reach their desired destination.

Since the automation algorithm is limited to discrete trap steps of one particle radius, the control loop must be run at faster rates to generate an increase in average particle speed. To improve the loop rate, the controller utilizes two open-loop steps (i.e., no detection or path planning step, but only collision avoidance and hologram calculation) followed by a single closed-loop step. The closed-loop automation steps run at 6Hz and ensure that particles reach their destinations via process monitoring, while the open-loop steps execute at 15Hz and produce faster average particle speeds. When used in a 1:2 ratio of closed to open-loop steps, the controller runs at an average rate of 10Hz. Using this approach with step sizes of 1.5µm for spherical particles, individual particle speeds were observed to reach approximately 15µm/sec.

4.3 Results and Discussion

This section demonstrates the performance of the reported automation algorithm. The controller was able to quickly reposition 44 particles from an initial ring arrangement to a final pattern consisting of two concentric circles in only 5 seconds (Figure 26a-b). Each optical trap used 2.5mW of power. The algorithm achieved a high degree of positioning accuracy (approximately 120nm), which was primarily limited by the SLM, and precision (approximately 500nm), which was primarily limited by the particles' Brownian motion. The HOT approach offers a high degree of spatial control when fabricating arbitrary arrays of microparticles, which provides a promising alternative to traditional self-assembly approaches[65,122].

The automation approach was also used to fabricate a “UCLA” pattern while simultaneously clearing excess particles from the working area by assigning destination locations at the top of the SLM’s working area (Figure 26c-d). The 42-particle pattern was formed and excess particles were removed within 12 seconds. The ability to achieve a desired final pattern while clearing excess particles may enable automated HOT systems to fabricate defect-free microgranular lattices[117], photonic crystals[123], or other microscale optical components composed of microparticles[124,125].

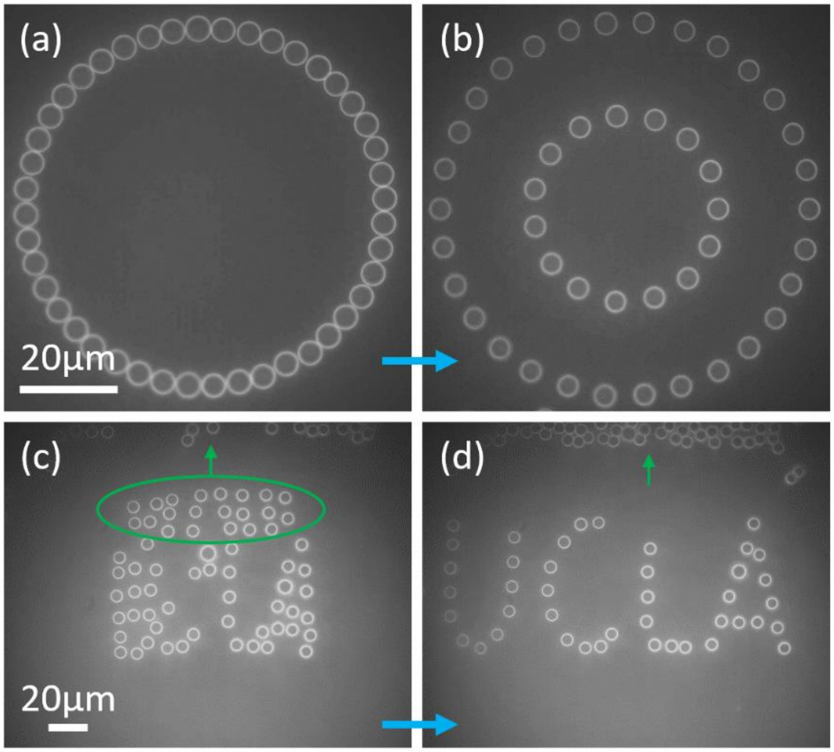

Figure 26: Reconfiguration of circular and “UCLA” patterns

The automation algorithm was also used to reconfigure particles through a series of shape changes (Figure 27). The algorithm is run until each desired shape is formed and then the control loop restarts for the next desired shape in the sequence. A video of the reconfiguration sequence is provided in the Supplementary Materials section. Vacancies in the desired patterns (e.g., in the outer perimeter of the *8* pattern) resulted from using a set of destination coordinates that was not adapted to the number of particles available. Future research will allow the automation algorithm to resample a complex shape into uniformly-spaced coordinates based on the number of available particles. The ability to continuously reconfigure particles into a time-varying target array may allow automated HOT systems' to use large groups of microparticles to indirectly manipulate multiple biological cells or other sensitive objects[115,126,127].

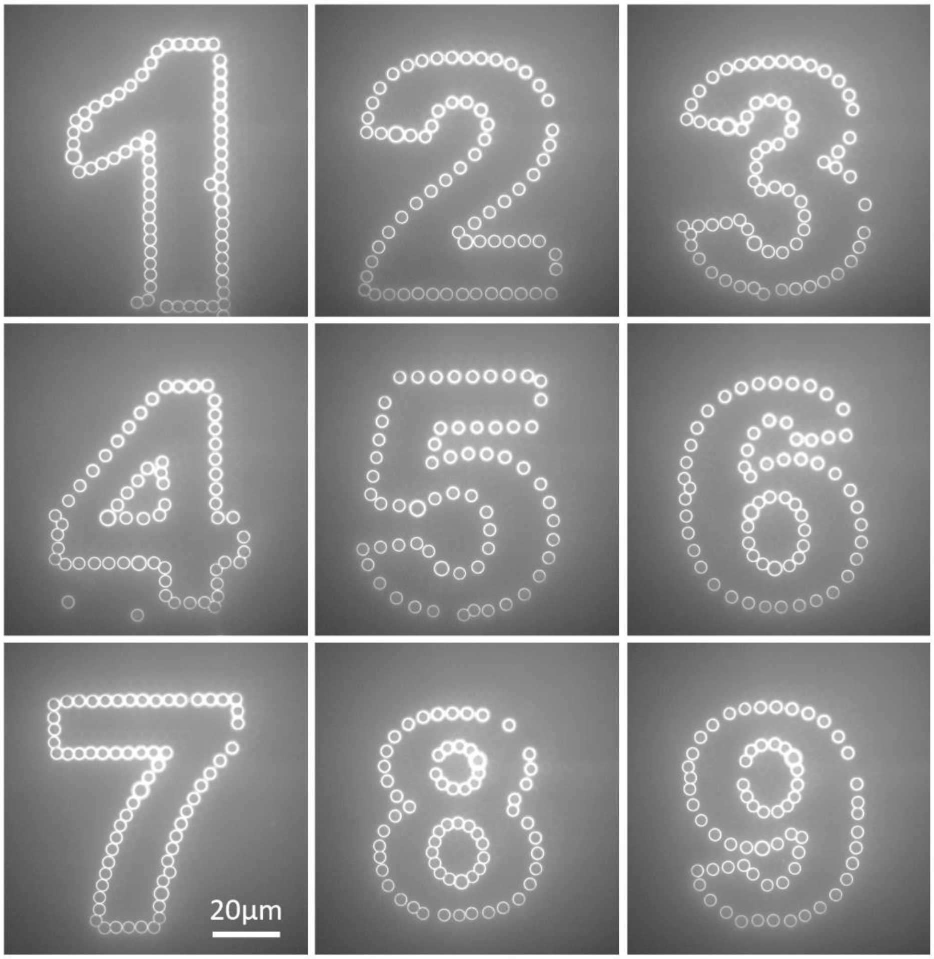

Figure 27: Nine-pattern number-shaped reconfiguration sequence

The automated HOT system was also used with a microfluidic channel (Figure 23c) to form a real-time continuous-assembly system. A desired rectangular-grid pattern is continuously reconfigured as new microparticles flow into the SLM's working area (Figure 28). The microparticles were held stationary with respect to the flowing medium (v_{medium} = 5µm/sec) using 2.5mW optical traps. Utilizing additional power per optical trap may enable the HOT system to hold particles stationary in faster microfluidic flow, thereby increasing the rate of particle delivery.

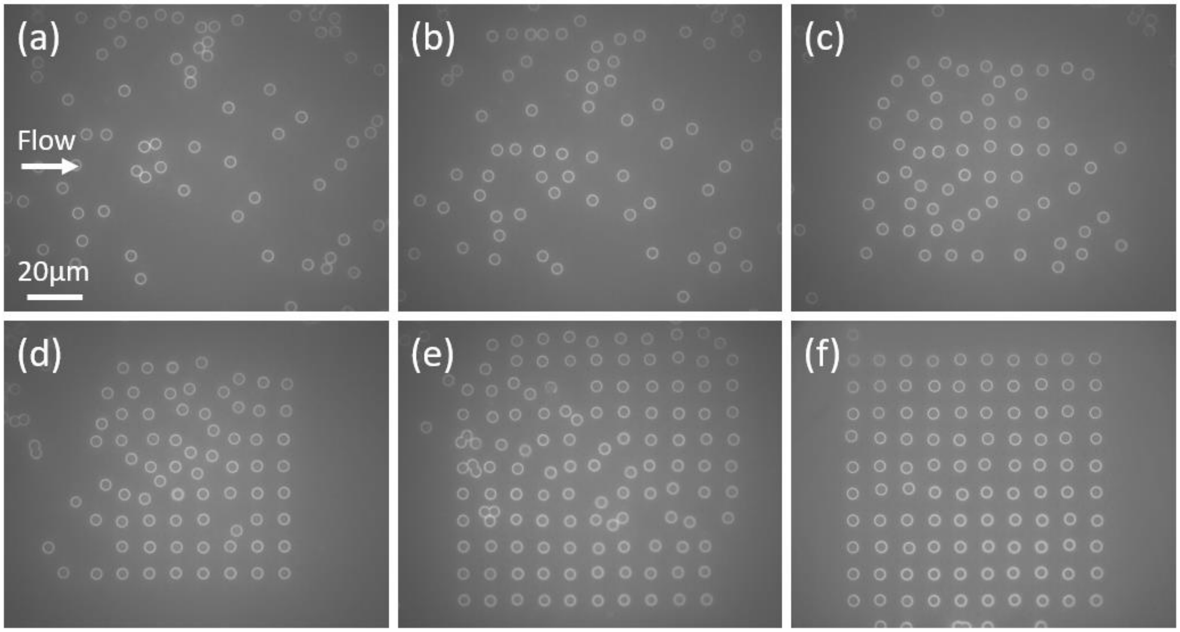

Figure 28: A 10x10 array of microspheres arranged in a continuously-flowing microchannel

If combined with a suitable method for adhering particles[54,55], the proposed conveyor-belt-like microparticle-delivery system holds the potential to enable a continuous assembly system, in which HOT-assembled parts are collected at the outlet of the microfluidic channel. This approach may also be combined with a flow lithography approach[128–130] to simultaneously fabricate, deform, and assemble non-spherical, custom-shaped particles.

This chapter demonstrated three primary advances to automated HOT systems for increasing the number and speed of particles that can be manipulated simultaneously: *(1)* real-time solutions to the BAP minimize the longest single path (thus, reducing move time), *(2)* particle statistics generated via image processing enable a new method to remove undesired particles, and *(3)* a 1:2 ratio of closed-to-open-loop automation steps increases the average controller rate to 10Hz and individual particle speeds to 15μm/sec. The proposed automation algorithms were demonstrated by rapidly reconfiguring up to 100 particles simultaneously (with new patterns typically formed in 5-20 seconds). Additionally, in contrast to existing microchannel-based sorting approaches[27,131], this work represents the first automated arrangement of microparticles in a microchannel-based particle-delivery system.

The automation approaches presented in this work are readily adaptable to 3D manipulation of microparticles[87,132,133]. Future research will enable layer-by-layer additive fabrication of microgranular structures by combining the 3D Gerchberg-Saxton phase retrieval algorithm[87], 3D microparticle detection[134], and a suitable method for joining particles[55].

Developments in automation continue to advance HOT's prospects as a viable means for scalable fabrication of microgranular structures[117,135] and micro-optical components[124,125], or as a means to manipulate multiple biological cells[115,126,127] and micro-tools[60,136] in parallel. Furthermore, combining an automated HOT system with a microfluidic channel may enable conveyor-belt-like fabrication of intricate micromechanisms[54,63].

Chapter 5

Control via Modeling

To scale the HOT approach to simultaneously handle more particles at faster rates, it is essential to qualitatively and quantitively understand the nature of the forces created by an optical trap and how to best apply them for reliable particle handling. There has been a considerable amount of OT theory developed over the past fifty years[137–141], yet few analytical and modeling efforts have been formulated to specifically investigate the dynamics of particles in the discretely-stepped optical traps found in HOT system.

As previously discussed in Chapter 2, a tightly-focused laser beam creates a stable potential well in which transparent microparticles become trapped[142]. Trapping of nontransparent (i.e., absorbing) microparticles is also possible[22,52,143] but is outside the scope of this work. The potential well for a plane-polarized Gaussian laser beam is generally axisymmetric and can be evaluated in a coordinate frame consisting of radial and axial components. This work will largely focus on the dynamics that result from the radial optical force profile as in-plane holography[85] and imaging is simpler, more robust, and less computationally efficient than out-of-plane techniques[87,134].

Mie-regime optical force simulations[144] predict an initially linear radial trap stiffness, which changes slope and rolls off at distances greater than approximately one particle radius (Figure 29). The shape of the optical force curve is heavily influenced by many optical system and colloidal properties, including wavelength, numerical aperture (NA), indices of refraction, and M^2 value. Sample radial and axial optical force profiles, and their dependences on NA and M^2 value are shown in Figure 29 (additional properties: D = 6µm polystyrene, $n_{PS} = 1.575$, λ = 532nm, P

= 40mW). As detailed in Ashkin[145], trapping efficiency values, represented by Q_r or Q_z for the radial and axial efficiency respectively, represent the momentum transferred from the trapping laser into force per photon. Efficiency is converted into force (in units of Newtons) using the factor nP/c, where n is the index of refraction, P is the laser power in the optical trap, and c is the speed of light in a vacuum:

$$F_{OT}(r) = \frac{Q_r nP}{c} \tag{10}$$

$$F_{OT}(z) = \frac{Q_z nP}{c} \tag{11}$$

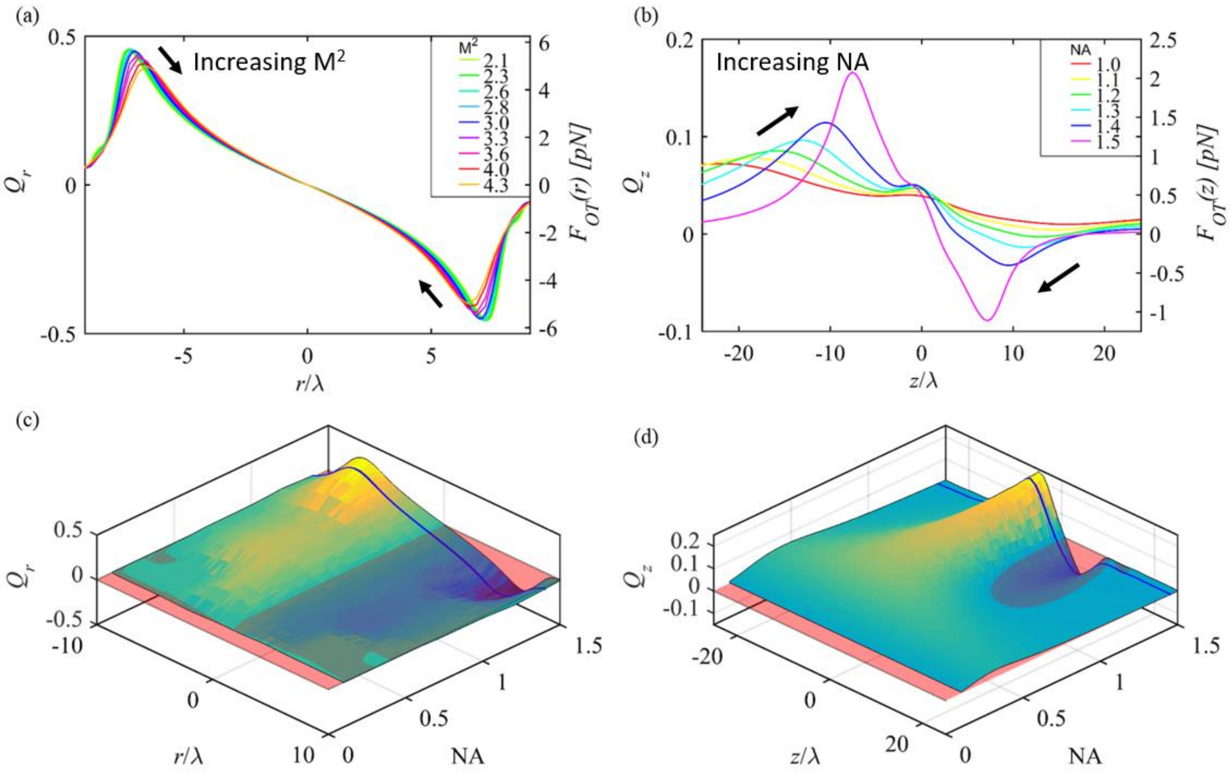

Figure 29: Sample radial and axial optical trapping force profiles (image courtesy M. Porter)

Creating a stable force profile in the axial direction requires higher numerical aperture values than are required for stable trapping in the radial direction. A stable axial force profile is important if particles are to be manipulated axially (i.e., ‘lifted’ or ‘submerged’). If axial stability is not achievable, as is often the case with microspheres in a liquid pre-polymer, then it is important to consider the relative densities of the particles, medium, and the microscope orientation to create conditions for optical trapping (Table 5 summarizes these relationships – the typical operating conditions for the work presented in this thesis are bolded).

Table 5: Microscope orientation, relative density, and trapping stability

	$\boldsymbol{\rho_{particle} > \rho_{medium}}$ **(i.e., particles sink)**	$\boldsymbol{\rho_{particle} < \rho_{medium}}$ **(i.e., particles float)**	$\boldsymbol{\rho_{particle} = \rho_{medium}}$ **(i.e., particles are neutrally buoyant)**
Upright microscope (beam propagates downwards)	**If the radial profile is stable, particles can be trapped against the bottom substrate**	Axial stability is required for reliable trapping	If the radial profile is stable, particles can be trapped against the bottom substrate
Inverted microscope (beam propagates upwards)	Axial stability is required for reliable trapping	If the radial profile is stable, particles can be trapped against the top substrate	If the radial profile is stable, particles can be trapped against the top substrate

The discussions in the sections that follow are limited to optical forces on transparent and spherical microparticles due to their prevalence in HOT experiments. Previously-published literature describes simulations of optical forces on non-spherical[74,146] and non-transparent (e.g., metallic[143,147]) particles but a discussion of these techniques is outside the scope of this work.

5.1 Dynamics of Particles in Constant-Velocity Traps

The nonlinear force profiles created by tightly-focused Gaussian beams allow for stable trapping and manipulation through viscous media. Most of the experiments discussed in this work involved colloidal particles suspended in DI water (which has a kinematic viscosity of approximately 1cP at 20°C), but optical trapping was possible in other media including include various photopolymers (~5-500cP), propylene carbonate (2.5cP), propylene glycol (42cP), and glycerol (934cP). It becomes increasingly difficult to resuspend and manipulate microparticles into media with high viscosities, especially for liquids with viscosities beyond that of glycerol.

Further investigation of particle dynamics will be limited to behaviors in the radial direction, denoted by the state variable x. A simple model of the dynamics of optically-trapped particles can be constructed in a second-order nonlinear ordinary differential equation (ODE) as

$$m\ddot{x} + c\dot{x} = F_{OT}(x - x_{OT}) \tag{12}$$

where m represents the mass of the particle, x_{OT} represents the radial position of the optical trap, and $F_{OT}(x - x_{OT})$ represents the optical force profile discussed above. The coefficient to the first derivative term, c, represents the viscous drag coefficient. This is often represented by a simple Stokes' drag equation, but a more accurate representation is captured by the Faxen's law equation[109]. This equation takes the particle's proximity to the substrate into account as particles in boundary layers will experience increased drag force. Faxen's law is expressed as

$$c = \frac{6\pi\eta R}{1 - \frac{9}{16}\left(\frac{R}{h}\right) + \frac{1}{8}\left(\frac{R}{h}\right)^3 - \frac{45}{256}\left(\frac{R}{h}\right)^4 - \frac{1}{16}\left(\frac{R}{h}\right)^5} \tag{13}$$

where η represents the kinematic viscosity of the fluid, v represents the fluid velocity, R represents the radius of the particle, and h represents the height of the particle from the substrate. The coefficient given by Faxen's law is typically 1-3 times larger than that offered by the Stoke's drag equation, depending on the proximity to one substrate.

Force terms for particle-particle[148] (i.e., F_{DLVO}) and particle-solvent[43,149] (i.e., $F_{Brownian}$) interactions are left outside of the scope of this modelling effort at this time. These terms represent stochastic forces that influence an optically-trapped particle that is trapped at high velocities or discretely-stepped with large step sizes, however, their omission does not change the overall behaviors predicted by the nonlinear ODE-based model. Future research by colleagues within the Flexible Research Group will address their effects.

When optical traps are moved at a constant velocity with respect to the suspension medium, trapped particles reach a steady-state equilibrium position where the magnitude of the optical force balances the viscous drag force in a first-order nonlinear ordinary differential equation:

$$c\dot{x} = F_{OT}(x - x_{OT}) \tag{14}$$

By optically trapping a particle and driving the micropositioning stage to move the sample chamber at a constant velocity, it is possible to map the optical force curve at given trap offsets (i.e., $x - x_{OT}$). Starting at zero velocity and zero time-averaged lag, an increasing micropositioning stage velocity results in a directly proportional increase in lag. This constant stiffness regime is also known as the stable trapping regime (Figure 30) as small perturbations of the particle from the steady-stage lag position result in a restoring force and a return to the equilibrium.

Since each velocity value can be used to calculate a viscous damping force value via the viscous damping equation, the constant-speed drag test method is widely used to quantify and calibrate the effective optical force profile on a microparticle[150]:

1. The micropositoning stage drives the sample chamber at a constant velocity with respect to the optically-trapped particle.
2. The amount of steady-state lag (i.e., the difference in the trap and microparticle positions, $x - x_{OT}$) is recorded.
3. The velocity is converted to a viscous force value via the viscous damping equation (i.e., $F_{drag} = c\dot{x}$, using Eq. (13))
4. The process is repeated for different velocity values until the stable trapping region is established (via a plot of $x - x_{OT}$ vs. F_{drag})

Other methods to measure optical forces have been demonstrated[109,151], but often require hardware like quadrant photodiodes or cannot be readily adapted to HOT systems. It is important to note that because the optical force and viscosity terms are dependent on many system parameters, these calibrations are not universal and are only valid for a given HOT and colloidal system.

As the velocity approaches its maximum speed, the sign of the derivative of the force-versus-lag curve changes sign, and an increase in fluid velocity beyond this point will result in the particle 'falling out' (i.e., lag values where the optical force cannot overcome the viscous drag force and the magnitude of $x - x_{OT}$ will increase monotonically with time). The change in derivative of the optical force profile represents the onset of the metastable trapping boundary (Figure 30). Beyond this location a perturbed particle experiences a non-restorative force that prevents it from settling to the stable equilibrium position when in the presence of viscous drag. Particles at this boundary have an equal likelihood of returning to the stable trapping regime or falling out. When manipulating particles with constant-speed traps, the most reliable drag speed is slightly below the maximum speed, as allowing for some distance between the stable and metastable regions allows for a safety margin against perturbations (e.g., from the effects of Brownian motion or inter-colloidal effects).

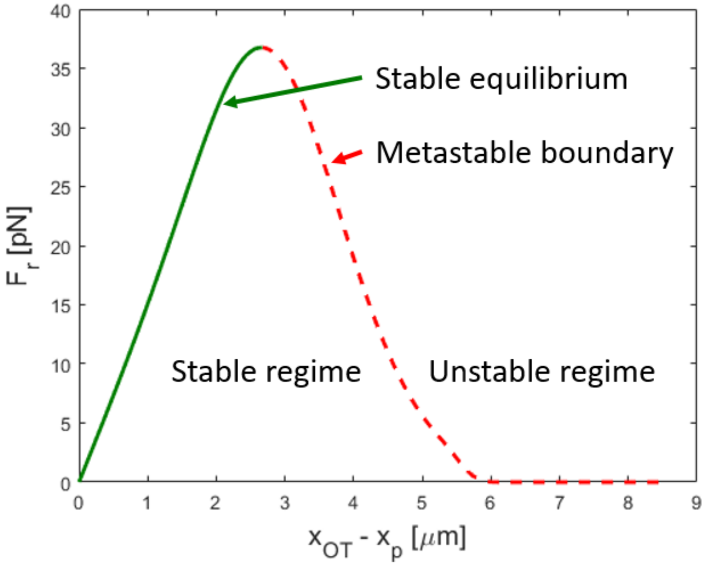

Figure 30: OT dynamic regimes

5.2 A New Method for Measuring the Full HOT Force Profile

The addition of active components like SLMs in HOT[116], scanning galvanometers in SOT[41], or both in SHOT[44] allows for parallelized handling of multiple particles simultaneously, but creates a dynamic environment where optical traps move with discrete steps rather than smooth and continuous motions due to the digital nature of the active components. This creates a unique set of dynamics, as the optical force term in Eq. (12) becomes a series of time-varying step functions. The maximum constant velocity is no longer attainable as the step period increases, as particles experience lower forces as they settle towards the trap center.

However, the ability to instantaneously jump the trap's position enables a new method for mapping out the metastable boundary of the optical force profile. The presented experimental method allows for force-lag mapping on particles of any size, shape, and material. By experimentally measuring the full optical force profile, simulations will better predict empirical HOT operating conditions and simulate operating parameters such as laser power profile, step size, step rate, and colloidal chemistry to fabricate a microgranular lattice, assemble MEMS devices, and actuate microscale mechanisms.

To locate the boundary between the stable and unstable regions (i.e., the metastable boundary in Figure 30), a combination of constant-velocity sample chamber movements and instantaneous trap jumps is used. With an optically-trapped microparticle moving at a given velocity value with respect to the medium, an instantaneous jump of magnitude dr is introduced via SLM, and the camera feed is monitored to determine whether the particle returns to its equilibrium position or falls out. The test is iterated until the largest jump, dr_{max}, is found that results in the particle returning to equilibrium. The values of dr_{max} trace the metastable region of the optical force profile. In Figure 31, the blue circles represent constant-speed drag tests that map the stable trapping region, the green circles represent jump tests in which the particle resettled to an equilibrium lag, and red circles represent jump tests in which the particle fell out of the moving optical trap. The boundary between the green and red circles represents the values of dr_{max}, and a support vector machine[152] was used to fit a curve for the metastable boundary. The data in Figure 31 is provided for a high NA case ($NA_{effective} = 1.23$) and a low NA case ($NA_{effective} = 0.46$)

using 6.0μm-diameter polystyrene microspheres ($n_{PS} = 1.575$) in DI water and 18mW, 532nm optical traps. The magenta 'model prediction' line displays a velocity profile predicted from Mie-regime optical force simulations[144].

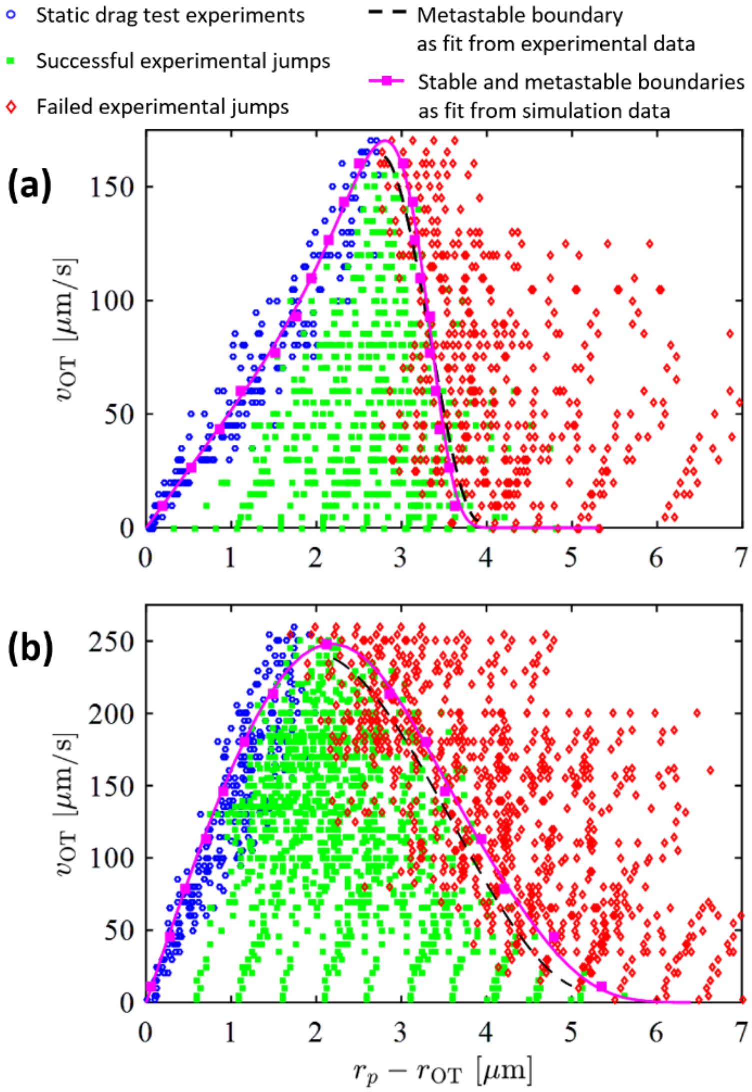

Figure 31: Experimental dynamic trapping results

The metastable boundary (i.e., the boundary between trap jumps in which the particle resettles to its equilibrium position or falls out) is a region that is, in practice, stochastically influenced by both the random nature of Brownian forces[43] as well as inter-colloidal[148] (i.e., DLVO) effects that result from proximity to additional randomly-distributed ambient particles (i.e., $F_{Brownian}$ and F_{DLVO} can either stochastically act along the direction of F_{OT} to help particles settle from a greater jump distance or oppose F_{OT} to cause particles to fall out at short trap jump distances). Understanding the nature of this stochastic region is important for reliably handling particles with discretely-stepped traps (e.g., in HOT or scanning OT systems) as increases in step size can result in a reduction of the probability that particles will resettle into their optical traps.

5.3 Dynamics of Particles in Discretely-Stepped Traps

Using either an analytically-calculated[73] or experimentally-measured optical force profile, we can now provide an empirical optical force term in Eq. (12) and simulate the effects of the discrete-stepping behavior found in HOT, SOT, and SHOT systems. For now, we continue to ignore the effects of Brownian motion[149,153] and intercolloidal forces[148,154] and seek only to explore, for the first time, the general dynamical behavior of colloidal particles in discretely-stepped optical traps.

The second-derivative inertial term of the ODE can be ignored as the inertia of micron or submicron particles is negligible when compared to the viscous drag and optical force terms. As a result, we can study the forcing function as a series of step functions defined only by step period, T, and step size, δ, as defined by

$$c\dot{x} = F_{OT}(x - x_{OT}(t), T, \delta) \tag{15}$$

A MATLAB-based time-stepping simulation was constructed and run for a range of T and δ values with a simulation duration of 1sec and time steps of 1ns.

Parameter sweeps of the T and δ parameters revealed two unique operating regimes: settling and slewing. In this work, the settling regime is characterized by a particle position that travels at least $0.9 \cdot \delta$ in each step period T. The slewing regime is characterized by a particle that can achieve a finite time-averaged lag value (i.e., the magnitude of $x - x_{OT}$ does not increase monotonically with time) but is also outside of the settling regime. The results are summarized in

Table 6.

Table 6: Dynamic operating regimes of particles in discretely-stepped traps (6.0μm-diameter polystyrene spheres and 40mW, 532nm optical traps)

Regime	Definition	Relevant systems	Example time-series plot
Settling	$\min\lvert x - x_{OT}\rvert \leq 0.1 \cdot \delta$	Step time (T): large Step size (δ): variable Typical of most HOT systems, where the rate is limited by SLM hardware	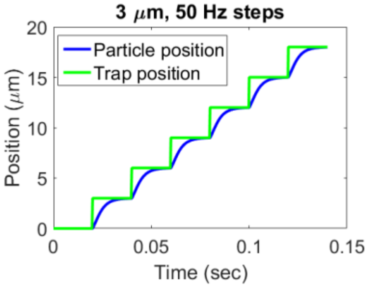
Slewing	$\min\lvert x - x_{OT}\rvert > 0.1 \cdot \delta$	Step time (T): small Step size (δ): small Typical of some SOT systems, where scanning elements can update quickly $\lim_{\delta\to 0, f\to\infty}(\delta/T) = v_{max}$ where v_{max} is the maximum continuous drag speed	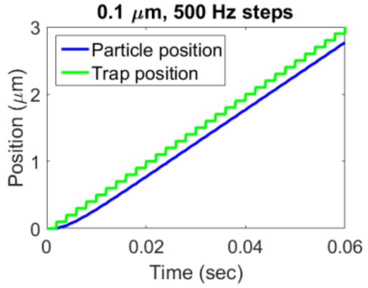
No trapping	$\lim_{t\to\infty}\lvert x - x_{OT}\rvert = \infty$	Step time (T): small Step size (δ): large	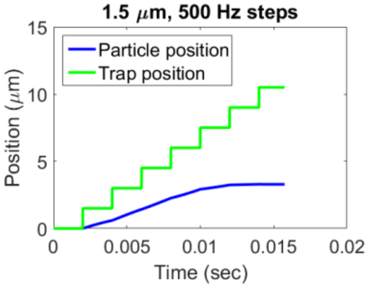

Sweeping T and δ across a wide parameter space (such as in the 4500 simulations in Figure 32) reveals that discretely-stepped optical traps move particles at an average rate that is much slower than constant-velocity traps. In these figures, we use $NA_{effective} = 1.23$, 18mW and 532nm optical traps, and 6.0μm-diameter polystyrene microspheres ($n_{PS} = 1.575$) in DI water. The blue dots represent the slewing regime and the green dots represent the setting regime, as introduced in

Table 6. The region above the 'no trapping boundary' represents a portion of the parameter space where particles cannot be manipulated. Figure 32a shows the operating space with a linear y-axis and Figure 32b shows the operating space with a logarithmic y-axis. In the latter case, we can see that the maximum speed for a discretely-stepped optically-trapped particle occurs when δ and T are small, and the slewing velocity approaches the maximum continuous drag velocity.

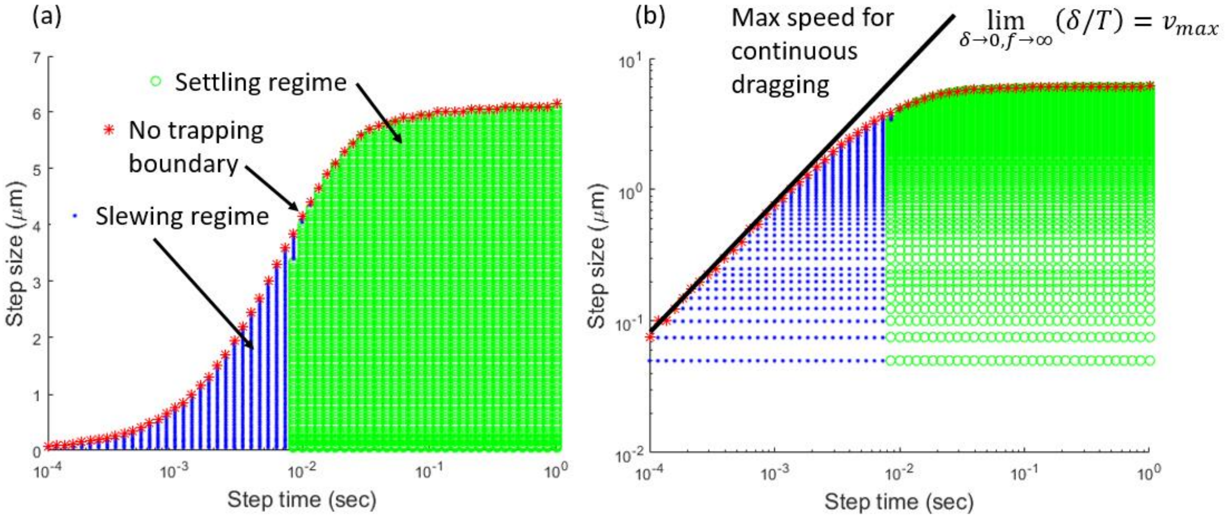

Figure 32: OT operating regimes in T-δ parameter space (6.0μm-diameter polystyrene spheres and 40mW, 532nm optical traps)

Simulating the full T and δ parameter space also provides an important insight about the operating dynamics of HOT systems: the maximum step size is constrained to be less than 1-2 particle radii. Thus, the only means to increase the average speed of discretely-stepped traps towards the maximum continuous-drag speed is to increase the step rate. This fact will be utilized when designing a hybrid open- and closed-loop automation controller in Section 5. Furthermore, these simulations can be performed *a priori* and reveal optimal step sizes for HOT systems with loop periods less than approximately 10ms.

However, the discrepancy in speed between continuously- and discretely-stepped optical traps (i.e., at step times greater than approximately 10ms) can also be addressed by moving multiple discretely-stepped particles in parallel via HOT. Each individual particle then operates within the parameter space shown in Figure 32.

5.4 Limitations of Simulated Force Profiles

To further illustrate the benefits of the experimental test method for mapping the full optical force profile discussed in the previous section over pure numerical-simulation-based approaches, a brief discussion of a few limitations on numerical optical force profile simulations is included in this section. A popular Mie-regime simulation environment based on the T-matrix method of field computation has been presented by Niemenen, et. al.[119], but the optical force profiles produced by the simulation cannot capture certain HOT operating conditions. For instance, the work in this thesis relies on a high-NA oil-immersion microscope objective ($NA = 1.45$, $n_{oil} = 1.52$) immersed in an aqueous medium with a lower index of refraction ($n_{water} = 1.33$). The index of refraction difference between the oil/coverslip system and the water medium gives rise to *(1)* spherical aberrations[155–158] and *(2)* apodization at high convergence angles due to both total internal and Fresnel reflections.

The first effect that is not captured by most Mie-regime simulations is spherical aberration arising from refraction at the coverslip-water interface, which results in elongated optical traps. The amount of trap elongation increases linearly with optical trapping depth into the water medium and can range from a few microns close to the coverslip, to nearly 100µm at the maximum 130µm trapping depth of an Olympus Plan Apo Lambda 100x microscope objective.

The second effect that reduces trap efficiency is reflection at the medium boundary between the glass coverslip and liquid trapping medium. One type of reflection is total internal reflection (TIR), which occurs when a propagated wave is incident upon a medium boundary with a decreasing refractive index (e.g., glass to water) at an angle larger than a critical angle, θ_c. From Snell's Law, we can solve for the critical angle by setting the transmission angle, θ_t, to 90°, and inputting the indices of refraction for the coverglass ($n_{glass} = 1.52$) and water ($n_{water} = 1.33$):

$$n_{glass} \sin\theta_i = n_{water} \sin\theta_t \tag{16}$$

$$\sin\theta_i = \frac{n_{water}}{n_{glass}} \sin\theta_t$$

$$\theta_c = \arcsin\left(\frac{n_{water}}{n_{glass}}\right) = 61.0°$$

Therefore, light that is focused at angles greater than 61.0° will be lost into the immersion oil due to TIR. This effect is visible in Figure 33, where an oil-immersion objective ($NA = 1.45$) is immersed into oil ($n_{oil} = 1.52$) on top of a glass microscope slide ($n_{glass} = 1.52$). The high-angle rays reflect in the glass, made evident by the bright edges of the microscope slide.

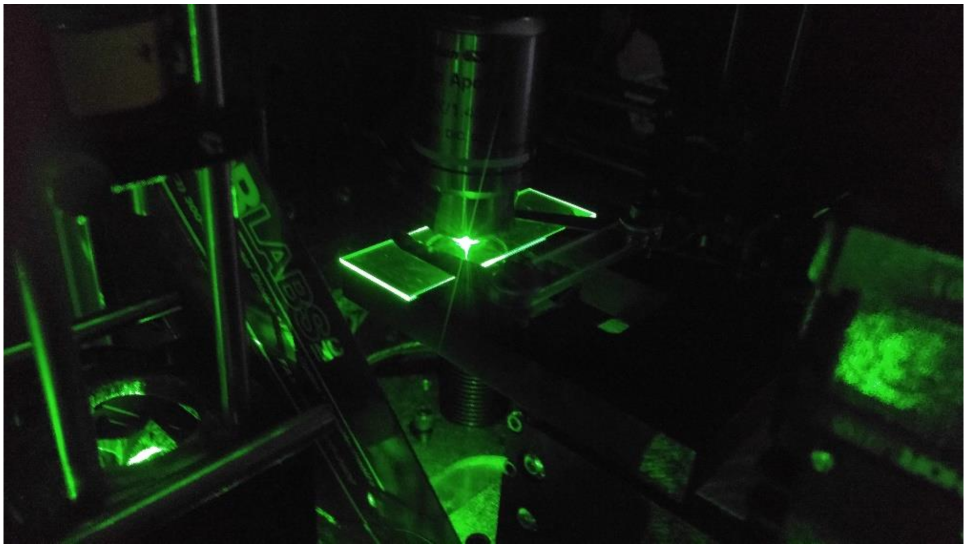

Figure 33: Total internal reflection at a glass-air boundary

Additional losses occur across all focusing angles (i.e., from 0° to $\theta_c = 61°$) due to a second reflective effect known as Fresnel reflection. Fresnel reflection is polarization-dependent, but since the microscope objective focuses in a radial cone, a bulk reflection value can be calculated by averaging the contributions from the s- and p-polarizations:

$$R_s(\theta_t) = \left|\frac{n_{glass}\cos\theta_i - n_{water}\cos\theta_t}{n_{glass}\cos\theta_i + n_{water}\cos\theta_t}\right|^2 \tag{17}$$

$$R_p(\theta_t) = \left|\frac{n_{glass}\cos\theta_t - n_{water}\cos\theta_i}{n_{glass}\cos\theta_t + n_{water}\cos\theta_i}\right|^2$$

$$R(\theta_t) = \frac{R_s(\theta_t) + R_p(\theta_t)}{2}$$

The result is that light focused across all angles (i.e., from 0° to $\theta_c = 61°$) will experience some attenuation due to Fresnel reflection.

Using a MATLAB-based ray-tracing simulation (Appendix D), both aberration and reflective effects become visible (Figure 34). This figure (not to scale) features a cone of light focusing at 71° (for a $NA = 1.45$ oil-immersion lens). The vertical black dashed line represents a glass-to-water medium boundary transition. The black marginal rays depict those lost to TIR (i.e., rays between 61-71°), whereas the blue rays represent the relative amount of attenuation due to angle-dependent Fresnel reflection (ranging from 40% for the most marginal rays to 0.04% for rays centered along the y-axis).

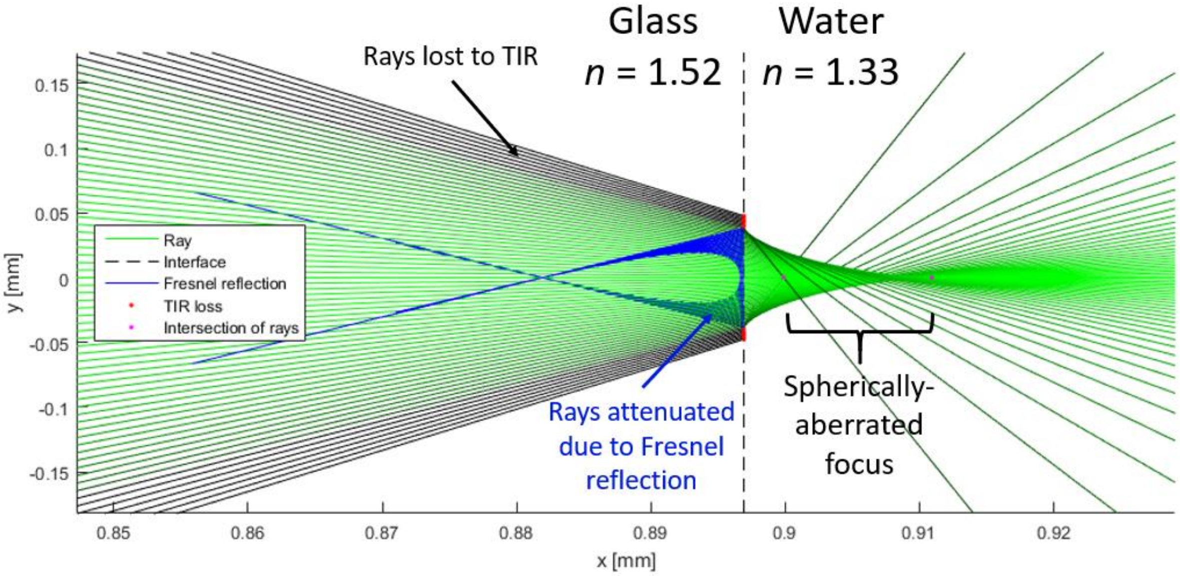

Figure 34: MATLAB ray-tracing simulation of TIR and Fresnel reflective losses

The spherically-aberrated focal region is influenced by the index-of-refraction mismatch between the glass and water media. For the parameters presented above, the amount of focal-region elongation is linearly dependent on trapping depth as:

$$\delta_z \approx 0.69 \cdot d \; [\mu m] \tag{18}$$

For example, the Olympus Plan Apo Lambda 100x oil-immersion microscope objective (*NA* = 1.45) has a total working distance of 0.3mm, or 0.13mm after a no. 1.5 coverslip. Trapping at the full 130µm depth creates a focal region that is approximately 70µm tall. This does not prevent stable radial trapping as there still exists a tight electric field gradient, but axial trapping becomes progressively more difficult, if not impossible, as trapping depth into an index-mismatched media increases.

The use of a high-NA, oil-immersion lens in an aqueous medium will give rise to aberration and reflective effects[159] that currently prohibit the use of standard Mie-regime optical force simulations. Experimental mapping of the full optical profile will provide the most accurate representation of the forces experienced by optically-trapped particles.

Chapter 6

Efficient Joining of Microparticles

The aim of this chapter is to demonstrate a holographically-driven photopolymerization process for joining colloidal particles to create planar microstructures fixed to a substrate, which can be monitored with real-time measurement. This chapter introduces a new photopolymerization process for rapidly joining simultaneously handled microspheres in plane. Additionally, a new process control technique allows for efficient identification of when particles have been successfully joined by measuring a sufficient reduction in the particles' Brownian motion.

6.1 Motivation

The focus of this chapter is to introduce a new and reliable method for simultaneously joining particles to create 2D microstructures. Robust and scalable particle joining is one of the key barriers preventing the implementation of HOT as a viable microfabrication technique. Previous joining efforts have relied on the high affinity between microparticles that are pre-coated with the complementary biomolecules streptavidin and biotin[160]. Relying on surface-coating affinity, however, places practical limits on the variety of particles that can be joined and requires that particles coated with these complementary biomolecules remain separated until joining is desired. Another similar approach has been proposed to increase the variety of complementary surface coatings by leveraging hybridization between DNA oligomers attached to the particles[58]. Unfortunately, this approach would still be burdened by the task of having to keep the particles separated until they are manually joined. A non-chemical alternative for joining particles is photothermal melting[161]. This technique relies on high laser intensities to melt and join the particles together. It is, however, difficult to sufficiently concentrate the delivery of the laser's thermal energy at the bonding interface between the particles to effectively join them, and particles made of different materials with different thermal properties are often not compatible to join using this approach. Cyclic heating of the entire sample chamber to temperatures above the softening point of the particles also allows for joining[162], but this method is time-consuming and cannot be localized. The most promising joining technique utilizes photopolymerization (i.e., the process of transforming a liquid monomer solution into a solid structure via photo-induced cross-linking)[54,78,163,164]. Joining via photopolymerization is unique in that it is not heavily dependent on the properties of the particles being joined and thus can be used to join particles of almost any material by encasing them in a polymer shell.

The dexterity and flexibility of the proposed HOT approach will enable a variety of applications. Holographically-assembled microlattices could be made to serve as photonic crystals or new metamaterials with tailored mechanical properties. Our HOT approach could also be used for adding flexures, anchors, or wires[165] to preformed parts of microelectromechanical systems (MEMS). Additionally, our approach may be used to fabricate structures for cell confinement[166]. Once assembled, these microdevices could subsequently be actuated using optical forces for sorting cells or controlling fluid flow in lab-on-a-chip devices.

This paper's contributions related to holographically-driven photopolymerized particle joining include *(i)* a chemical recipe that supports photopolymerization, *(ii)* a trap-plane intensity pattern used to initiate photopolymerization at the bonding interface between particles, and *(iii)* a real-time process monitoring technique that records Brownian motion to determine when joining is complete.

6.2 Photochemistry

We will now outline an acrylamide-based vinyl photopolymerization reaction used for particle joining. When laser light interacts with a photoinitiator and co-initiator mixture, the chemical system generates free radicals that cause a chain reaction of cross-linking between dissolved acrylamide monomers[167]. The bulk process terminates when the fusing laser intensity is reduced to prevent significant free radical formation. Individual chains then terminate due to recombination or disproportionation reactions that form unreactive chains[168]. The photochemistry reported here is inspired by the bulk-gel synthesis process[169] with concentrations adjusted to enable particle positioning without cross-linking at low laser power and localized photopolymerization at high power.

The aqueous medium consists of 0.68M acrylamide monomer, 17mM bis-acrylamide cross-linker, 17µM safranin dye photoinitiator, and 16mM triethanolamine co-initiator (Sigma-Aldrich). We favor safranin dye (λ_{max}=532nm) as a free radical photoinitiator because its absorption wavelength coincides with our trapping laser and because its absorption maximum is high[170]. Solutions are prepared and tested in a darkened room in order to reduce premature polymerization induced by overhead fluorescent lights. All experiments use unfunctionalized polystyrene microspheres with 4.21-micron diameters (Bangs Laboratories, Inc.). Figure 35 contains example patterns and Figure 36 depicts the construction process.

Oxygen is an inhibitor in a free-radical photopolymerization reaction, which reacts with laser-induced free radicals to form unreactive species[171]. Therefore, it is important to prepare the medium mixture in such a way as to minimize dissolved oxygen levels. We found that avoiding vigorous mixing (i.e. no vortexing of samples) was sufficient to create a chemical environment that was conducive to the assembly of the structures in Figure 35 and Figure 36. Performance may be further improved by enclosing the sample chamber in an environment with controlled oxygen content to eliminate diffusion of atmospheric oxygen[45].

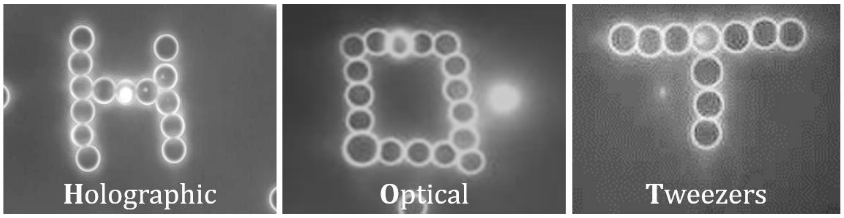

Figure 35: The letters H-O-T joined with acrylamide-based photopolymer

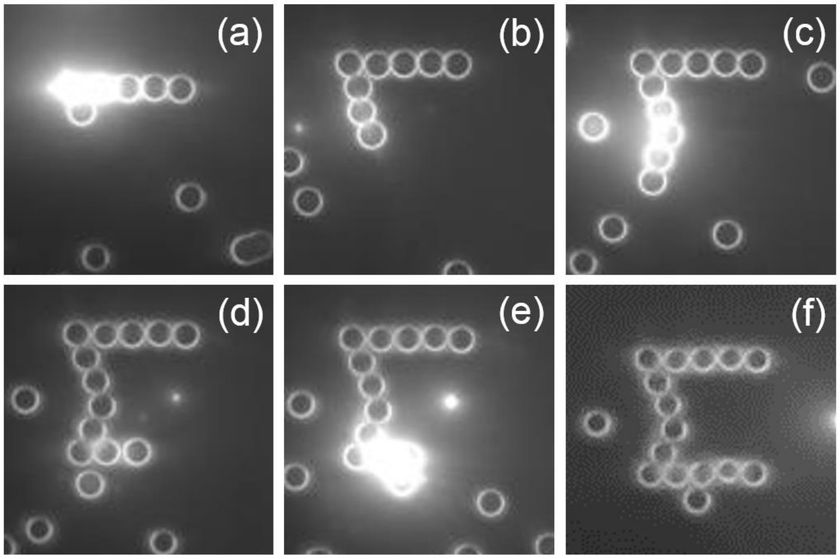

Figure 36: Construction steps for joining a capital sigma arrangement of microspheres

6.3 Experimental System

The holographic optical trapping system consists of a single CW laser and 256-by-256 pixel phase-only spatial light modulator (Boulder Nonlinear Systems HSP0532-256). The microscope objective is slightly under-filled using a 4-f telescope to maximize trap efficiency[172]. SLM positioning accuracy is approximately 200nm but the system's overall positioning accuracy is approximately 0.5µm due to Brownian motion.

The user manually positions particles prior to joining them with individual point traps, which are created in response to mouse clicks within a MATLAB graphical-user interface (GUI). The adaptive-additive Gerchberg-Saxton algorithm[85] calculates all holographic phase patterns. Hologram calculation and SLM updates are performed at rates between 75 and 100 Hz. The computer is a Dell Precision T3600 with a quad-core, 3.0 GHz processor and 12 GB of RAM.

6.4 Holograms for Joining

To rapidly and robustly join adjacent microparticles together on the substrate, laser light can be used to induce a photopolymerization reaction between them. To this end, we delivered power via the distributed trapping pattern shown in Figure 37. The addition of the smaller inter-particle traps allows for the rapid onset of joining since there is more photopolymer between the particles than at the particle-substrate interface. The ratio of the intensity at the particle interfaces to the maximum intensity used to trap (shown in Figure 37 as approximately 0.5) produces joining for values between 0.3 and 1.0, although mid-range values more effectively maintain planar patterns while providing reliable joining.

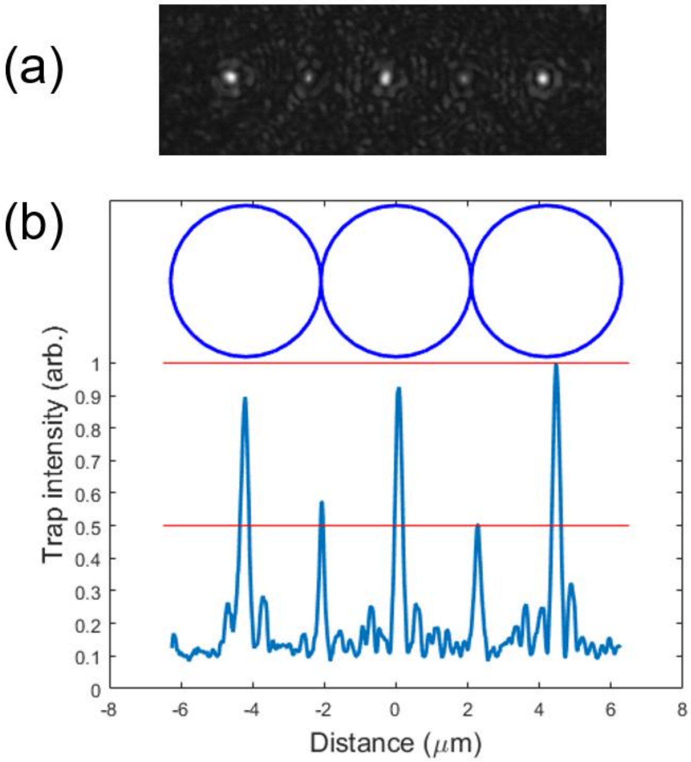

Figure 37: Hologram used to join adjacent microparticles

During operation, microparticle positioning requires 20mW per point trap and immobilization requires 100mW to 150mW line traps (Figure 38) for approximately 2 to 8 seconds depending on slight variations in the aqueous photopolymer chemistry. Trap powers are measured at the trapping plane using an integrating sphere photodiode power sensor (Thorlabs S142C and PM100USB) and the zero-order spot removed. Underpowered trap profiles are slow to initiate photopolymerization or may not initiate the reaction at all. Overpowered trap profiles, on the other hand, can produce uncontrolled, ‘runaway’ reactions where photopolymer engulfs large regions of the trapping plane. Typical particle positioning speeds are 3-4 microns per second. To manually assemble the structure in Figure 38, 1 to 5 beads are trapped and fused at a time. Since the aqueous medium with the dissolved acrylamide is denser than the polystyrene microspheres, the particles float to the top of the sample chamber for easy retrieval.

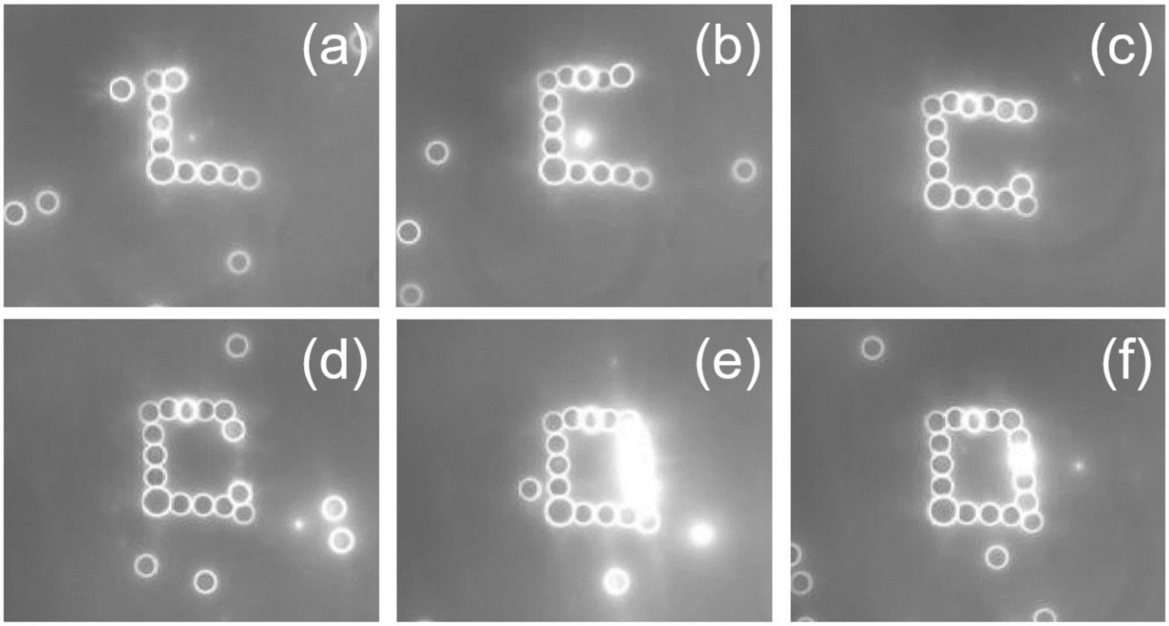

Figure 38: Construction and joining of microspheres into a rectangular array

6.5 Process Control Technique

Most successful manufacturing and fabrication technologies require some degree of process monitoring and control. This section outlines a method for determining when the photopolymerization reaction of the proposed technology has sufficiently joined particles by measuring their Brownian motion. A particle trapped by a high-intensity 100mW to 150mW linear trap pattern exhibits visible shaking due to its increased temperature, but its positional variance decreases as the particle is polymerized to its neighboring particles and the glass cover slip. The photopolymerization process is complete when the magnitude of the Brownian motion of the particle drops off by ~2 orders of magnitude. It is possible for a system operator to make a qualitative assessment of Brownian motion and to then appropriately cut the laser power. For micromanufacturing applications, however, it is preferable to link this effect to a quantitative measurement and automatic power throttling to halt the joining reaction as soon as the particles have been sufficiently joined to maximize efficiency.

In order to automatically determine when the joining reaction is complete, we monitor the Brownian motion of a single particle and cut the laser power once the Brownian motion magnitude drops to a set threshold. We perform this measurement by reducing the camera's field of view to an area containing only the particle of interest and track the centroid by using MATLAB's *imfindcircles* command. An additional dichroic filter placed before the imaging cameras prevents laser light from interfering with the image processing routine. The unit of the centroids position is camera pixels. The variance (in units of pixels^2) is then computed using a moving window consisting of 50 samples. Image acquisition and variance calculations proceed at approximately 60Hz. Figure 39 shows examples of the measured positional variance of the center particle in a 3-by-1 linear array during a high-intensity joining process like the one shown in Figure 38. The reaction is complete when the position variance drops below the horizontal threshold line. The variation in joining time is a result of variations in the chemistry of the medium, including the presence of dissolved oxygen inhibitors.

The threshold position variance for reliable particle joining should be calibrated for each sample. This threshold value is dependent on constant measurement system parameters (e.g., camera pixel size, camera magnification, and trap efficiency) and variations in aqueous medium chemistry between samples. In our experiments, calibrated threshold position variance values range from 0.1pixels^2 to 2.0pixels^2. The threshold value used in the fabrication of the structures in Figures 1 and 2 is 0.5pixels^2. Position variance values reach an absolute minimum between 0.1pixels^2 and 0.01pixels^2, but the laser power should be reduced before the absolute minimum to prevent excessive accumulation of photopolymer.

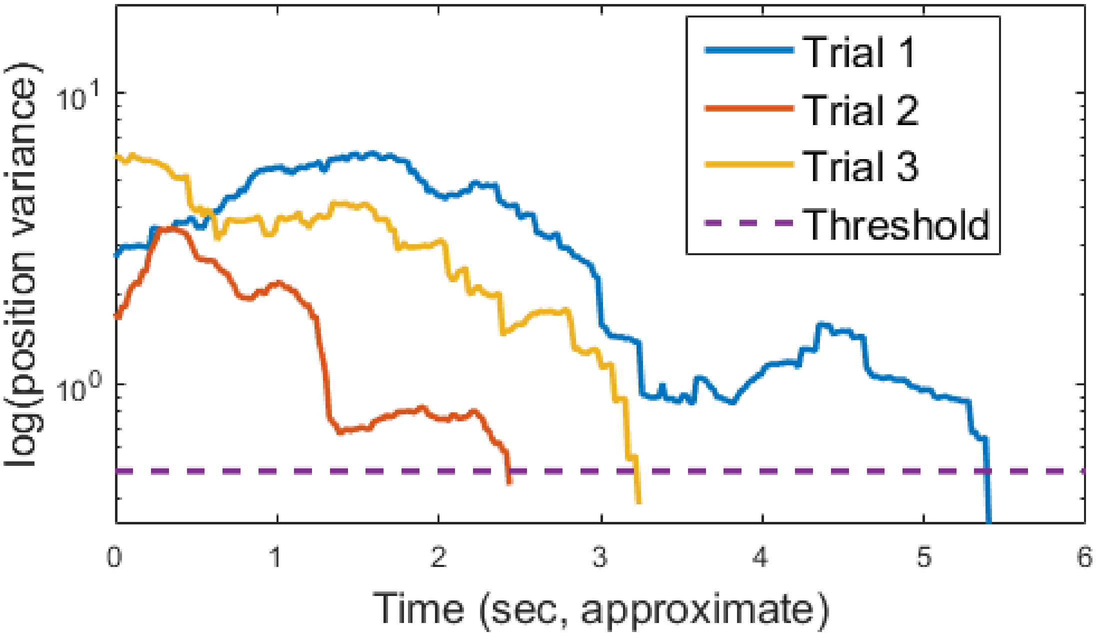

Figure 39: Microsphere positional variance during joining

Calibration of the threshold position variance value is performed by joining approximately 4 to 8 separate particles to the cover slip until different threshold values are reached. The system operator’s objective is to find threshold position variance values that correspond to immobilized particles. Once a lower bound for position variance that is indicative of an immobilized particle is determined, the system control software can automatically reduce the laser power and end the photopolymerization reaction. In addition, correct tuning of the positional variance threshold and focusing of the joining hologram can result in particles that are adhered to one another but not to the substrate. The following example (Figure 40) demonstrates how a 1x3 array of 6µm-diameter microspheres can be joined and manipulated as a single object using a trap on the leading sphere.

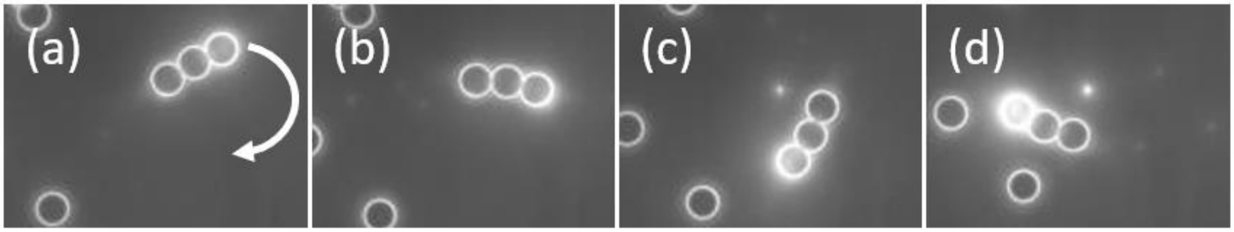

Figure 40: A 1x3 array of 6µm-diameter particles is joined and manipulated

6.6 Outlook

Future research will maximize the number of particles that can be joined within a large microstructure by reducing undesired solidification of the medium caused by unwanted stray light. Sources of stray light include the SLM's zero-order spot, background speckle in the holographic patterns, and the fact that the same laser wavelength is currently used to trap and join the particles. Furthermore, the slow dynamics of the CW laser's closed-loop current controller result in slow power reduction of high-intensity trap patterns while the photopolymerization reaction is still occurring. To address these issues, future work will reduce the SLM's background speckle via higher-resolution holograms and incorporate a beam shutter to rapidly turn the joining laser on or off. Furthermore, it is possible to decouple the handling and joining processes by delegating particle handling to a second laser wavelength that is not able to initiate the reaction, such as a two-photon system[56]. Future research will investigate inexpensive LED-based one-photon spot curing in the near-UV range as an alternative to an ultrafast laser.

Future research will also enable HOT techniques to fabricate complex microstructures in three dimensions via photopolymerization. Producing freely-floating structures with our current approach is difficult since the chosen chemistry causes the particles to float against the cover slip. By selecting microparticles that achieve near-neutral buoyancy in the aqueous photopolymer medium, however, 3D microstructures can be assembled throughout the entire depth of the sample chamber. These structures can either be assembled while fixed to a substrate or while free-floating in the medium.

A method for joining microparticles via photopolymerization was introduced as a means of fabricating planar microstructures fixed to a substrate. Particles were simultaneously positioned within an aqueous photopolymer medium using a custom-developed holographic optical tweezers system and a specialized trap-plane intensity pattern was used to drive the joining process. The reaction's progress was measured by observing Brownian motion and the laser power was reduced upon reaching a pre-calibrated threshold value. Example 2D microstructures were assembled using multiple simultaneously-handled particles as case studies.

Chapter 7

Novel Applications of Two-Photon Lithography

This chapter departs from exclusive discussion of the HOT approach to introduce two-photon lithography (TPL) and its use in a novel hybrid TPL-HOT system. For the past half-century, lithographic approaches have served as the primary approach for direct additive microfabrication[173] of structures that do not require assembly. Typical lithography systems, including both laser-scanning[174] and projection[45] approaches, rely on layer-by-layer assembly via stacking of 2D patterns. Alternative approaches for 3D laser scanning[80] or 3D volumetric curing[175] have been demonstrated, although these techniques have not yet found wide adoption due to limited speed or constraints on the geometries that can be fabricated. The majority of materials used in lithography are acrylic polymers[176–178], although recent literature has demonstrated advances in lithographic fabrication using ceramics[179] and conductive polymers[180]. The highest-resolution systems utilize a two-photon polymerization reaction, which is a nonlinear absorption process that occurs only in very small regions of high photon density. More information about this photochemical process is described in the next section.

The combination of TPL-based fabrication and HOT-based manipulation has already shown great promise in assembling microscale mechanical components including micron-scale screws[62], snap-fits[63], microgranular lattices[56], and weaves and threaded microfibers[56,181]. However, the work presented in this thesis represents the first time that a hybrid TPL/HOT system has been used to fabricate and manipulate under the same microscope.

The first section of this chapter presents the basic working principles of TPL as well as the experimental system and software features that enable TPL-based fabrication of novel microstructures and colloidal microparticles. In the second section, case studies in direct TPL fabrication of mechanical metamaterials are presented and include a negative Poisson’s ratio structure, large-deformation rolling contact materials, and a constant-stiffness spring topology. The third section introduces how TPL can be combined with a continuously-flowing microfluidic channel to enable conveyor-belt-like fabrication of arbitrarily-shaped microfluidic particles. Finally, the chapter concludes with preliminary work on hybrid TPL/HOT-based fabrication and manipulation.

7.1 System Design

7.1.1 Photochemistry

The general photopolymerization reaction, in which monomers cross-link to form solid polymer networks, is initiated by the absorption of photons by photoinitiator molecules. In the common one-photon absorption process used in many types of photolithography[129,182], a single high-energy photon (typically in the 300-400nm ultraviolet portion of the spectrum) is absorbed by a photoinitiator molecule (Figure 41), which cleaves into free radicals that initiate a chain reaction of polymerization among dissolved monomer molecules. The result is a large ‘initiated area’, as photoinitiator molecules encounter initiating photons across the full writing beam.

In contrast, the TPL approach uses a nonlinear two-photon absorption process, in which two lower-energy photons (typically in the 600-800nm near-infrared (NIR) or infrared (IR) portion of the spectrum) effectively add to provide the same initiation energy (Figure 41). The two NIR/IR photons must influence the same photoinitiator molecule within the molecule's relaxation time, which is on the order of femtoseconds. Thus, a highly-energetic femtosecond pulsed laser is required to achieve the high spatial and temporal compression of photons needed to overcome the activation threshold. The result is a highly-localized initiated area that exists only at the beam's focal point.

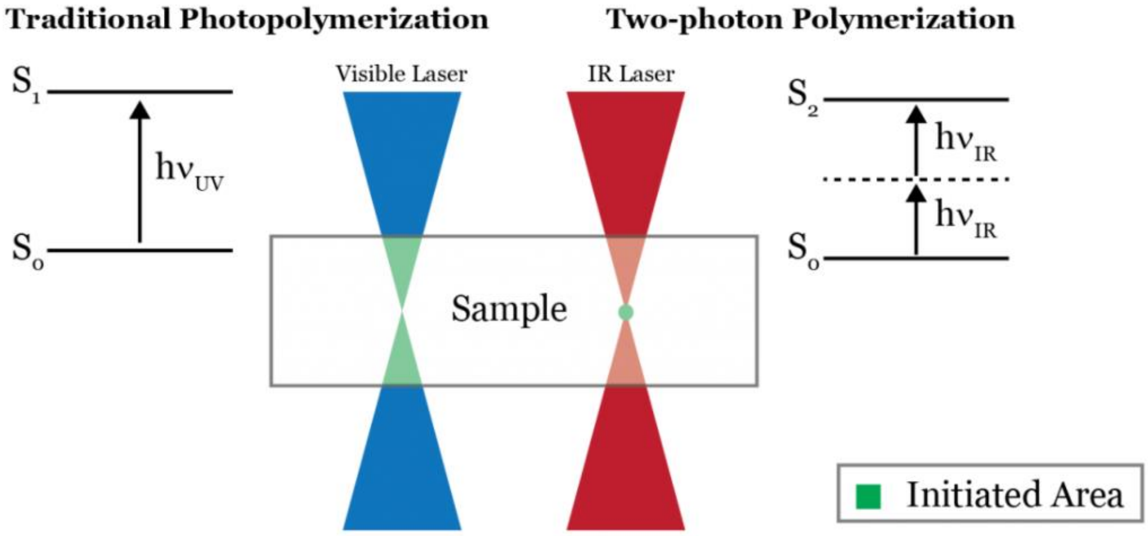

Figure 41: One- vs. two-photon absorption diagrams (image courtesy of the Tucker Stem Cell Laboratory[183])

A practical comparison between one- and two-photon initiation is shown in the fluorescence experiments in Figure 42, where the left-hand near-UV beam creates an initiated area across the full beam, whereas the righthand NIR beam initiates only a very small region at the beam's focal region.

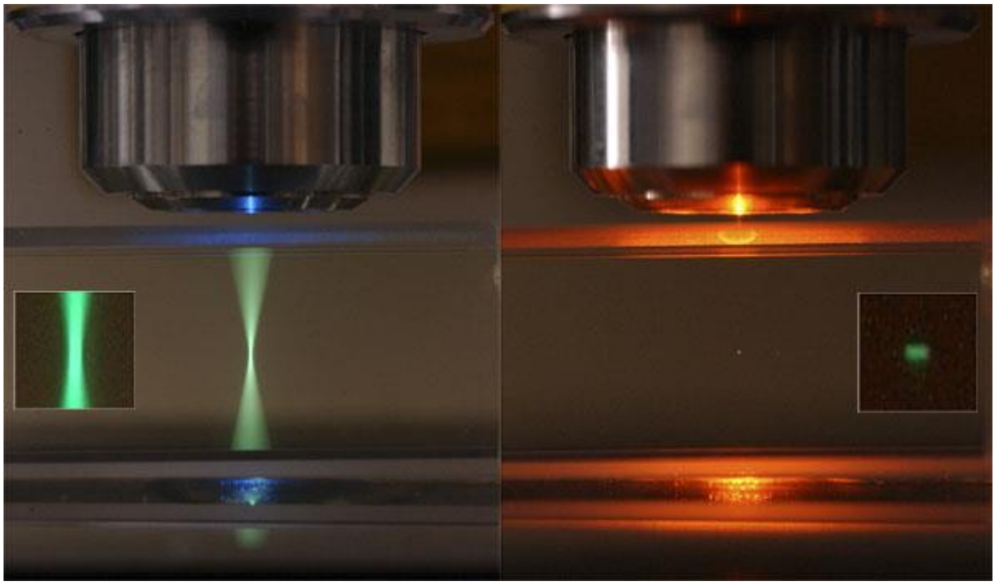

Figure 42: One- vs. two-photon fluorescence in liquid (image courtesy S. Ruzin[184])

In selecting a resin for direct TPL-based printing of microstructures, we sought a multi-functional acrylate for its high degree of crosslinking (resulting in high strength) and high viscosity (so fabricated parts would not shift during substrate height changes). In contrast, resins for fabricating parts for HOT manipulation needed to exhibit lower viscosity values (as less optical trapping force was available because of the lower index of refraction difference between the cured object and the uncured medium). A detailed description of the resins used to fabricate the microstructures and micromechanisms in this work are presented in the respective case study sections (7.2.1 and 7.2.2).

7.1.2 Physical Optics

The hybrid microfabrication system of Figure 43 combines TPL with the HOT system described in Chapter 2. The TPL system includes a femtosecond laser (fs laser, Spectra-Physics

MaiTai eHP DS, 690-1040nm) and an acousto-optic modulator switch (AOM, IntraAction ATM-802DA2 and ME-820-6). The AOM and 2D scanning mirror galvanometer (galvo, Thorlabs GVS012) are driven by an analog output module (National Instruments NI-9263).

Additional components include two ultrafast mirrors (M), beam block (BB), beam expander system (BE, *f* = 50 and 200mm lenses), 2D scanning mirror galvanometer (galvo, Thorlabs GVS012), 4-F telescope relay (two *f* = 60mm lenses), power sensor (Thorlabs S142C and PM100USB), and longpass dichroic mirror (DM2, λ_c = 650 nm).

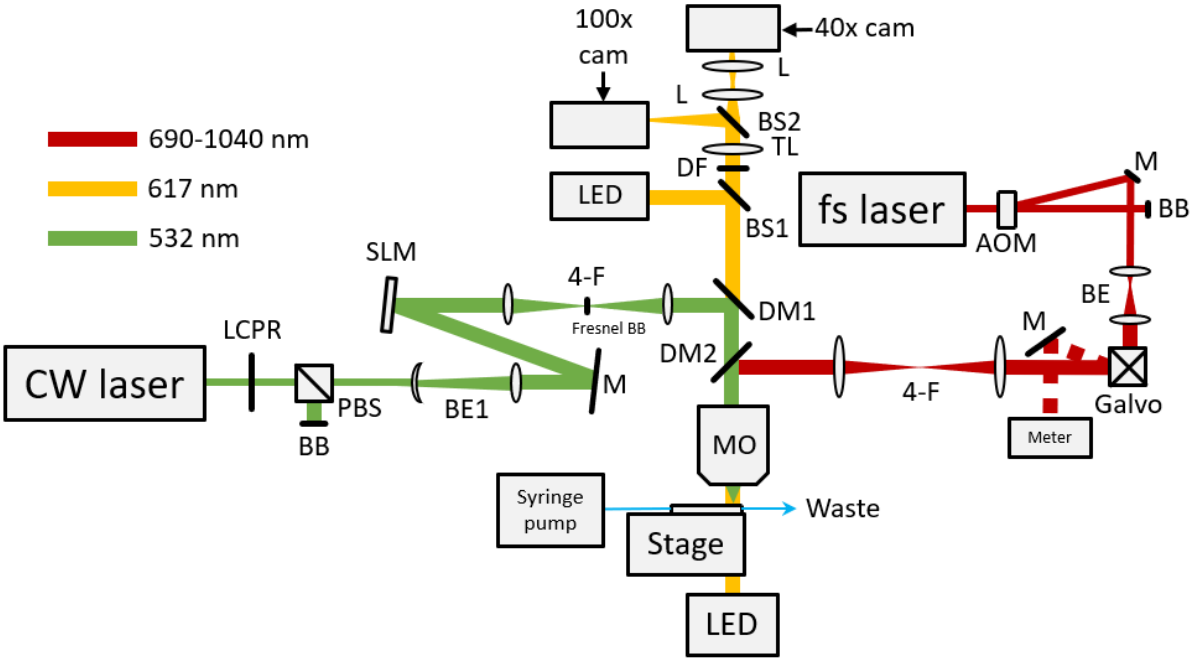

Figure 43: Hybrid HOT-TPL system

7.1.2 Software Design

Preparing a computer-aided design (CAD) file for laser-direct writing involves a path planning step in which the shape must be discretized into a series of points for the laser to scan in sequence. The structures in this thesis were path-planned with Slic3r[185] software, an open-source toolpath planning program that is typically used for conventional fused-deposition modeling (FDM) 3D printers. Slic3r software has input fields for a standard STL file, the size of the writing voxel, and the type of fill pattern (e.g., raster- or spiral-based fills). Slic3r's output is G-code provided at various layers ("slices") across the object. Custom MATLAB code is used to convert the G-code commands to uniformly-spaced coordinates and to output a MATLAB-formatted *.mat* file.

Data sets produced by either method often produce 10^4-10^7 points, so custom MATLAB code was produced to quickly handle, manipulate, and visualize coordinates across many layers.

Table **7** provides a list of sub-functions created to load, manipulate, and verify large sets of spatial data prior to laser scanning. The MATLAB code used in the TPL system is available upon reasonable request.

Table 7: List of *Scan* class commands for manipulating printing data

Category	Function name	Description	Argument(s)
Input/output	*LoadScanData*	Load a G-code file (exported from Slic3r[185] or similar software)	Filename
	LoadImage	Load an image file for 2D writing (.jpg, .bmp, .png, or similar)	Filename
Data manipulation	*Center*	Place the object at the coordinate origin	
	ZeroZ	Translate the object so that its z-coordinates are z = 0 and larger	
	Translate	Translate the object by specified distances	δ_x, δ_y, δ_z
	Rotate	Rotate the object by specified angles	θ_x, θ_y, θ_z
	Scale	Scale the object along each axis	C_x, C_y, C_z
	Tessellate	Duplicate the object with specified spacing	N_x, N_y, N_z δ_x, δ_y, δ_z
	Mirror	Mirror the object along each axis	M_x, M_y, M_z
	Upsample	Upsample the scan data by adding additional points	N_{factor}
	Downsample	Downsample the scan data by removing points	N_{factor}
Data verification	*GetCentroid*	Return the current centroid of the object (calculated as mean of total extents)	
	GetExtents	Return the extents of the object along each axis	
	NumLayers	Return the number of print layers in the object (along the z-axis)	
	CalcFabTime	Estimate the total time to fabricate the object	
	ScanRate	Return the linear velocities of the laser spot during the fabrication process	
Data visualization	*Plot3D*	Plot the object in 3D	
	Animate3D	Animate the fabrication of the object in 3D	

The data is then processed into four channels as columns in an *n*-by-4 matrix: *(1)* the x-coordinates of each point in the scan path (in units of voltage to be written to the scanning galvanometer), *(2)* the y-coordinates of each point in the scan path (also in units of voltage), *(3)* the AOM's analog drive voltage (which corresponds to the relative amount of pulsed-laser power at each scan point), and *(4)* the Z-axis piezo positioner's drive voltage (which corresponds to the Z-height of the sample). This data set is uploaded to the DAC card that drives the galvanometer, AOM, and piezo controller. The DAC card can drive scans at rates up to 40kHz, although the scanning galvanometer's practical bandwidth limitation for most scans is between 5-10kHz depending on the extents of the scanned area.

7.2 Case Studies in Microscale Mechanisms

This section presents two microscale mechanisms directly fabricated with the TPL approach: *(1)* a mechanical metamaterial designed to achieve a negative Poisson's ratio and *(2)* a 2D lattice of rolling contact mechanisms designed to achieve low rolling friction.

7.2.1 Negative Poisson Metamaterial

Poisson's ratio is a value that describes the ratio of axial to transverse strain[5]. Virtually every natural material possesses positive Poisson's ratios (i.e., they swell in a transverse direction when compressed axially). The metamaterial design featured in Figure 44 was generated with the FACT design methodology[1] and has been optimized[186] to achieve a Poission's ratio of -0.9. Materials exhibiting negative Poisson's ratios, also known as auxetic materials, are expected to find application in variable permeability membranes[187,188], fasteners[189,190], and acoustic dampers[191,192].

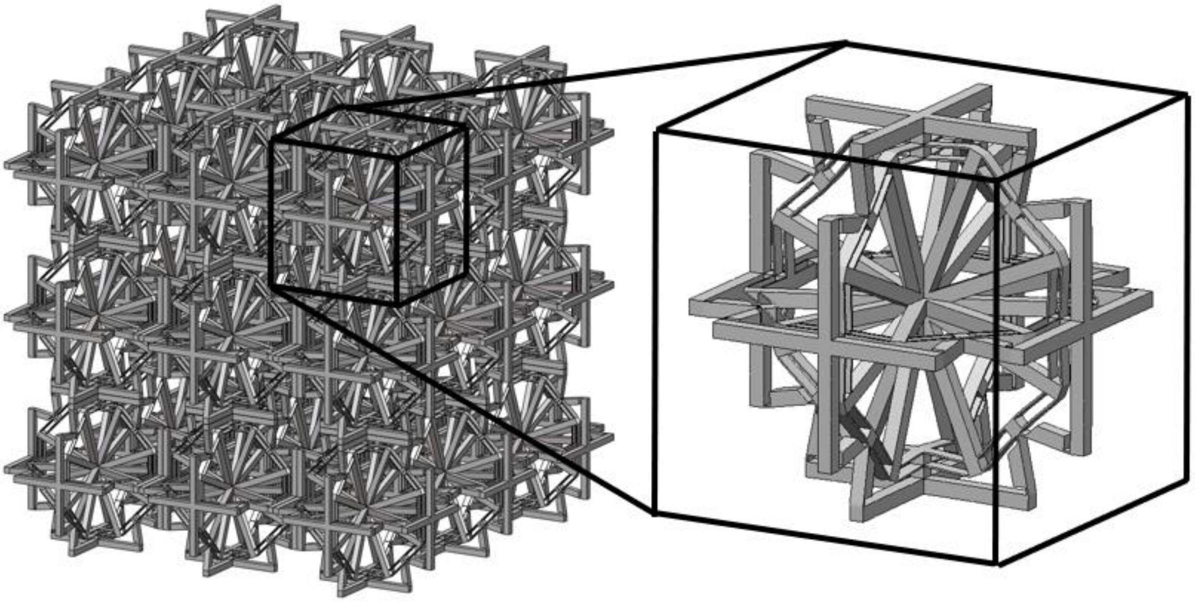

Figure 44: Negative Poisson's ratio metamaterial design

The negative Poisson lattices shown in Figure 45 was fabricated from proprietary Nanoscribe IP-DIP photoresist obtained through a collaborator. The writing spot used approximately 10mW of power at 780nm and writing speeds on the order of 100µm/sec. The total fabrication time for the lattice was approximately 1 hour. The resulting lattice had features with 300nm features in the writing laser's focal plane and 800nm features along the axis of the writing beam.

After the lattice was printed, the glass slide containing the sample was removed from the TPL system and developed in propylene glycol monomethyl ether acetate (PGMEA) for 15 minutes and 99% isopropyl alcohol (IPA) for 15 minutes. The glass slide was then scribed to fit on a scanning electron microscope (SEM) stub and was mounted with double-sided tape and conductive silver paste. The samples were coated with approximately 1nm of iridium via 10 minutes of sputter coating and imaged in an FEI Nova 600 SEM. Future research efforts will use in-SEM nanoindentation machines to examine the bulk mechanical properties of microstructured lattices[193].

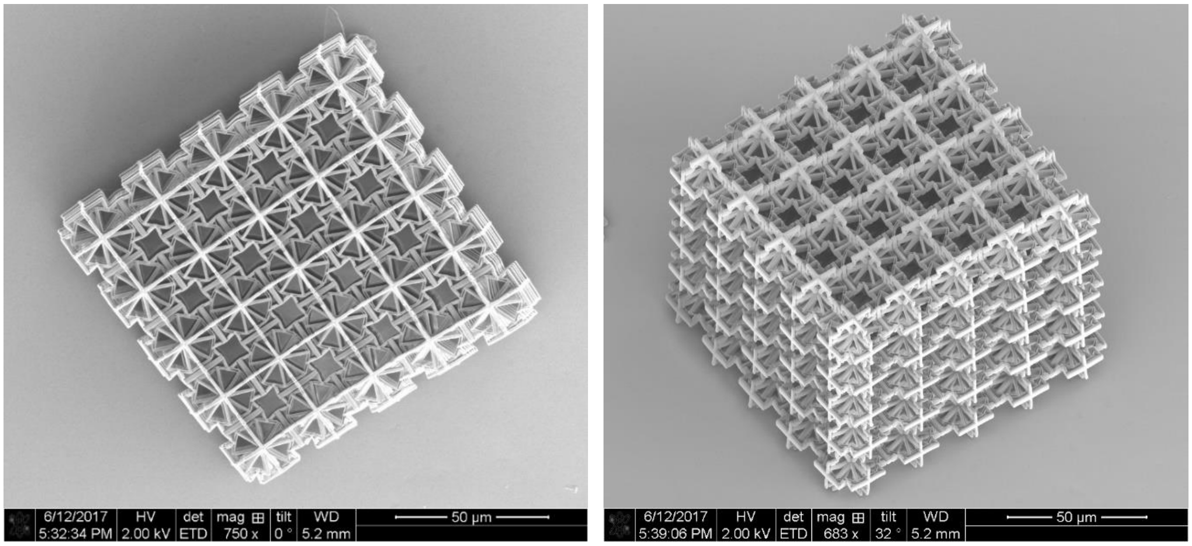

Figure 45: SEM images of a 5x5x5 lattice of a negative Poisson's ratio metamaterial

7.2.2 Rolling Contact Mechanisms

This section demonstrates the direct-TPL fabrication of compliant rolling-contact architecture materials (CRAMs, Figure 46) that utilize compliant rolling contact joints (CRJs)[194,195] to achieve large-range and low-friction rolling motions. CRAMs possess the unique properties of achieving nearly 360 degrees of continuous rotation, minimal friction because of rolling contact between joints (as a no-slip condition is enforced), and high stiffness and load capacity in all other directions.

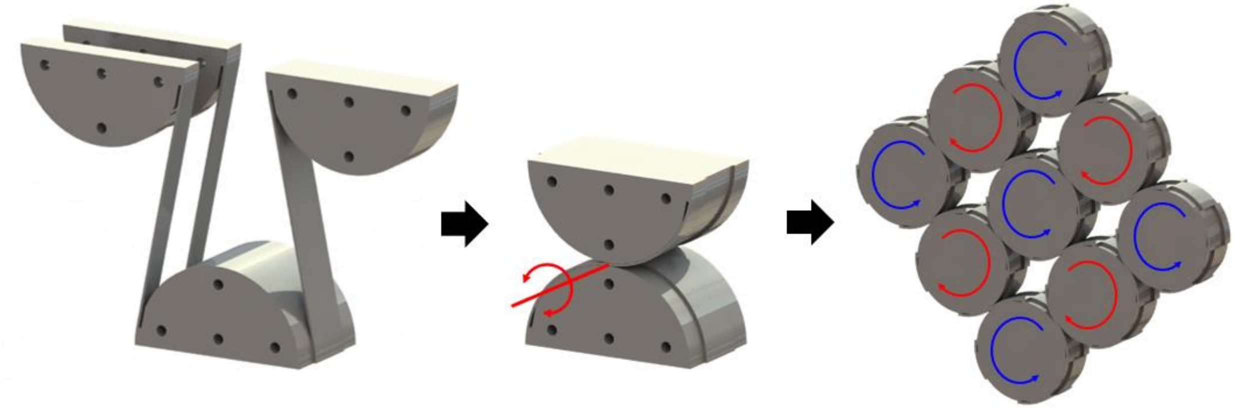

Figure 46: Compliant rolling-contact architecture metamaterial (CRAM)

The CRAMs shown in Figure 47 and Figure 48 were fabricated from proprietary Nanoscribe IP-DIP photoresist obtained through a collaborator. The writing spot used approximately 15mW of power at 780nm and writing speeds on the order of 250µm/sec. The total fabrication time for the lattice was approximately 3 minutes.

The scan paths for the CRAMs of Figure 46 were calculated by slicing a single CRJ (using Slic3r open-source software[185]) and tessellating it by copying and translating its coordinates (using MATLAB). Subsequent shrinkage of the photopolymer caused the flexure straps to shift and sever, creating gaps between each individual CRJ.

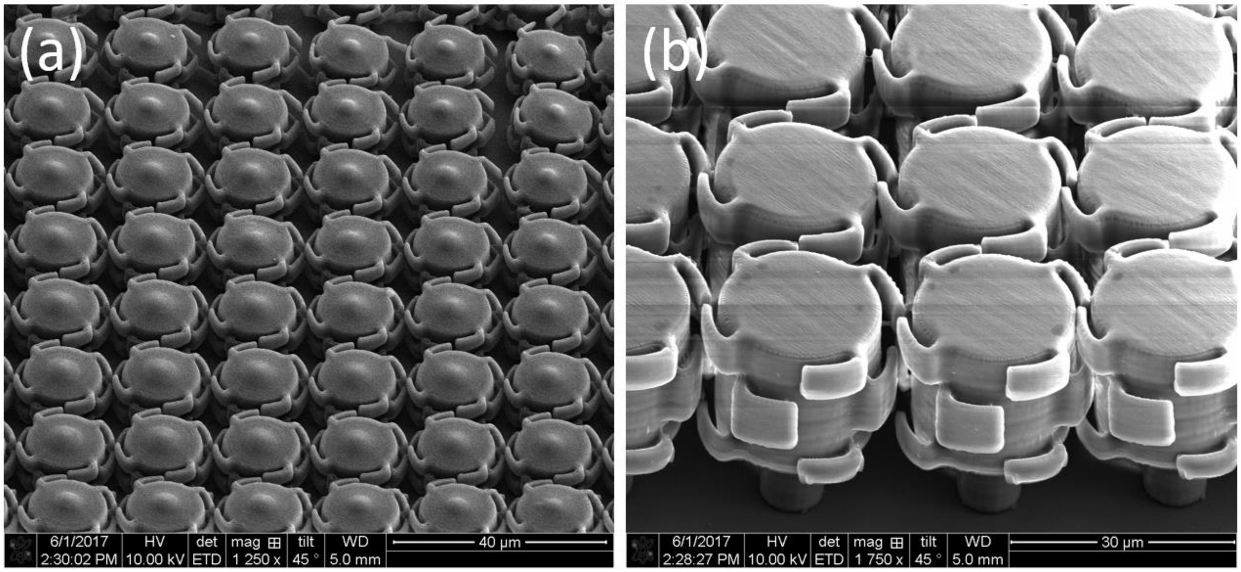

Figure 47: Defective individual rolling contact mechanisms fabricated with TPL

In contrast, the CRAM array shown in Figure 48 was processed as a full mechanism and the improved scan path produced continuous flexure straps with no discontinuities.

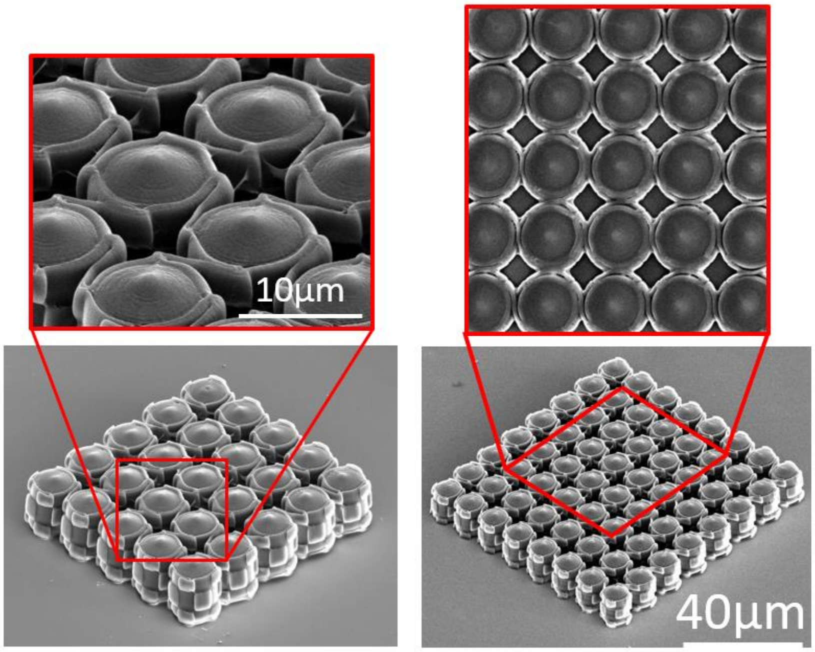

Figure 48: Corrected rolling contact mechanisms fabricated with TPL

7.3 Case Studies in Hybrid TPL/HOT

This section presents two microscale mechanisms printed with the TPL approach and subsequently handled with the HOT approach: *(1)* a mechanical metamaterial designed to achieve a negative Poisson’s ratio and *(2)* a 2D lattice of rolling contact mechanisms designed to achieve low rolling friction.

The photopolymer resin used to fabricate the mechanisms in this section consisted of 1wt.% Li-TPO (Colorado Photopolymer Solutions), 35wt.% ethoxylated (15) trimethylolpropane triacrylate (Sartomer SR9035), and 64wt.% DI water. This photopolymer is specifically designed for the hybrid TPL/HOT fabrication method as the low viscosity and the difference in refractive index of the cured and uncured polymer enable HOT-based manipulation. All photos are images obtained via optical microscopy.

7.3.1 Negative Poisson Mechanism

A classic version of an auxetic lattice that is particularly amenable to TPL-based fabrication relies on the ‘bowtie’-like thin features shown in Figure 49. As an initial proof-of-concept, a single unit cell was fabricated with spherical ‘handles’ (i.e., the black circles shown in the boxed inset). These handles resemble the microspheres used in the HOT experiments presented earlier in this thesis and were chosen as they effectively transfer momentum from the trapping laser beam into trapping force on the microstructure.

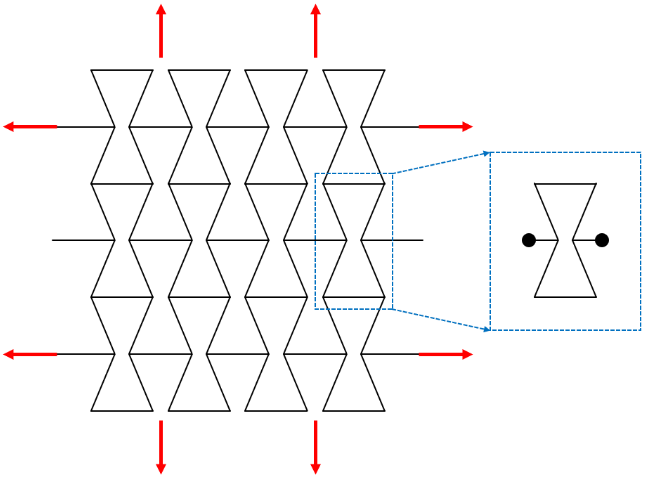

Figure 49: Traditional auxetic lattice and single unit cell design

The single auxetic mechanism (Figure 50) was fabricated in approximately 5 seconds and subsequently deformed with one optical trap placed at each of the spherical polymer ‘handles’. Frames *(a)*-*(f)* were captured over approximately two minutes. The mechanism is shown at its full extension in frame *(d)* the optical traps are switched off. The mechanism is shown to relax during frames *(e)* and *(f)*, demonstrating the polymer’s ability to store strain energy.

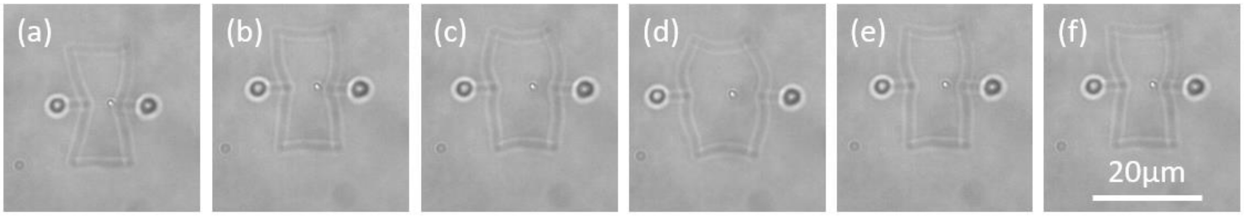

Figure 50: Negative-Poisson mechanism fabricated with TPL and actuated with HOT (images courtesy S. Chizari)

7.3.2 Rolling Contact Mechanisms

For the rolling contact mechanism to operate in its intended low-friction behavior, the flexure straps must be printed and subsequently 'wrapped' to store strain energy. This section leverages the hybrid capabilities of the presented TPL-HOT system to fabricate and manipulate under the same microscope. Figure 51 and Figure 52 show the TPL-HOT system's ability to print and manipulate a single CRJ and two-by-two CRAM lattice respectively. The layers were observed to successfully store strain energy because they would unwrap when the optical traps were switched off.

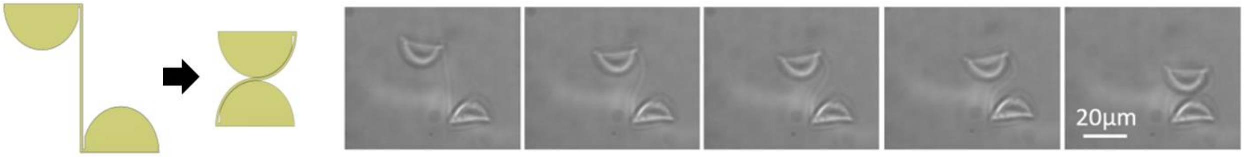

Figure 51: Single rolling contact joint layer fabricated with TPL and deformed with HOT (images courtesy S. Chizari)

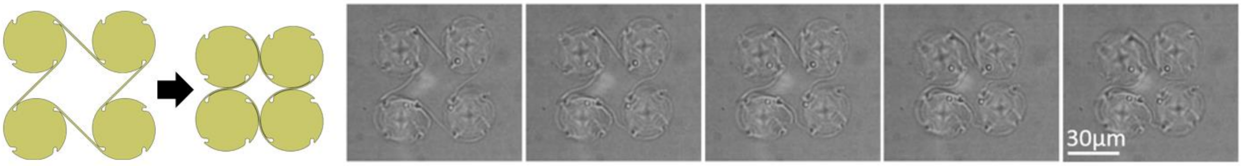

Figure 52: 2x2 CRAM lattice layer fabricated with TPL and deformed with HOT (images courtesy S. Chizari)

7.4 Scanning Two-Photon Continuous Flow Lithography

The demand for custom-shaped colloidal microparticles ranges across a breadth of applications including advanced films and coatings[196], cell scaffolding[197], drug delivery[198], diagnostics[199], and optical devices[200]. Many properties of a bulk colloidal suspension including diffusivity and rheology are strongly influenced by the shape of the constituent particles[201,202]. Additionally, tuning the colloid chemistry can produce a variety of particle properties, including hydrogels that can be made to swell in response to external stimuli for sensing applications[203]. Once fabricated, particles can be assembled using approaches such as holographic optical tweezers[166,204] or self-assembly[205].

There are many established and high-throughput methods for fabricating spherical microparticles. Suspension polymerization[206], emulsion polymerization[207], or droplet-based polymerization techniques[208] each offer control of the sphere's diameter but do not always produce truly monodispersed colloidal suspensions and cannot be readily adapted to produce general non-spherical shapes.

Many surface-patterning approaches, such as casting[209], lithography[210], and the PRINT method developed by DeSimone and colleagues[211,212], can produce upwards of billions of individual particles in a single patterning step, but their geometries are limited to 2D extrusions and must be patterned on a surface. To create freely-floating colloidal objects, Doyle's group first proposed the stop-flow lithography (SFL) approach, in which UV-curable photopolymer is delivered to a projection lithography system via a polydimethylsiloxane (PDMS) microfluidic channel and 2D particles are fabricated while suspended[129]. The SFL approach was limited in throughput by the need to stop the flow of liquid pre-polymer in the channel prior to each curing step. Further improvement in throughput was demonstrated with the invention of continuous-flow lithography (CFL), where lithographic curing occurs while the liquid pre-polymer flows without stopping[213,214]. However, most flow-lithography approaches are limited in resolution, particle shape (i.e., they can only be extruded 2D shapes), and require an oxygen inhibition layer (limiting the use of pre-polymers that would swell PDMS).

In recent years, new approaches have been demonstrated to introduce a third dimension of geometric control. Inertial flow shaping[130] provides a means of creating 3D particles, but particle geometry is limited because axial features must be created by complex microfluidic flow profiles. Pisignano and coworkers applied a highly-localized two-photon lithography (TPL) process to a CFL system (i.e., two-photon continuous-flow lithography, or TP-CFL)[128], which generated 3D colloidal microsprings with very high 3D resolution. However, 3D positioning of the writing spot with respect to the photopolymer medium was performed entirely via piezo-based positioning of the microfluidic chip, limiting the complexity of the fabricated features and the rate at which the laser can be repositioned.

The purpose of this section is to increase the complexity of fabricated particle geometries and dramatically raise the throughput of the TP-CFL approach to produce large numbers of fully-arbitrary 3D shapes with submicron-sized features. To accomplish this, we introduce (1) a new system that allows for 3D scanning-TPL in a microchannel, and (2) a technique for modifying the laser's scan path to compensate for the high-flow-rate liquid precursor. We demonstrate fabrication rates of over 30 particles per second or 10^5 particles per hour. Although this fabrication rate is limited when compared to optimized CFL (i.e., nearly 1000 particles per second which is over 10^6 particles per hour[215]) and a commercial PRINT approach (i.e., 1.2 grams per hour for sub-200nm particles or 30 grams per hour for 5µm particles[216]), the scanning TP-CFL approach is unmatched in its potential to create complex 3D microparticles with arbitrary shapes at submicron resolution.

Also, as we discuss below, the throughput of the proposed approach also shows promise for producing comparable or superior throughputs given additional research.

7.4.1 Experimental Setup

The introduction of a fast laser-scanning component (e.g., an acousto-optic modulator (AOM) or scanning mirror galvanometer) vastly increases the flexibility and speed of TP-CFL when compared to fixed-focal-point systems[128]. Galvanometers can rapidly scan arbitrary in-plane paths with linear writing rates surpassing 1mm/sec[217]. Scanning only in the microscope objective's focal plane produces intricate 2D colloidal objects, but by changing the height of the microfluidic chip by piezoelectric actuation, the medium can be quickly repositioned to write on different layers and produce 3D parts[218]. Other means to rapidly change the writing plane include adaptive-optical components like spatial light modulators (SLMs)[80], however, a discussion of these methods is outside the scope of this paper.

The experimental setup (Figure 53) includes a tunable femtosecond laser (Spectra-Physics MaiTai eHP DS) at 760nm and an AOM (IntraAction ATM-802DA2), which serves as a variable power attenuator and rapid beam shutter. The 2D mirror galvanometers (Thorlabs GVS012) scan the beam within the microchannel and can also temporarily divert it into a power sensor to measure writing power (Thorlabs S142C and PM100USB). The microscope objective is a 100x oil-immersion objective (Olympus Plan Apo Lambda, NA = 1.45). A ±15μm-range Z-axis piezo actuator allows for the height of the microfluidic chip to be changed during laser scanning. The scanning mirror galvanometers, AOM, and piezo controller (Thorlabs TPZ001) are synchronously driven by a four-channel analog output module (National Instruments NI-9263). The imaging system consists of a camera (Thorlabs DCC1545M) and custom tube lens at 40x magnification. Additional components (Figure 53) include: M: mirror; BB: beam block; BE: beam expander; Meter: power meter; 4-F: 4-F telescope relay; DM: dichroic mirror; TL: tube lens.

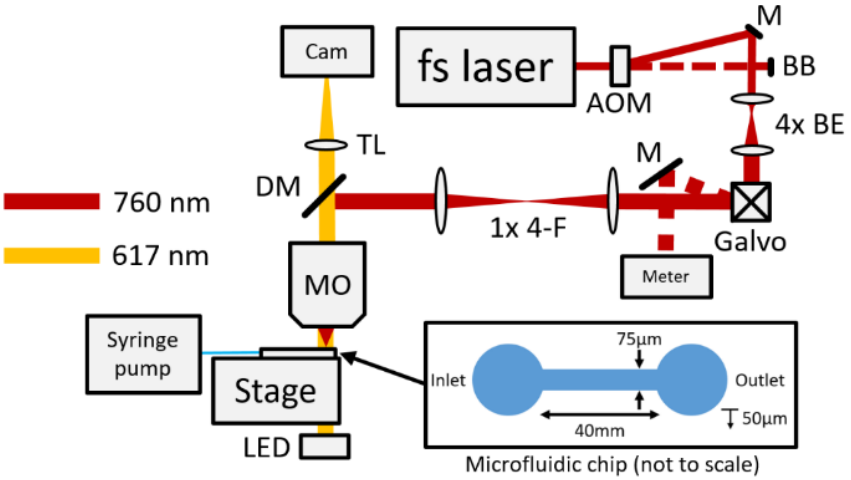

Figure 53: The experimental setup for scanning TP-CFL

The pre-polymer liquid medium consists of Sartomer SR9035 acrylate (65% w/w), DI water (34% w/w), and photoinitiator Irgacure Li-TPO (1% w/w)[205]. Flow is driven by a standard syringe pump (Chemyx Fusion 100).

The microfluidic channel used was cast in polydimethylsiloxane (PDMS) using a standard lithographically-produced mold. The PDMS was bonded to a coverslip ceiling after both surfaces were treated with oxygen plasma. These microfluidic channels were 40mm in length, 75µm in width, denoted as *w*, and 50µm in depth, *h*. The experimental system presented here is compatible with a variety of other microfluidic devices.

7.4.2 Writing Scheme

In this section, we discuss how the laser's scan path must be modified to produce non-warped parts in a rapidly flowing microchannel. The laminar flow within the microchannel acts analogously to a conveyor belt in macroscale manufacturing for delivering uncured liquid pre-polymer to the writing volume (i.e., the scanning laser's focal spot) and for carrying away fabricated colloidal particles. Increasing the flow rate of the channel can allow the laser galvanometer to scan at its maximum bandwidth and produce colloidal objects with higher throughput.

If a laser scan path designed to write in a static medium (Figure 54a) is used in a flowing medium, the part shifts downstream during its fabrication and additional polymer will be cured due to the relative velocity between the scanning-laser's frame of reference and the flowing medium (Figure 54b/e). To compensate for the flow in the microchannel, we continuously shift the laser spot downstream to track the moving part during its fabrication.

Although in pressure-driven laminar flows the velocity profile is generally parabolic for a Newtonian fluid (Poiseuille flow), we have found that a uniform-velocity-profile assumption produces satisfactory results under the fabrication conditions we have used and for particles that occupy a small fraction of the flow cross-section. It is only important to compensate each particle for the average flow speed of its local streamlines. While the velocity profile gradient across each particle causes an additional rotation as the particles travel downstream, fabrication occurs much more rapidly than rotation is induced.

The details of the compensation algorithm are as follows: the lateral coordinate (along the flow direction of the microchannel) of each 3D point in the scan path (indexed as *n*) is shifted by an offset, δ_n, downstream as a function of the flow velocity, v_{medium}, and the time during the scan: $\delta_n = t_n \cdot v_{medium}$ (Figure 54c/f). The result is a part with no warping effects (Figure 54d/g).

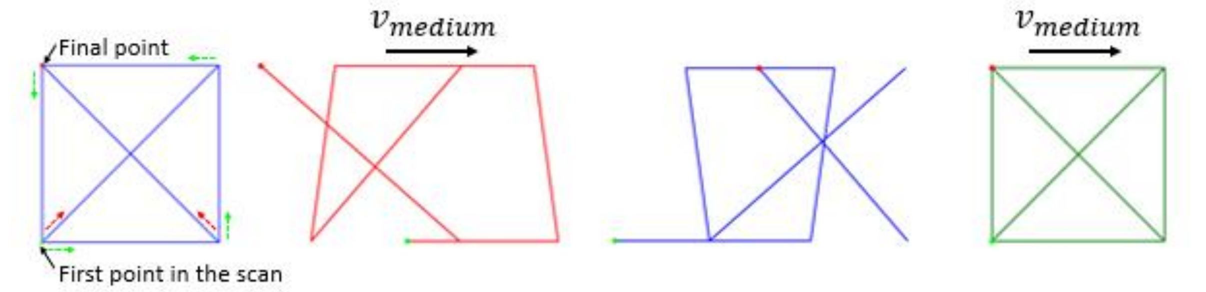
(a) Laser scan path in static media
(b) Printed result in flowing media
(c) Compensated laser scan path in flowing media
(d) Corrected result in flowing media

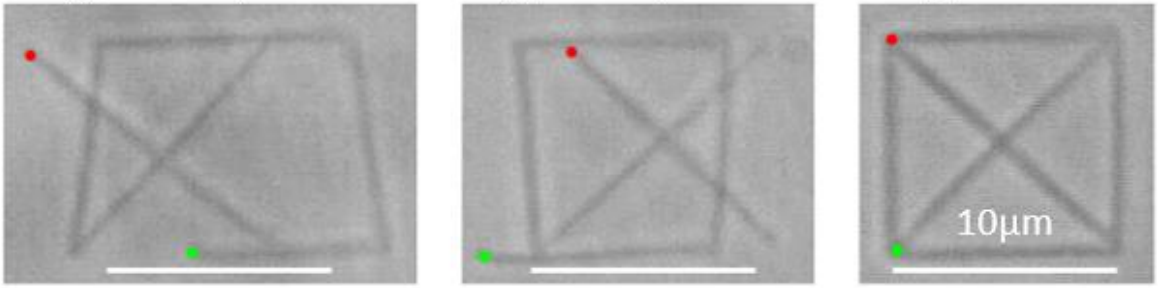
(e) Undercompensated
(f) Overcompensated
(g) Corrected

Figure 54: Laser scan file correction for scanning TP-CFL

We used two different methods to estimate the average velocity of the medium for use in the compensation algorithm. The first and simplest method involved a first-order calculation of the mean flow velocity from the syringe pump's volumetric flow rate, Q, and channel cross-sectional area, $w \times h$. We accounted for the effect of the parabolic profile shape by manually-tuning a scaling factor, s, ranging from 0.5-1.5 until the fabricated parts appeared visually correct under the microscope, i.e. $v_{medium} = s \cdot Q / (w \times h)$. The scaling factor must be calibrated for each printing location, both within the velocity gradient and within the larger microfluidic device (due to pressure-induced deformation to the PDMS).

However, a second and more accurate method for retrieving the flow velocity involved recording a background image of the channel with no objects present, and then two successive images of a flowing object at a known time difference. The flowing object can be a simple polymerized spot – no additional calibration particles are necessary. The fluid velocity was extracted by subtracting the background image from the latter two images and calculating the distance that the object travelled via centroid tracking.

7.4.3 Results

To take advantage of the full scanning bandwidth of the galvanometers and to utilize the maximum volumetric fraction of the photopolymer, fabrication sites were spatially multiplexed along a direction perpendicular to the flow (e.g., 3 colloidal objects were fabricated in parallel in Figs. 3 and 4, each of which was compensated for its own flow velocity). Planar objects (Figure 55 and Figure 56) were created at a rate of 31 particles per second at a linear flow rate of 110µm/sec. 3D objects (Figure 57) were created at a rate of 15 particles per second at a linear flow rate of 100µm/sec. Writing was performed in the middle of the channel’s depth where the gradient of the velocity field was minimal. The focal spot used 70mW of writing power and a linear scan rate of 1mm/sec. The minimum written feature size was observed to be 800nm (for the star-shaped patterns in Fig. 3b). To test the number of objects that could be multiplexed in a vertical scan direction, the gears, f-shaped logos, and stars shown in Figure 56 were fabricated in a wide channel of 50µm depth, 1mm width, and 6mm length.

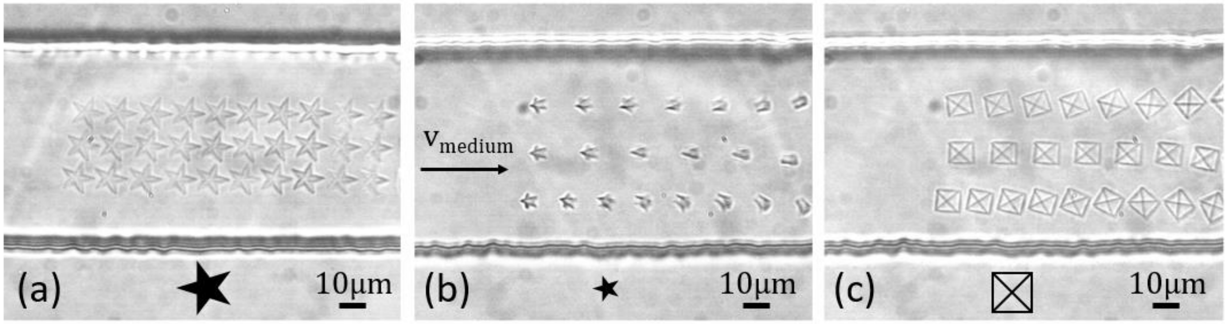

Figure 55: Three examples of 2D structures fabricated with scanning TP-CFL

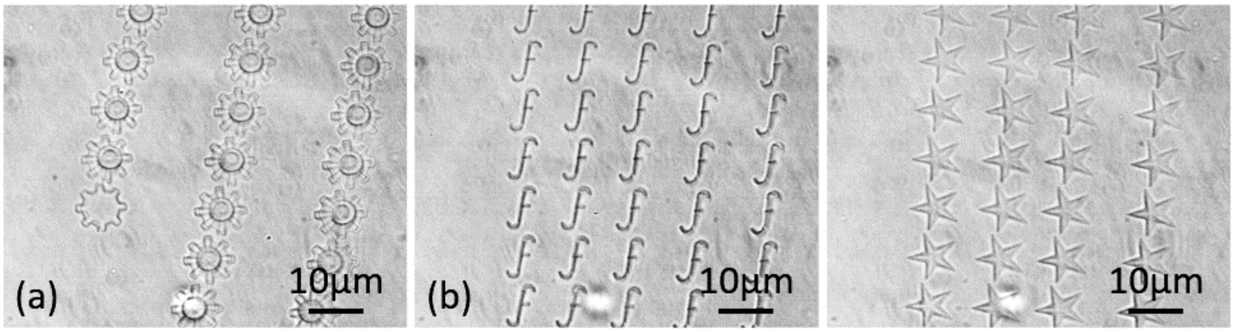

Figure 56: Additional spatial multiplexing of 2D TP-CFL structures

To image features along the writing beam's axis, we fabricated 3D particles at a distance of approximately 10μm from the coverslip, where the gradient of the velocity profile in the channel's boundary layer produces a torque that rotates the particles (Figure 57). By viewing 3D pyramid-shaped particles that have rotated about an axis in the focal plane, we observed that the axial writing resolution was approximately 3μm. This value is considerably smaller than prismatic particles fabricated by most other flow lithography approaches that use a one-photon polymerization reaction. For such reactions the median particle thickness is equal to the thickness of the channel itself minus a small oxygen inhibition layer (e.g. 15μm-thick particles in 20μm channels[213]).

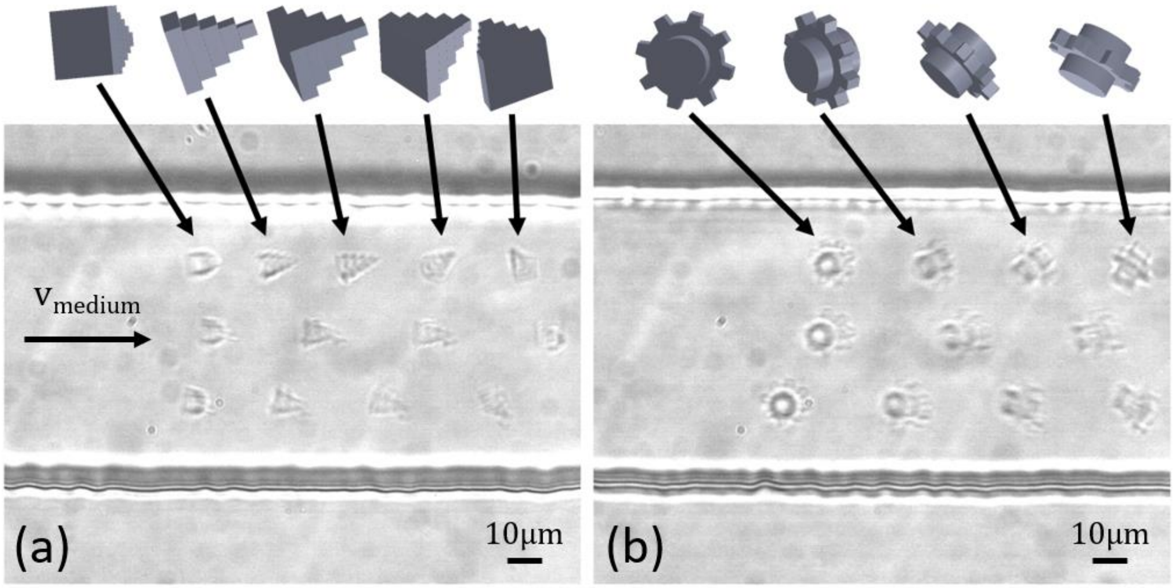

Figure 57: 3D gears and pyramids are rotated by shear forces in the microfluidic channel

The fabrication rate is dependent on the maximum scan rate and the length of the scan path, so further improvements can be expected with a faster galvanometer or scan paths with fewer coordinates. For instance, using a galvanometer with a 10-fold increase in scan rate and a modest increase in the laser writing power of approximately 2x[217], the flow rate can be increased by 10-fold, thereby correspondingly increasing the fabrication rate. Micromirror arrays hold the potential to reach higher scan rates than conventional mirror galvanometers due to their reduced inertia[219]. Diffractive optical elements may be used for further speed-up (e.g. 2-4x) by splitting a single beam for parallelized writing of multiple identical parts simultaneously[80].

This work demonstrates how scanning TP-CFL provides a means to fabricate complex 3D shapes with submicron printing resolution at rates surpassing 10^5 parts per hour. Fabrication rates surpassing 10^6 particles per hour are anticipated with faster scanning galvanometers and flow rates.

To compensate for the continuously-flowing photopolymer, we present a method to adjust the laser's scan path to prevent deformation as the part moves with the flow during fabrication. The scanning TP-CFL approach provides a promising path towards high-throughput fabrication of complex 3D colloidal microparticles for a variety of applications in materials and biological science.

Chapter 8

Conclusions

This thesis outlined four contributions that advance the HOT approach as a viable method for additive manufacturing of microstructures and micromechanisms. The basic working principles of OT, HOT, and the GS phase retrieval algorithm were presented. A description of HOT system components was provided, which included equations for selecting 4-F telescope lenses to produce a desired working area and effective numerical aperture. The main body of the work was divided into four main sections:

- Chapter 3 discussed scanning holographic optical tweezers (SHOT), a new experimental system and associated heuristic algorithm for simultaneously handling large numbers of microparticles across an increased working area.
- Chapter 4 introduced algorithms and control strategies that further increase the number and speed of particles that can be handled with the HOT approach. Improvements in path planning, handling undesired particles, and controller loop rate (via hybrid open- and closed-loop control) were demonstrated.
- Chapter 5 detailed how modeling the dynamics of optically-trapped particles can predict optimal handling conditions (i.e., step sizes and step rates for HOT, SOT, or SHOT systems). Furthermore, Chapter 5 discussed the limitations of GLMT-based simulation of optical force profiles and introduced an experimental method for measuring the full optical force curve on any particle type.

- Chapter 6 outlined a new chemical system and process control strategy for joining microparticles via laser-induced photopolymerization.

The final chapter of this thesis discussed how a HOT system can be combined with a two-photon lithography system for three purposes:

- Section 7.2 demonstrated how TPL can be used for direct writing of microstructures using a two-photon polymerization reaction.
- Section 7.3 provided two case studies in hybrid TPL-based fabrication and HOT-based manipulation of micromechanisms, which are performed in the same system for the first time.
- Section 7.4 detailed how the TPL approach can be used in combination with a microfluidic channel to enable rapid fabrication of arbitrarily-shaped 3D colloidal microparticles.

8.1 Suggested Future Work

Ongoing research will pursue a chemical system that allows for scalable joining of microparticles. Joining efforts would benefit from a polymer that is two-photon-curable in the NIR range but transparent to the wavelength of the handling laser. Additionally, matching of proper microparticle and substrate surface chemistries will support particle-particle and particle-substrate repulsion until joining is desired. Combining a two-photon-polymerization-based joining approach with the automation strategies presented in Chapter 4 may enable automatic and scalable fabrication of microgranular lattices, which may include different constituent materials, particle sizes, and controlled vacancies to achieve desired shock-routing properties.

Additional simulation efforts hold the potential to create a model that can accurately predict particle dynamics under any system parameters (e.g., particle size, refractive index, medium composition, numerical aperture, and M2-value). New simulations will leverage GLMT-simulated or experimentally-measured optical force profiles and include Brownian motion and inter-colloidal effects to better quantify the stochastic metastable boundary relevant to discretely-stepped traps.

Furthermore, additional experimental efforts to verify these simulations will help understand the nature of the stochastic metastable boundary. There has been a considerable amount of literature that discusses the use of constant-velocity drag tests to characterize the stable optical force regime. However, a detailed investigation of stepping parameters (i.e., step size and step rate) holds the potential to determine optimal operating conditions for maximum HOT-based particle manipulation speed.

Additional characterization of the solid photopolymers used in TPL will enable the creation of microstructures and micromechanisms with precisely-tuned properties. Using new approaches to characterize the refractive index, static mechanical, and stress relaxation properties of micro- or nano-scale polymer parts will provide designers with a better understanding of possible bulk properties or behaviors. Simulations of Maxwell’s equations (i.e., non-GLMT-based modelling) may provide a means to predict optical force profiles on arbitrarily-shaped TPL-fabricated structures.

Following the characterization of new TPL polymers, the hybrid TPL-HOT system presented in this work may allow a new means to fabricate microstructures complex geometries that are only possible due to HOT-based manipulation during the build process. Suspending or rotating components during TPL fabrication using the HOT approach may produce complex geometries such as overhanging features that impossible to fabricate with other microfabrication approaches.

Finally, combining the HOT and two-photon continuous-flow-lithography approaches may allow for rapid and continuous fabrication of micromechanisms with embedded strain energy. A hybrid process involving printing and straining of micron-scale parts may be conducted within a continuously-flowing microchannel. The parts may then be collected at the output of the microfluidic device and used for a variety of applications, including cellular mechanics and colloidal self-assembly studies.

8.2 Outlook

The HOT and hybrid TPL/HOT approaches hold vast potential in fabricating micromechanisms and mechanical metamaterials that are impossible to create with other fabrication methods. The ability to dexterously trap, manipulate, and join micro- and nano-particles of various materials, shapes, and with no mechanical contact forces allows HOT to assemble structures with high compositional control and geometry flexibility. Examples of new application areas that may be enabled by the HOT approach include:

- Microgranular lattices, which achieve unique shock routing properties due to the nonlinear Hertzian contacts between closely-packed constituent microspheres

- Mechanical structures with embedded strain energy, which may achieve zero or negative effective stiffness values, or release energy and change shape upon failure
- Supplementing the capabilities of traditional CMOS-based cleanroom processes by adding conductive and nonconductive components in 2D or 3D configurations to MEMS devices

Although biological applications were not discussed in this work, a final promising application area for automated assembly with HOT is the fabrication of living cells into organoids, which are collections of 10^1-10^4 cells that serve as simplified versions of larger organs. By automatically assembling multiple cell types into predefined spatial configurations, scientists may be able to inexpensively and efficiently screen new drugs.

Overall, optical tweezers provide an unprecedented level of dexterous and non-invasive touch for the microscale world. The ability to manipulate and fabricate on this scale offers incredibly promising opportunities in creating mechanisms and metamaterials with entirely new properties that are not found in nature. The microscale world is all around us, as is its infinite potential in science and engineering. According to Richard Feynman’s famous 1959 lecture that produced the wave of interest in the microscale that we are still riding today, “there’s plenty of room at the bottom”.

Appendix A

Glossary of Optical Terms

The **numerical aperture (NA)** of a focusing optic or optical system is a dimensionless number that describes the range of angles that a system can capture or focus[220]:

$$NA = n \cdot \sin\theta \tag{19}$$

The term θ is the angle between the light's axis and the paraxial ray, while n is the index of refraction of the medium. NA is constant across passive media with varying indices of refraction.

Snell's law is a useful equation for calculating changes in propagation angle at medium boundaries with different indices of refraction:

$$n_i \sin(\theta_i) = n_t \sin(\theta_t) \tag{20}$$

Total internal reflection (TIR) occurs at or greater than a critical angle, θ_c, where light transmitting through a medium with a higher index of refraction is entirely reflected from a boundary with a medium with a lower index of refraction:

$$\theta_c = \arcsin\left(\frac{n_t}{n_i}\right) \tag{21}$$

At angles less than the TIR critical angle, both refraction and reflection occur in varying proportions. The **Fresnel reflection** equations describe the fraction of power that is reflected or transmitted:

$$R_s(\theta_t) = \left|\frac{n_{glass}\cos\theta_i - n_{water}\cos\theta_t}{n_{glass}\cos\theta_i + n_{water}\cos\theta_t}\right|^2 \tag{22}$$

$$R_p(\theta_t) = \left|\frac{n_{glass}\cos\theta_t - n_{water}\cos\theta_i}{n_{glass}\cos\theta_t + n_{water}\cos\theta_i}\right|^2 \tag{23}$$

For a plane-polarized radially-symmetric beam, the effective Fresnel reflection can be calculated as an average of the s- and p-polarization terms:

$$R(\theta_t) = \frac{R_s(\theta_t) + R_p(\theta_t)}{2} \tag{24}$$

TEM$_{00}$ laser, such as the continuous wave (532nm) and femtosecond-pulsed (760-1040nm) lasers used in this work, has a radially symmetrical **Gaussian electric field and intensity distribution**[221,222]:

$$E(r) = E_0 \exp\left(-\frac{r^2}{\omega_0^2}\right) \tag{25}$$

$$I(r) = I_0 \exp\left(-\frac{2r^2}{\omega_0^2}\right) \tag{26}$$

$$\theta = \frac{\lambda}{\pi\omega_0} \tag{27}$$

The parameter ω_0 is the *1/e*-radius of the beam and λ is the wavelength of the beam. The Fourier transformation of a Gaussian profile is also a Gaussian profile and solving the Fresnel integral shows that the beam maintains a Gaussian shape at every point along the beam path, although the Gaussian with may change as a result of focusing or free-space diffraction. Additional parameters are provided in Figure 58.

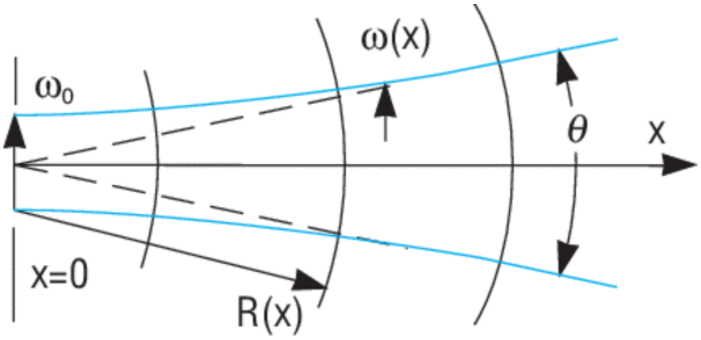

Figure 58: Gaussian beam parameters (image courtesy of Newport Corporation)

Equations for the beam radius and wavefront curvature as a function of the propagation distance, *x*, are as follows:

$$\omega^2(x) = \omega_0^2\left[1 + \left(\frac{\lambda x}{\pi\omega_0^2}\right)^2\right] \tag{28}$$

$$R(x) = x\left[1 + \left(\frac{\pi\omega_0^2}{\lambda x}\right)^2\right] \tag{29}$$

Appendix B

MATLAB Control Software Architecture

This work relied heavily on a custom MATLAB graphical user interface (GUI) that allowed for real-time coordination of the various pieces of experimental hardware necessary for holographic optical trapping and two-photon laser-direct writing. This section discusses basic software structure and software source code is available on reasonable request.

B1. Graphical User Interface

The front panel is organized into sections that each control an aspect of the system (Figure 59). The predominant feature is the camera feed, which can be switched between high (100x) and low (40x) magnification modes. By clicking within the area corresponding to the SLM's active area (denoted by the large rectangle in the image feed), the software will automatically add an optical trap and compute an updated phase pattern using a preselected phase retrieval algorithm and number of algorithm iterations. The user can also choose to select, delete, move, or change the type of the optical traps (e.g., to out-of-plane Gaussian traps[37] or optical vortices[223]).

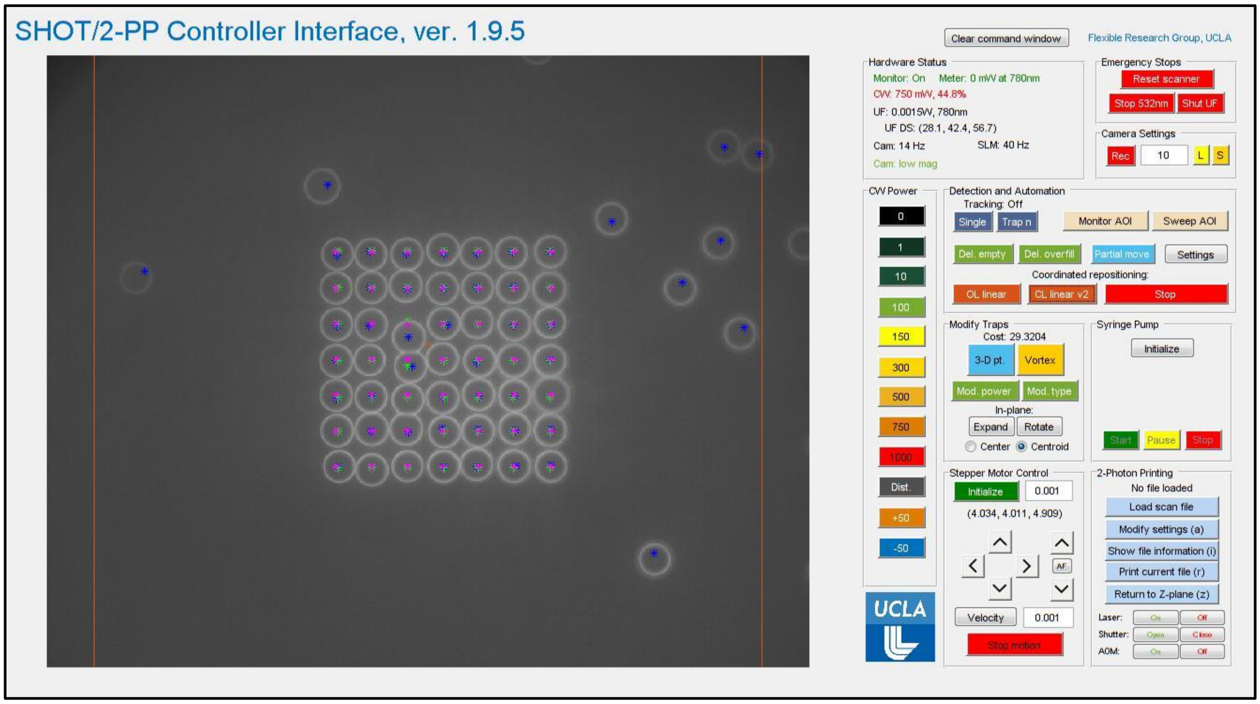

SHOT/2-PP Controller Interface, ver. 1.9.5

Flexible Research Group, UCLA

Hardware Status

Monitor: On
Meter: 0 mW at 780nm
CW: 750 mW, 44.8%
UF: 0.0015W, 780nm
UF DS: (28.1, 42.4, 56.7)
Cam: 14 Hz
SLM: 40 Hz
Cam: low mag

Camera Settings: 10

Detection and Automation
Tracking: Off

Modify Traps
Cost: 29.3204

In-plane: ○ Center ● Centroid

Stepper Motor Control: 0.001
(4.034, 4.011, 4.909)
Velocity: 0.001

2-Photon Printing
No file loaded

Figure 59: MATLAB GUI front panel

Indicators provide the user with real-time updates on the power output of the two lasers and camera acquisition rates. Laser power can be updated using additional front-panel buttons, drop-down menus, or using hotkeys. Buttons on the right-hand side of the front panel control advanced software functions including various image processing routines, automated assembly algorithms, and syringe pump commands. The two-photon lithography controls provide the user with an intuitive workflow for loading a scan file, specifying scan parameters (e.g., scaling, rotation, print rate, and laser power), visualizing a scan file, and initializing a printing process.

The top-level source code file contains the functions behind each button, menu item, hotkey, mouse click command, and additional subroutines that are shared among functions. The main sub-functions that drive GUI interactivity are found in the *KeyPressFcn*, which handles mouse clicks, and *ButtonDownFcn*, which handles keyboard button presses. A detailed list of GUI hotkeys can be found in the Documentation folder of the GUI code repository.

The GUI's opening function (*ManualTrapControl_OpeningFcn*) contains all initialization code that runs when the GUI is first launched. This code serves two main purposes: *(1)* to initialize communication will all hardware (see appendix section B3) and *(2)* to initialize all state variables, which include user settings and dynamic variables like the active optical trap coordinates (all of which are stored in the variable *handles*).

The timing code section (i.e., the sub-functions *TimerSLMFcn*, *TimerCamFcn*, and *TimerMonitorFcn*) handles tasks that are run at prescribed intervals.

- *TimerSLMFcn* handles SLM-based trap movements (i.e., when a trap is linearly stepped in an open-loop fashion from a prescribed start location to a prescribed end location, typically when a trap is selected by right-clicking and then repositioned by left-clicking). Typical SLM timer periods are 0.1 seconds.
- *TimerCamFcn* handles camera frame acquisition and display on the GUI's front panel. Typical frame acquisition rates are 5 Hz.
- *TimerMonitorFcn* gathers and displays hardware status information on the GUI's front panel. Typical monitor information acquisition periods are 2 seconds.

The timers are initialized in the GUI's opening function and are often switched on and off throughout other GUI sub-functions.

The coordinate conversion section (i.e., the sub-functions *CursorCoords2SLMCoords*, *SLMCoords2CursorCoords*, and *CursorCoords2GalvoVolts*) contains important sub-functions that enable rapid conversion from the various coordinate frames used in the code, including the camera view (in units of pixels), the SLM’s working area (pixels), the stepper motor stages (in millimeters), and the scanning galvanometer (voltage). The software depends on the calibration files located in the Lookup Table folder to align and scale each coordinate frame respectively. This code is important for most interactive functions – so that optical traps can be placed precisely with mouse clicks, the stepper motor can be driven to exact locations via mouse clicks, and the galvo scanner can fabricate objects with precise sizes.

More information about the GUI back end can be found in the GUI Programming Guide document in the Documentation folder of the GUI code repository.

B2. Instrument Control Code

Low-level instrument control commands are located within the Hardware folder of the *Optical_System_Code* Git repository. Each piece of hardware includes its own initialization, communication, and shutdown code. A basic summary of the communications protocols can be found in

Table **8**. More information can be found in each device's respective user's and programming manuals.

Table 8: System hardware and communications protocol

Hardware	Vendor	Communication protocol
SLM (HSP256-0532)	Boulder Nonlinear	C++ via MATLAB MEX files over a PCI-e connection
SLM (1920x1152)	Meadowlark Optics	C++ via MATLAB MEX files over USB
CW laser	Laser Quantum	Serial over RS-232
Ultrafast laser	Spectra Physics	Serial over USB
CMOS cameras	Thorlabs	DotNET over USB
CMOS cameras	Basler	GigE (Ethernet)
Power meter	Thorlabs	Serial over USB
Stepper motor controller	Thorlabs	ActiveX over USB
USB DAQ devices	National Instruments	MATLAB ICT w/ NI drivers over USB
Syringe pump	Chemyx	Serial over USB

B3. Additional Functions

Additional MATLAB functions can be found within the subfolders of the *Optical_System_Code* Git repository. This code is categorized by functionality and includes image processing, automation, scanning lithography, and calibration routines.

Appendix C

MATLAB Code for Analysis of the HOT Space-Bandwidth Product

This section provides the raw MATLAB code for the space-bandwidth product calculations described in section 2.2.2. The script uses SLM, microscope objective, and physical layout parameters to explore the tradeoff between working area and effective numerical aperture.

```
clear; clc; close all;

%% System parameters
switch 1
    case 1 % Meadowlark 1920x1152
        SLM_area = [17.7 10.6] * 1e-3; % m
        SLM_pixels = [1920 1152];
        SLM_name = 'UCLA Meadowlark 1920x1152';

        f1 = 250; % mm
        f2 = 200; % mm

        BE1 = -50; % mm
        BE2 = 250; % mm
    case 2 % Boulder Nonlinear Systems HSP256-0532
        SLM_area = [6.14 6.14] * 1e-3; % m
        SLM_pixels = [256 256];
        SLM_name = 'UCLA - BNS256-0532';

        BE1 = -100; % mm
        BE2 = 300; % mm

        f1 = 300; % mm
        f2 = 100; % mm
end

%% Static system parameters
lambda_0 = 532e-9; % green CW wavelength
```

```
% SLM
theta_inc = 9/180 * pi; % Incident angle, 9 deg

% MO
d_MO = 5.8 * 1e-3; % m
f = 2e-3;

d_laser = 1.85*1e-3;

% Header
disp('----- HOT system calculations -----')
disp(' ')

%% --------------- Calculations ---------------
%% Beam expander
d_BE = d_laser * -BE2/BE1;
SLM_illum_area(1) = min([SLM_area(1) d_BE]);
SLM_illum_area(2) = min([SLM_area(2) d_BE]);

%% SLM reach
grating_period = 2*mean(SLM_area./SLM_pixels);
n_ref = 1; % In air
n_inc = n_ref; % For reflection

m = 1; % Order
theta_m = asin((n_inc * sin(theta_inc) - m *
lambda_0/grating_period)/n_ref );
theta_m1_deg = theta_m/pi*180;

m = -1; % Order
theta_mm1 = asin((n_inc * sin(theta_inc) - m *
lambda_0/grating_period)/n_ref );
theta_mm1_deg = theta_mm1/pi*180;

dtheta = abs(theta_mm1 - theta_m)/2; % Single-sided

disp('--- SLM ---')
disp(['SLM description    ' SLM_name])
disp(['SLM pixels:        ' num2str(SLM_pixels(1)) ' x '
num2str(SLM_pixels(2)) ' pixels'])
disp(['SLM illum. area:   ' num2str(SLM_illum_area(1)*1000) ' x '
num2str(SLM_illum_area(2)*1000) ' mm'])
disp(['Pixel pitch:       ' num2str(grating_period*1e6) ' um'])
disp(['Full SLM spread:   ' num2str(dtheta*2/pi*180) ' deg'])
disp(' ')

%% 4-F system
M_lateral = -f2/f1;
```

```
M_angular = -f1/f2;

dtheta_4f = abs(dtheta * M_angular); % Single-sided
SLM_area_4f = abs(SLM_illum_area * M_lateral); % Single-sided

disp('--- 4-f telescope ---')
disp(['f1 = ' num2str(f1) ' mm'])
disp(['f2 = ' num2str(f2) ' mm'])
disp(['Total 4f length = ' num2str(2*f1+2*f2) ' mm'])
% disp(['Beam size at lens 1:    ' num2str(0) ' x ' num2str(0) ' mm'])
disp(['Lateral magnification:  ' num2str(M_lateral)])
disp(['Angular magnification:  ' num2str(M_angular)])
disp(['Projected SLM area:     ' num2str(SLM_area_4f(1)*1000) ' x '
num2str(SLM_area_4f(2)*1000) ' mm'])
disp(['Projected SLM angle:    ' num2str(dtheta_4f*2/pi*180) ' deg'])
disp(' ')

%% Microscope objective (MO)
theta_input = dtheta_4f; % Single-sided, radians
scan_radius = f * tan(theta_input);
NA = 1.45;
alpha = min([min(SLM_area_4f) / d_MO, 1]);

disp('--- Microscope objective (MO) ---')
disp(['Diameter of MO:    ' num2str(d_MO*1e3) ' mm'])
disp(['Diameter of beam:  ' num2str(SLM_area_4f(1)*1e3) ' x '
num2str(SLM_area_4f(2)*1e3) ' mm'])
disp(['Scan diameter:     ' num2str(scan_radius*2e6) ' um'])
disp(['Effective NA:      ' num2str(alpha * NA)])
disp(' ')

%% Warnings
disp('--- Warnings ---')
warn = 0;
if any(abs(d_MO-SLM_area_4f) > 1e-3)
    warning('MO input beam is incorrectly sized')
    warn = 1;
end

if scan_radius*2e6 < 75
    warning('Working area is small')
    warn = 1;
end

if (2*f1+2*f2) > 1200
    warning('4-f system is long')
    warn = 1;
end
```

```
if ~warn
    disp('No warnings')
end
```

Appendix D: MATLAB Code for Analysis of Reflection at a Medium Boundary

This section provides the raw MATLAB code to simulate reflection and apodization effects at a medium boundary as described in section 5.4.

```
clear; clc; close all;

%% Simulation parameters
n_rays = 131; % Number of rays to simulate, can be any integer

max_angle = asind(1.45/1.52); % asind(NA/n_glass)
f = 5.8/2 / tand(max_angle); % effective focal length

sigma = 1.9; % sigma value for Gaussian MO input
X = linspace(-5.8/2, 5.8/2, n_rays);
wP = exp(-X.^2/2/sigma^2); % Gaussian distribution for power

%% Define all surfaces
surf{1}.x = 0;
surf{1}.y = 5.8/2; % Arbitrary height - must be sufficiently large to
capture all rays, but beyond that any extra height is just for
visualization
surf{1}.n = 1.52;
surf{1}.tag = 'MO entrance';

surf{2}.x = f-0.17-0.13;
surf{2}.y = 1.5;
surf{2}.n = 1.52;
surf{2}.tag = 'MO exit';

surf{3}.x = f-0.13; % THIS VALUE controls how far into the water we
trap. The MO is designed for a max sample WD of 0.13, so (f-0.13) is
the furthest we can trap into the sample.
surf{3}.y = 1;
surf{3}.n = 1.33;
```

```
surf{3}.tag = 'Bottom of coverslip';

surf{4}.x = inf;
surf{4}.y = [];
surf{4}.n = 1.33;
surf{4}.tag = 'Water';

%% Initialize rays
h_rays = linspace(-surf{1}.y, surf{1}.y, n_rays);
for k = 1:n_rays
    rays{k}.x(1) = surf{1}.x;
    rays{k}.y(1) = h_rays(k);
    rays{k}.t(1) = atand(-h_rays(k) / f); % initial angle
    rays{k}.w_lost = 0;
    rays{k}.w(1) = wP(k); % weighting
    rays{k}.TIR = false; % rays are not lost to TIR by default
    rays{k}.reflections = []; % Fresnel reflected rays go in here
end

%% Propagate
bump = 0.25;
for k = 1:n_rays
    for s = 1:3
        t1 = rays{k}.t(s); % current theta

        x1 = rays{k}.x(s); % current x-location
        x2 = surf{s+1}.x * 1.1; % next x-location, placed beyond
surface to calculate intersection
        if isinf(x2)
            x2 = surf{s}.x + bump;
        end

        y1 = rays{k}.y(s); % current y-height of ray
        y2 = y1 + tand(t1)*(x2-x1); % next y-height of ray, placed
beyond surface to calculate intersection

        L1 = [x1 x2; y1 y2]; % ray information used to calculate
intersection

        xs = surf{s+1}.x; % surface locations
        if isinf(xs)
            xs = surf{s}.x + bump;
            ys = 1000;
        else
            ys = surf{s+1}.y;
        end
```

```
        L2 = [xs xs; -ys ys]; % surface information used to calculate
intersection

        P = InterX(L1, L2); % intersection between ray and surface

        xi = P(1); % x-loc of intersection between ray and next
surface
        yi = P(2); % y-loc of intersection

        rays{k}.x(s+1) = xi; % record this information into ray
structure
        rays{k}.y(s+1) = yi;

        n1 = surf{s}.n; % current IOR
        n2 = surf{s+1}.n; % next IOR

        t2 = asind(n1*sind(t1)/n2); % new ray angle based on Snell's
law
        rays{k}.t(s+1) = t2; % record this information into ray
structure

        % Check for TIR
        t_critical = asind(n2/n1);
        if abs(t1) > abs(t_critical)
            rays{k}.TIR = true; % ray is lost to TIR
            rays{k}.w_lost = rays{k}.w;
            rays{k}.w = 0; % its power is zero
            break % do not continue calculating this ray
        end

        % Calculate Fresnel losses
        ti = t1/180*pi; % convert to radians for now
        tt = t2/180*pi;
        ni = n1;
        nt = n2;

        r_perp = (ni*cos(ti)-nt*cos(tt))/(ni*cos(ti)+nt*cos(tt));
        t_perp = 2*ni*cos(ti)/(ni*cos(ti)+nt*cos(tt));

        r_para = (ni*cos(tt)-nt*cos(ti))/(ni*cos(tt)+nt*cos(ti));
        t_para = 2*ni*cos(ti)/(ni*cos(tt)+nt*cos(ti));

        t = mean([t_perp, t_para]); % average of perpendicular and
parallel polarizations

        T = (nt*cos(tt))/(ni*cos(ti)) * t_perp^2; % transmission
coefficient
        R = 1-T; % reflection coefficient
```

```
        if R > 0.000001 % if reflection is significant, record info
into structure
            rays{k}.reflections{end+1}.x = xi;
            rays{k}.reflections{end}.y = yi;
            rays{k}.reflections{end}.R = R;
            rays{k}.reflections{end}.t = t1;
        end

        rays{k}.w = rays{k}.w * T; % weight its power by the
transmission coefficient
    end
end

%% Analysis
disp(['Relative total power:  1'])
Pf = 0;
P_TIR = 0;
for k = 1:n_rays
    Pf = Pf + rays{k}.w; % sum of all power weights among rays
    P_TIR = P_TIR + rays{k}.w_lost;
end
disp(['Power lost to TIR:     ' num2str(sum(P_TIR)/sum(wP))])
disp(['Power lost to Fresnel: ' num2str( (sum(wP)-sum(Pf)-
sum(P_TIR))/sum(wP) )])
disp(['Relative final power:  ' num2str(sum(Pf)/sum(wP))])
disp(' ')

%% Calculate trap elongation
% We will calculate where the symmetric marginal rays intersect, and
where
% the inner-most off-axis rays intersect. The difference in their
% x-locations is the length or 'elongation' of the trap

% Intersection of symmetric rays just off-axis
if mod(n_rays,2) == 0 % n_rays is even
    I1 = n_rays/2;
    I2 = n_rays/2+1;
else % n_rays is odd
    I1 = floor(n_rays/2);
    I2 = ceil(n_rays/2);
end
L1 = [rays{I1}.x; rays{I1}.y];
L2 = [rays{I2}.x; rays{I2}.y];
P1 = InterX(L1, L2);

% Calculate intersection of outer marginal rays
I3 = 1;
```

```
bool = true;
while bool
    if rays{I3}.TIR == 1
        I3 = I3 + 1; % Look for outermost ray not lost to TIR
    else bool = false;
    end
end
I4 = n_rays;
bool = true;
while bool
    if rays{I4}.TIR == 1
        I4 = I4 - 1; % Look for other outermost ray not lost to TIR
    else bool = false;
    end
end
L3 = [rays{I3}.x; rays{I3}.y];
L4 = [rays{I4}.x; rays{I4}.y];
P2 = InterX(L3, L4);

disp(['Trap length (z-dir): ' num2str(abs(P1(1)-P2(1))*1000) ' um'])

%% Plot
hold on
axis equal

for s = 1:length(surf)
    if ~isempty(surf{s}.y)
        x = surf{s}.x;
        y = surf{s}.y;
        line_black = plot([x x], [-y y], 'k--');
        str = [surf{s}.tag ', n=' num2str(surf{s}.n)];
        text(x, y*(mod(s,2)-0.5)*2, str)
    end
end

for k = 1:n_rays
    color = [0 rays{k}.w 0];
    if k == round(n_rays/2)
        line_ray = plot(rays{k}.x, rays{k}.y, 'color', color);
    else
        plot(rays{k}.x, rays{k}.y, 'color', color)
    end
    if rays{k}.TIR
        dot_red = plot(rays{k}.x(end), rays{k}.y(end), 'r.');
    end

    for r = 1:length(rays{k}.reflections)
        ref = rays{k}.reflections{r};
```

```
        x1 = ref.x;
        y1 = ref.y;
        x2 = x1 - ref.R*cosd(ref.t);
        y2 = y1 + ref.R*sind(ref.t);

        line_blue = plot([x1 x2], [y1 y2], 'b');
    end
end

dot_mag = plot(P1(1), P1(2),'m.');
plot(P2(1), P2(2),'m.')

plot(-wP, X)

l = legend([line_ray, line_black, line_blue, dot_red, dot_mag], 'Ray',
'Interface', 'Fresnel reflection', 'TIR loss', 'Intersection of rays',
'Location', 'West');

% ylim([-yview yview])
xlabel('x [mm]')
ylabel('y [mm]')
set(gcf, 'color', 'w')
```

References

1. Hopkins, J. B. & Culpepper, M. L. Synthesis of multi-degree of freedom, parallel flexure system concepts via Freedom and Constraint Topology (FACT) - Part I: Principles. *Precis. Eng.* **34,** 259–270 (2010).
2. Bendsøe, M. P. & Sigmund, O. *Topology Optimization: Theory, Methods, and Applications*. (Springer Berlin Heidelberg, 2004). doi:10.1007/978-3-662-05086-6
3. Florijn, B., Coulais, C. & Van Hecke, M. Programmable mechanical metamaterials. *Phys. Rev. Lett.* **113,** 1–5 (2014).
4. Liu, A. Q., Zhu, W. M., Tsai, D. P. & Zheludev, N. I. Micromachined tunable metamaterials: A review. *J. Opt. (United Kingdom)* **14,** (2012).
5. Lee, J. H., Singer, J. P. & Thomas, E. L. Micro-/nanostructured mechanical metamaterials. *Adv. Mater.* **24,** 4782–4810 (2012).
6. Silverberg, J. L. *et al.* Using origami design principles to fold reprogrammable mechanical metamaterials. *Science (80-.).* **345,** 647–650 (2014).
7. Bertoldi, K., Vitelli, V., Christensen, J. & Van Hecke, M. Flexible mechanical metamaterials. *Nat. Rev. Mater.* **2,** (2017).
8. Wang, Q. *et al.* Lightweight mechanical metamaterials with tunable negative thermal expansion. *Phys. Rev. Lett.* **117,** 175901 (2016).
9. Hopkins, J. B. *et al.* Design of nonperiodic microarchitectured materials that achieve graded thermal expansions. *J. Mech. Robot.* **8,** 51010 (2016).
10. Haghpanah, B., Salari-Sharif, L., Pourrajab, P., Hopkins, J. & Valdevit, L. Multistable shape-reconfigurable architected materials. *Adv. Mater.* **28,** 7915–7920 (2016).
11. Song, Y., Dohm, P. C., Haghpanah, B., Vaziri, A. & Hopkins, J. B. An active microarchitectured material that utilizes piezo actuators to achieve programmable properties. *Adv. Eng. Mater.* **18,** 1113–1117 (2016).
12. Shaw, L. A. & Hopkins, J. B. An Actively Controlled Shape-Morphing Compliant Microarchitectured Material. *J. Mech. Robot.* **8,** 21019 (2015).
13. Frenzel, T., Kadic, M. & Wegener, M. Three-dimensional mechanical metamaterials with

a twist. *Science (80-.).* **358,** 1072–1074 (2017).

14. Boechler, N. *et al.* Interaction of a Contact Resonance of Microspheres with Surface Acoustic Waves. *Phys. Rev. Lett.* **111,** 36103 (2013).
15. Ponson, L. *et al.* Nonlinear waves in disordered diatomic granular chains. *Phys. Rev. E* **82,** 21301 (2010).
16. Jiang, S., Sewell, T. D. & Thompson, D. L. Molecular Dynamics Simulations of Shock Wave Propagation through the Crystal–Melt Interface of (100)-Oriented Nitromethane. *J. Phys. Chem. C* **120,** 22989–23000 (2016).
17. Donahue, C. M., Anzel, P. W. J., Bonanomi, L., Keller, T. A. & Daraio, C. Experimental realization of a nonlinear acoustic lens with a tunable focus. *Appl. Phys. Lett.* **104,** 14103 (2014).
18. Roichman, Y. & Grier, D. G. Holographic assembly of quasicrystalline photonic heterostructures. *Opt. Express* **13,** 5434–5439 (2005).
19. Lebedew, P. Untersuchungen über die Druckkräfte des Lichtes. *Ann. Phys.* **311,** 433–458 (1901).
20. Ashkin, A. Acceleration and trapping of particles by radiation pressure. *Phys. Rev. Lett.* **24,** 156–159 (1970).
21. Chu, S., Hollberg, L., Bjorkholm, J. E., Cable, A. & Ashkin, A. Three-dimensional viscous confinement and cooling of atoms by resonance radiation pressure. *Phys. Rev. Lett.* **55,** 48–51 (1985).
22. Hajizadeh, F. & Reihani, S. N. S. Optimized optical trapping of gold nanoparticles. *Opt. Express* **18,** 551–9 (2010).
23. Ashkin, A., Dziedzic, J. M., Bjorkholm, J. E. & Chu, S. Observation of a single-beam gradient force optical trap for dielectric particles. *Opt. Lett.* **11,** 288 (1986).
24. Ashkin, A., Dziedzic, J. M. & Yamane, T. Optical trapping and manipulation of single cells using infrared laser beams. *Nature* **330,** 769–771 (1987).
25. Zhang, H. & Liu, K.-K. Optical tweezers for single cells. *J. R. Soc. Interface* **5,** 671–690 (2008).
26. Applegate, R. W., Squier, J., Vestad, T., Oakey, J. & Marr, D. W. . Optical trapping,

manipulation, and sorting of cells and colloids in microfluidic systems with diode laser bars. *Conf. Lasers Electro-Optics/Quantum Electron. Laser Sci. Photonic Appl. Syst. Technol. (2005), Pap. CFN2* **12,** CFN2 (2005).

27. Ozkan, M. *et al.* Optical manipulation of objects and biological cells in microfluidic devices. *Biomed. Microdevices* **5,** 61–67 (2003).
28. Xin, H., Liu, Q. & Li, B. Non-contact fiber-optical trapping of motile bacteria: dynamics observation and energy estimation. *Sci. Rep.* **3,** 1–8 (2014).
29. Arias-Gonzalez, J. R. in 273–304 (2013). doi:10.1007/978-94-007-6552-8_9
30. Wang, M. D., Yin, H., Landick, R., Gelles, J. & Block, S. M. Stretching DNA with optical tweezers. *Biophys. J.* **72,** 1335–1346 (1997).
31. Chu, S., Bjorkholm, J. E., Ashkin, A. & Cable, A. Experimental observation of optically trapped Atoms. *Phys. Rev. Lett.* **57,** 314–317 (1986).
32. Dufresne, E. R., Spalding, G. C., Dearing, M. T., Sheets, S. A. & Grier, D. G. Computer-generated holographic optical tweezer arrays. *Rev. Sci. Instrum.* **72,** 1810–1816 (2001).
33. Reicherter, M., Haist, T., Wagemann, E. U. & Tiziani, H. J. Optical particle trapping with computer-generated holograms written on a liquid-crystal display. *Opt. Lett.* **24,** 608 (1999).
34. Grier, D. G. A revolution in optical manipulation. *Nature* **424,** 810–6 (2003).
35. Arlt, J., Sibbett, W. & Dholakia, K. Optical micromanipulation using a Bessel light beam. **197,** 239–245 (2001).
36. Gahagan, K. T. & Swartzlander, G. A. Optical vortex trapping of particles. *Opt. Lett.* **21,** 827–9 (1996).
37. Grier, D. G. & Roichman, Y. Holographic optical trapping. *Appl. Opt.* **45,** 880–7 (2006).
38. Diekmann, R. *et al.* Nanoscopy of bacterial cells immobilized by holographic optical tweezers. *Nat. Commun.* **7,** 13711 (2016).
39. León-Montiel, R. D. J. & Quinto-Su, P. A. Noise-enabled optical ratchets. *Sci. Rep.* **7,** 1–6 (2017).
40. Ostendorf, A., Ghadiri, R. & Ksouri, S. I. Optical tweezers in microassembly. *Proc. SPIE* **8607,** 86070U–86070U–11 (2013).
41. Tanaka, Y., Tsutsui, S. & Kitajima, H. Design of hybrid optical tweezers system for

automated 3D micro manipulation. *Proc. SPIE* **8550,** 85501X–1–7 (2012).

42. Brouhard, G. J., III, H. T. S. & Hunt, A. J. Advanced optical tweezers for the study of cellular and molecular biomechanics. *Biomed. Eng. (NY).* **50,** 121–125 (2003).
43. Deng, Y., Bechhoefer, J. & Forde, N. R. Brownian motion in a modulated optical trap. *J. Opt. A Pure Appl. Opt.* **9,** (2007).
44. Shaw, L. A., Spadaccini, C. M. & Hopkins, J. B. Scanning holographic optical tweezers. *Opt. Lett.* **42,** 2862–2865 (2017).
45. Zheng, X. *et al.* Design and optimization of a light-emitting diode projection micro-stereolithography three-dimensional manufacturing system. *Rev. Sci. Instrum.* **83,** 125001 (2012).
46. Ng, M. R., Moran, B., Bekker, L. & Dudukovic, N. *Large area projection microstereolithography: characterization and optimization of 3D printing parameters*. (2016). doi:10.2172/1305839
47. Shusteff, M. *et al.* One-step volumetric additive manufacturing of complex polymer structures. *Sci. Adv.* **3,** eaao5496 (2017).
48. Wu, E.-S., Strickler, J. H., Harrell, W. R. & Webb, W. W. Two-photon lithography for microelectronic application. 776 (1992). doi:10.1117/12.130367
49. Jeon, S., Malyarchuk, V., Rogers, J. A. & Wiederrecht, G. P. Fabricating three-dimensional nanostructures using two photon lithography in a single exposure step. *Opt. Express* **14,** 2300 (2006).
50. D’Angelo, M., Chekhova, M. V. & Shih, Y. Two-photon diffraction and quantum lithography. *Phys. Rev. Lett.* **87,** 013602/1-013602/4 (2001).
51. Juodkazis, S., Mizeikis, V., Seet, K. K., Miwa, M. & Misawa, H. Two-photon lithography of nanorods in SU-8 photoresist. *Nanotechnology* **16,** 846–849 (2005).
52. Svoboda, K. & Block, S. M. Optical trapping of metallic Rayleigh particles. *Opt. Lett.* **19,** 930–2 (1994).
53. Agarwal, R., Ladavac, K., Roichman, Y., Lieber, C. M. & Grier, D. G. Manipulation and assembly of nanowires with holographic optical traps. **13,** 1135–1140 (2005).
54. Terray, A., Oakey, J. & Marr, D. W. M. Fabrication of linear colloidal structures for

microfluidic applications. *Appl. Phys. Lett.* **81,** 1555 (2002).

55. Shaw, L. A. *et al.* Holographic optical assembly and photopolymerized joining of planar microspheres. *Opt. Lett.* **41,** 3571 (2016).
56. Dawood, F., Qin, S., Li, L., Lin, E. Y. & Fourkas, J. T. Simultaneous microscale optical manipulation, fabrication and immobilisation in aqueous media. *Chem. Sci.* **3,** 2449 (2012).
57. Ghadiri, R., Weigel, T., Esen, C. & Ostendorf, A. Microfabrication by Optical Tweezers. in *Proc. of SPIE* (eds. Pfleging, W., Lu, Y. & Washio, K.) **7921,** 792102-792102–9 (2011).
58. Castelino, K., Satyanarayana, S. & Sitti, M. Manufacturing of two and three-dimensional micro/nanostructures by integrating optical tweezers with chemical assembly. *Robotica* **23,** 435–439 (2005).
59. Kirkham, G. R. *et al.* Precision assembly of complex cellular microenvironments using holographic optical tweezers. *Sci. Rep.* **5,** 8577 (2015).
60. Villangca, M. J., Palima, D., Banas, A. R. & Gluckstad, J. Light-driven micro-tool equipped with a syringe function. *Light Sci Appl.* **5,** e16148 (2016).
61. Ksouri, S. I. *et al.* Holographic optical tweezers: microassembling of shape-complementary 2PP building blocks. **9164,** 916433 (2014).
62. Köhler, J., Ksouri, S. I., Esen, C. & Ostendorf, A. Optical screw-wrench for microassembly. *Microsystems Nanoeng.* **3,** 16083 (2017).
63. Köhler, J. *et al.* Optical assembly of microsnap-fits fabricated by two-photon polymerization. *Opt. Eng.* **56,** 1 (2017).
64. Gullo, M. R., Jacot-Descombes, L. & Brugger, J. In-liquid MEMS assembly by optical trapping. *Proc. IEEE Int. Conf. MEMS* 78–81 (2013). doi:10.1109/MEMSYS.2013.6474181
65. Khanolkar, A. *et al.* A self-assembled metamaterial for Lamb waves. *Appl. Phys. Lett.* **107,** 71903 (2015).
66. Awasthi, A., Wang, Z., Broadhurst, N. & Geubelle, P. Impact response of granular layers. *Granul. Matter* **17,** 21–31 (2015).
67. Neto, P. & Nussenzveig, H. Theory of optical tweezers. *Europhys. Lett.* **50,** 702–708 (2000).
68. Bowman, R. W. & Padgett, M. J. Three dimensional touch and vision for the micro-world.

(University of Glasgow, 2012). at <http://theses.gla.ac.uk/3664/>

69. Min, C. *et al.* Focused plasmonic trapping of metallic particles. *Nat. Commun.* **4,** 2891 (2013).

70. Juan, M. L., Righini, M. & Quidant, R. Plasmon nano-optical tweezers. *Nat. Photonics* **5,** 349–356 (2011).

71. Zhang, Y. *et al.* A Plasmonic Spanner for Metal Particle Manipulation. *Sci. Rep.* **5,** 15446 (2015).

72. Lock, J. a. & Gouesbet, G. Generalized Lorenz–Mie theory and applications. *J. Quant. Spectrosc. Radiat. Transf.* **110,** 800–807 (2009).

73. Nieminen, T. A. *et al.* Optical tweezers computational toolbox. (2007).

74. Nieminen, T. A., Rubinsztein-Dunlop, H. & Heckenberg, N. R. Calculation and optical measurement of laser trapping forces on non-spherical particles. *J. Quant. Spectrosc. Radiat. Transf.* **70,** 627–637 (2001).

75. Im, K. *et al.* Calculation of Optical Trapping Forces on Microspheres in the Ray Optics Regime. **40,** 930–933 (2002).

76. Callegari, A., Mijalkov, M., Gököz, A. B. & Volpe, G. Computational toolbox for optical tweezers in geometrical optics. *J. Opt. Soc. Am. B* **32,** B11 (2015).

77. Park, I.-Y., Sung, S.-Y., Lee, J.-H. & Lee, Y.-G. Manufacturing micro-scale structures by an optical tweezers system controlled by five finger tips. *J. Micromechanics Microengineering* **17,** N82–N89 (2007).

78. Sasaki, K., Koshioka, M., Misawa, H. & Kitamura, N. Optical trapping laser beam of a metal article and a water droplet by a scanning. *Appl. Phys. Lett.* **60,** 807–809 (1993).

79. Weiner, A. M. Femtosecond pulse shaping using spatial light modulators. *Rev. Sci. Instrum.* **71,** 1929–1960 (2000).

80. Vizsnyiczai, G., Kelemen, L. & Ormos, P. Holographic multi-focus 3D two-photon polymerization with real-time calculated holograms. *Opt. Express* (2014).

81. Goodman, J. W. *Introduction to Fourier optics*. (1968).

82. Gerchberg, R. W. & Saxton, W. O. A practical algorithm for the determination of phase from image and diffraction plane pictures. *Optik (Stuttg).* **35,** 237–246 (1972).

83. Persson, M. *Advances in Holographic Optical Trapping*. (2013).

84. Kotlyar, V. V., Seraphimovich, P. G. & Soifer, V. A. Iterative weight-based method for calculating kinoforms. in (eds. Kuznetsov, N. A. & Soifer, V. A.) 177–183 (1995). doi:10.1117/12.199632

85. Spalding, G. C., Courtial, J. & Leonardo, R. Di. Holographic optical tweezers.

86. Brady, D. J. Analysis of Fresnel diffraction by FFTs. at <http://www.disp.duke.edu/~dbrady/ece371/notes/ftf/ftf.html>

87. Sinclair, G. *et al.* Interactive application in holographic optical tweezers of a multi-plane Gerchberg-Saxton algorithm for three-dimensional light shaping. *Opt. Express* **12,** 1665–1670 (2004).

88. Seldowitz, M. A., Allebach, J. P. & Sweeney, D. W. Synthesis of digital holograms by direct binary search. *Appl. Opt.* **26,** 2788 (1987).

89. Montes-Usategui, M., Pleguezuelos, E., Andilla, J. & Martín-Badosa, E. Fast generation of holographic optical tweezers by random mask encoding of Fourier components. *Opt. Express* **14,** 2101 (2006).

90. Mico, V., Zalevsky, Z., García-Martínez, P. & García, J. Superresolved imaging in digital holography by superposition of tilted wavefronts. *Appl. Opt.* **45,** 822–828 (2006).

91. Poland, S. P., Krstajić, N., Knight, R. D., Henderson, R. K. & Ameer-Beg, S. M. Development of a doubly weighted Gerchberg-Saxton algorithm for use in multibeam imaging applications. *Opt. Lett.* **39,** 2431–4 (2014).

92. Zhang, H., Xie, J., Liu, J. & Wang, Y. Elimination of a zero-order beam induced by a pixelated spatial light modulator for holographic projection. *Appl. Opt.* **48,** 5834 (2009).

93. Liang, J., Wu, S.-Y., Fatemi, F. K. & Becker, M. F. Suppression of the zero-order diffracted beam from a pixelated spatial light modulator by phase compression. *Appl. Opt.* **51,** 3294 (2012).

94. Hernandez, O., Guillon, M., Papagiakoumou, E. & Emiliani, V. Zero-order suppression for two-photon holographic excitation. *Opt. Lett.* **39,** 5953–5956 (2014).

95. Barbastathis, G., Sheppard, C. & Oh, S. B. Introduction to spatial filtering. *MIT 2.71/2.710* (2009). at <https://ocw.mit.edu/courses/mechanical-engineering/2-71-optics-spring-

2009/video-lectures/lecture-19-the-4f-system-binary-amplitude-pupil-masks/MIT2_71S09_lec19.pdf>

96. Rumpf, R. C. Lecture #9: Diffraction gratings. 7 (2018). at <http://emlab.utep.edu/ee5390em21/Lecture 9 -- Diffraction gratings.pdf>

97. Eddings, M. a, Johnson, M. A. & Gale, B. K. Determining the optimal PDMS–PDMS bonding technique for microfluidic devices. *J. Micromechanics Microengineering* **18,** 67001 (2008).

98. Duffy, D. C., McDonald, J. C., Schueller, O. J. A. & Whitesides, G. M. Rapid prototyping of microfluidic systems in poly(dimethylsiloxane). *Anal. Chem.* **70,** 4974–4984 (1998).

99. Chapin, S. C., Germain, V. & Dufresne, E. R. Automated trapping, assembly, and sorting with holographic optical tweezers. *Opt. Express* **14,** 13095–13100 (2006).

100. Curtis, J. E., Koss, B. A. & Grier, D. G. Dynamic holographic optical tweezers. *Opt. Commun.* **207,** 169–175 (2002).

101. Wallen, S. P., Maznev, A. A. & Boechler, N. Dynamics of a monolayer of microspheres on an elastic substrate. *Phys. Rev. B* **92,** 174303 (2015).

102. Nesterenko, V. F. Propagation of Nonlinear Compression Pulses in Granular Media. *J. Appl. Mech. Tech. Phys.* **24,** 733–743 (1983).

103. Akselrod, G. M. *et al.* Laser-Guided Assembly of Heterotypic Three-Dimensional Living Cell Microarrays. *Biophys. J.* **91,** 3465–3473 (2006).

104. Cižmár, T., Romero, L. C. D., Dholakia, K. & Andrews, D. L. Multiple optical trapping and binding: new routes to self-assembly. *J. Phys. B* **43,** 102001 (2010).

105. Hartigan, J. A. & Wong, M. A. Algorithm AS 136: A K-Means Clustering Algorithm. *Appl. Stat.* **28,** 100 (1979).

106. Gutin, G., Yeo, A. & Zverovich, A. Traveling salesman should not be greedy: domination analysis of greedy-type heuristics for the TSP. *Discret. Appl. Math.* **117,** 81–86 (2002).

107. Ong, H. L. & Moore, J. B. Worst-case analysis of two travelling salesman heuristics. *Oper. Res. Lett.* **2,** 273–277 (1984).

108. Di Leonardo, R., Ianni, F. & Ruocco, G. Computer generation of optimal holograms for optical trap arrays. *Opt. Express* **15,** 1913–22 (2007).

109. Sarshar, M., Wong, W. T. & Anvari, B. Comparative study of methods to calibrate the stiffness of a single-beam gradient-force optical tweezers of various laser trapping powers. *J. Biomed. Opics* **19,** 115001 (2014).

110. Sinclair, G. *et al.* Assembly of 3-dimensional structures using programmable holographic optical tweezers. *Opt. Express* **12,** 5475–80 (2004).

111. Wu, Y., Sun, D., Huang, W. & Xi, N. Dynamics analysis and motion planning for automated cell transportation. *IEEE/ASME Trans. Mechatronics* **18,** 706–713 (2013).

112. Chowdhury, S. *et al.* Automated cell transport in optical tweezers-assisted microfluidic chambers. *IEEE Trans. Autom. Sci. Eng.* **10,** 980–989 (2013).

113. Chen, H. & Sun, D. Moving groups of microparticles into array with a robot-tweezers manipulation system. *IEEE Trans. Robot.* **28,** 1069–1080 (2012).

114. Chen, H., Wang, C. & Lou, Y. Flocking multiple microparticles with automatically controlled optical tweezers: solutions and experiments. *IEEE Trans. Biomed. Eng.* **60,** 1518–1527 (2013).

115. Thakur, A. *et al.* Indirect pushing based automated micromanipulation of biological cells using optical tweezers. *Int. J. Rob. Res.* **33,** 1098–1111 (2014).

116. Chapin, S. C., Germain, V. & Dufresne, E. R. Automated trapping, assembly, and sorting with holographic optical tweezers. *Opt. Express* **14,** 13095–13100 (2006).

117. Boechler, N. *et al.* Interaction of a contact resonance of microspheres with surface acoustic waves. *Phys. Rev. Lett.* **111,** 36103 (2013).

118. Tanaka, Y., Kawada, H., Hirano, K., Ishikawa, M. & Kitajima, H. Automated manipulation of non-spherical micro-objects using optical tweezers combined with image processing techniques. *Opt. Express* **16,** 15115–15122 (2008).

119. Nieminen, T. A. *et al.* Optical tweezers computational toolbox. *J. Opt. A Pure Appl. Opt.* **9,** S196–S203 (2007).

120. Kuhn, H. W. The Hungarian method for the assignment problem. *Nav. Res. Logist. Q.* **2,** 83–97 (1955).

121. Pundir, P. S., Porwal, S. K. & Singh, B. P. A new algorithm for solving linear bottleneck assignment problem. *J. Inst. Sci. Technol.* **20,** 101–102 (2015).

122. McGorty, R., Fung, J., Kaz, D. & Manoharan, V. N. Colloidal self-assembly at an interface. *Mater. Today* **13,** 34–42 (2010).

123. Li, G., Zhang, S. & Zentgraf, T. Nonlinear photonic metasurfaces. *Nat. Rev. Mater.* **2,** 1–14 (2017).

124. Wu, M. H. & Whitesides, G. M. Fabrication of arrays of two-dimensional micropatterns using microspheres as lenses for projection photolithography. *Appl. Phys. Lett.* **78,** 2273–2275 (2001).

125. Nam, H. J., Jung, D. Y., Yi, G. R. & Choi, H. Close-packed hemispherical microlens array from two-dimensional ordered polymeric microspheres. *Langmuir* **22,** 7358–7363 (2006).

126. Chowdhury, S. *et al.* Automated indirect transport of biological cells with optical tweezers using planar gripper formations. 267–272 (2012). doi:10.1109/CoASE.2012.6386430

127. Banerjee, A. G., Chowdhury, S., Losert, W. & Gupta, S. K. Survey on indirect optical manipulation of cells, nucleic acids, and motor proteins. *J. Biomed. Opt.* **16,** 51302 (2011).

128. Laza, S. C. *et al.* Two-photon continuous flow lithography. *Adv. Mater.* **24,** 1304–1308 (2012).

129. Dendukuri, D., Gu, S. S., Pregibon, D. C., Hatton, T. A. & Doyle, P. S. Stop-flow lithography in a microfluidic device. *Lab Chip* **7,** 818 (2007).

130. Paulsen, K. S., Di Carlo, D. & Chung, A. J. Optofluidic fabrication for 3D-shaped particles. *Nat. Commun.* **6,** 1–9 (2015).

131. Landenberger, B., Höfemann, H., Wadle, S. & Rohrbach, A. Microfluidic sorting of arbitrary cells with dynamic optical tweezers. *Lab Chip* **12,** 3177 (2012).

132. Tao Tao, T. T., Jing Li, J. L., Qian Long, Q. L. & Xiaoping Wu, X. W. 3D trapping and manipulation of micro-particles using holographic optical tweezers with optimized computer-generated holograms. *Chinese Opt. Lett.* **9,** 120010–120013 (2011).

133. Leach, J. *et al.* 3D manipulation of particles into crystal structures using holographic optical tweezers. *Opt. Express* **12,** 220–6 (2004).

134. Peng, T., Balijepalli, A., Gupta, S. K. & LeBrun, T. Algorithms for On-Line Monitoring of Micro Spheres in an Optical Tweezers-Based Assembly Cell. *J. Comput. Inf. Sci. Eng.* **7,** 330 (2007).

135. Wallen, S. P., Maznev, A. A. & Boechler, N. Dynamics of a monolayer of microspheres on an elastic substrate. *Phys. Rev. B* **92,** 174303 (2015).

136. Maruo, S., Ikuta, K. & Korogi, H. Submicron manipulation tools driven by light in a liquid. *Appl. Phys. Lett.* **82,** 133 (2003).

137. Grier, D. G. Optical tweezers in colloid and interface science. *Curr. Opin. Colloid Interface Sci.* **2,** 264–270 (1997).

138. Block, S. M., Blair, D. F. & Berg, H. C. Compliance of bacterial flagella measured with optical tweezers. *Nature* **338,** 514–518 (1989).

139. D'Helon, C., Dearden, E. W., Rubinsztein-Dunlop, H. & Heckenberg, N. R. Measurement of the optical force and trapping range of a single-beam gradient optical trap for micron-sized latex spheres. *J. Mod. Opt.* **41,** 595–601 (1994).

140. Friese, M. E. J., Rubinsztein-Dunlop, H., Heckenberg, N. R. & Dearden, E. W. Determination of the force constant of a single-beam gradient trap by measurement of backscattered light. *Appl. Opt.* **35,** 7112 (1996).

141. Malagnino, N., Pesce, G., Sasso, A. & Arimondo, E. Measurements of trapping efficiency and stiffness in optical tweezers. *Opt. Commun.* **214,** 15–24 (2002).

142. Ashkin, A. & Dziedzic, J. M. Optical levitation by radiation pressure. *Appl. Phys. Lett.* **19,** 283–285 (1971).

143. Ke, P. C. & Gu, M. Characterization of trapping force on metallic mie particles. *Appl. Opt.* **38,** 160–7 (1999).

144. Nieminen, T. a *et al.* Optical tweezers computational toolbox. *J. Opt. A Pure Appl. Opt.* **9,** S196–S203 (2007).

145. Ashkin, A. Forces of a single-beam gradient laser trap on a dielectric sphere in the ray optics regime. *Biophys. J.* **61,** 569–582 (1992).

146. Nieminen, T. a. *et al.* Tailoring Particles for Optical Trapping and Micromanipulation: An Overview. *PIERS Online* **4,** 381–385 (2008).

147. Beijersbergen, W. Orbital angular momentum of light and the transformation of Laguerre-Gaussian laser modes. **45,** (1992).

148. Derjaguin, B. & Landau, L. Theory of the stability of strongly charged lyophobic sols and

of the adhesion of strongly charged particles in solutions of electrolytes. *Prog. Surf. Sci.* **43,** 30–59 (1993).

149. Ball, R. C. & Melrose, J. R. A simulation technique for many spheres in quasi-static motion under frame-invariant pair drag and Brownian forces. *Phys. A Stat. Mech. its Appl.* **247,** 444–472 (1997).

150. Felgner, H., Müller, O. & Schliwa, M. Calibration of light forces in optical tweezers. *Appl. Opt.* **34,** 977–982 (1995).

151. Baek, J.-H., Hwang, S.-U. & Lee, Y.-G. Trap stiffness in optical tweezers. *Asian Symp. Precis. Eng. Nanotechnol.* **685,** 1100 (2007).

152. Hastie, T., Tibshirani, R. & Friedman, J. The elements of statistical learning. *Math. Intell.* **27,** 83–85 (2001).

153. Kumar, A. & Higdon, J. J. L. Origins of the anomalous stress behavior in charged colloidal suspensions under shear. *Phys. Rev. E - Stat. Nonlinear, Soft Matter Phys.* **82,** 1–7 (2010).

154. Verwey, E. J. W. Theory of the stability of lyophobic colloids. *J. Phys. Colloid Chem.* **51,** 631–636 (1947).

155. Reihani, S. N. S., Charsooghi, M. A., Khalesifard, H. R. & Golestanian, R. Efficient in-depth trapping with an oil-immersion objective lens. *Opt. Lett.* **31,** 766 (2006).

156. Reihani, S. N. S. & Oddershede, L. B. Optimizing immersion media refractive index improves optical trapping by compensating spherical aberrations. *Opt. Lett.* **32,** 1998 (2007).

157. Vermeulen, K. C., Wuite, G. J. L., Stienen, G. J. M. & Schmidt, C. F. Optical trap stiffness in the presence and absence of spherical aberrations. *Appl. Opt.* **45,** 1812–1819 (2006).

158. Fällman, E. & Axner, O. Influence of a Glass-Water Interface on the On-Axis Trapping of Micrometer-Sized Spherical Objects by Optical Tweezers. *Appl. Opt.* **42,** 3915–3926 (2003).

159. Mahmoudi, A. & Reihani, S. N. S. The effect of immersion medium in optical tweezers. *Opt. Express* **19,** 14794–14800 (2011).

160. Ghadiri, R., Weigel, T., Esen, C. & Ostendorf, A. Microassembly of complex and three-dimensional microstructures using holographic optical tweezers. *J. Micromechanics*

Microengineering **22,** 65016 (2012).

161. Won, J. *et al.* Photothermal fixation of laser-trapped polymer microparticles on polymer substrates. *Appl. Phys. Lett.* **75,** 1506 (1999).
162. Ghadiri, R., Surbek, M., Esen, C. & Ostendorf, A. Optically based manufacturing with polymer particles. *Phys. Procedia* **5,** 47–51 (2010).
163. Misawa, H., Sasaki, K., Koshioka, M., Kitamura, N. & Masuhara, H. Laser manipulation and assembling of polymer latex particles in solution. *Macromolecules* **26,** 282–286 (1993).
164. Mio, C. & Marr, D. W. M. Optical Trapping for the Manipulation of Colloidal Particles. *Adv. Mater.* **12,** 917–920 (2000).
165. Pauzauskie, P. J. *et al.* Optical trapping and integration of semiconductor nanowire assemblies in water. *Nat. Mater.* **5,** 97–101 (2006).
166. Rodrigo, P. J. *et al.* Optical microassembly platform for constructing reconfigurable microenvironments for biomedical studies. *Opt. Express* **17,** 6578–83 (2009).
167. Barner-Kowollik, C. & Junkers, T. Handbook of Vinyl Polymers: Radical Polymerization, Process, and Technology. *Macromol. Chem. Phys.* **210,** 1766–1766 (2009).
168. Ibrahim, A. *et al.* Investigation of termination reactions in free radical photopolymerization of UV powder formulations. *Eur. Polym. J.* **48,** 1475–1484 (2012).
169. Gómez, M. L., Montejano, H. A., del Valle Bohorquez, M. & Previtali, C. M. Photopolymerization of acrylamide initiated by the three-component system safranine/triethanolamine/diphenyliodonium chloride: The effect of the aggregation of the salt. *J. Polym. Sci. Part A Polym. Chem.* **42,** 4916–4920 (2004).
170. Ahmad, I. *et al.* Photoinitiated Polymerization of 2-Hydroxyethyl Methacrylate by Riboflavin/Triethanolamine in Aqueous Solution: A Kinetic Study. *ISRN Pharm.* **2013,** 1–7 (2013).
171. Dendukuri, D. *et al.* Modeling of Oxygen-Inhibited Free Radical Photopolymerization in a PDMS Microfluidic Device. *Macromolecules* **41,** 8547–8556 (2008).
172. Mahamdeh, M., Campos, C. P. & Schäffer, E. Under-filling trapping objectives optimizes the use of the available laser power in optical tweezers. *Opt. Express* **19,** 11759–11768 (2011).

173. LaFratta, C. N., Fourkas, J. T., Baldacchini, T. & Farrer, R. A. Multiphoton fabrication. *Angew. Chemie - Int. Ed.* **46,** 6238–6258 (2007).

174. Yuan, L. L. & Herman, P. R. Laser Scanning Holographic Lithography for Flexible 3D Fabrication of Multi-Scale Integrated Nano-structures and Optical Biosensors. *Sci. Rep.* **6,** 22294 (2016).

175. Shusteff, M. *et al.* Volumetric Additive Manufacturing of Polymer Structures.

176. Sun, H. B. & Kawata, S. Two-photon photopolymerization and 3D lithographic microfabrication. *Adv. Polym. Sci.* **170,** 169–273 (2004).

177. Bayindir, Z. *et al.* Polymer microcantilevers fabricated via multiphoton absorption polymerization. *Appl. Phys. Lett.* **86,** 1–3 (2005).

178. Baldacchini, T. *et al.* Acrylic-based resin with favorable properties for three-dimensional two-photon polymerization. *J. Appl. Phys.* **95,** 6072–6076 (2004).

179. Eckel, Z. C. *et al.* Additive manufacturing of polymer-derived ceramics. *Science (80-.).* **351,** 58–62 (2016).

180. Kurselis, K., Kiyan, R., Bagratashvili, V. N., Popov, V. K. & Chichkov, B. N. 3D fabrication of all-polymer conductive microstructures by two photon polymerization. *Opt. Express* **21,** 31029–35 (2013).

181. Fourkas, J. T. *et al.* Creation of multimaterial micro- and nanostructures through aqueous-based fabrication, manipulation, and immobilization. *SPIE Photonics West 2014-LASE Lasers Sources* **8970,** 89700M (2014).

182. Lee, M. P. *et al.* Development of a 3D printer using scanning projection stereolithography. *Sci. Rep.* **5,** 9875 (2015).

183. Laboratory, T. S. C. Human retinal engineering. at <http://www.tuckerlaboratory.org/Tissue Engineering>

184. Ruzin, S. Two-photon fluorescence microscopy. (2016). at <http://microscopy.berkeley.edu/courses/tlm/2P/index.html>

185. Slic3r: G-code generator for 3D printers. (2018). at <http://slic3r.org/>

186. Hatamizadeh, A., Song, Y. & Hopkins, J. B. Geometry Optimization of Flexure System Topologies Using the Boundary Learning Optimization Tool (BLOT). in *ASME IDETC* 1–

11 (2017).

187. Alderson, A. *et al.* An auxetic filter: A tuneable filter displaying enhanced size selectivity or defouling properties. *Ind. Eng. Chem. Res.* **39,** 654–665 (2000).

188. Rasburn, J. *et al.* Auxetic structures for variable permeability systems. *AIChE J.* **47,** 2623–2626 (2001).

189. Choi, J. B. & Lakes, R. S. Nonlinear properties of polymer cellular materials with a negative Poisson's ratio. *Mater. Sci.* **27,** 4678–4684 (1992).

190. Stavroulakis, G. E. Auxetic behaviour: appearance and engineering applications. *Phys. status solidi* **242,** 710–720 (2005).

191. Howell, B., Prendergast, P. & Hansen, L. Examination of acoustic behavior of negative poisson's ratio materials. *Appl. Acoust.* **43,** 141–148 (1994).

192. Scarpa, F., Ciffo, L. G. & Yates, J. R. Dynamic properties of high structural integrity auxetic open cell foam. *Smart Mater. Struct.* **13,** 49–56 (2004).

193. Meza, L. R., Das, S. & Greer, J. R. Strong, lightweight, and recoverable three-dimensional ceramic nanolattices. *Science (80-.).* **345,** 1322–6 (2014).

194. Nelson, T. G., Lang, R. J., Magleby, S. P. & Howell, L. L. Curved-folding-inspired deployable compliant rolling-contact element (D-CORE). *Mech. Mach. Theory* **96,** 225–238 (2016).

195. Kim, S.-H., In, H., Song, J.-R. & Cho, K.-J. Force characteristics of rolling contact joint for compact structure. in *6th IEEE Int. Conf. Biomed. Robot. Biomech.* 1207–1212 (2016). doi:10.1109/BIOROB.2016.7523795

196. Jiang, S. *et al.* Design colloidal particle morphology and self-assembly for coating applications. *Chem. Soc. Rev.* **46,** 3792–3807 (2017).

197. Bernard, A. B., Lin, C.-C. & Anseth, K. S. A Microwell Cell Culture Platform for the Aggregation of Pancreatic β-Cells. *Tissue Eng. Part C Methods* **18,** 583–592 (2012).

198. Horcajada, P. *et al.* Porous metal-organic-framework nanoscale carriers as a potential platform for drug deliveryand imaging. *Nat. Mater.* **9,** 172–178 (2010).

199. Appleyard, D. C., Chapin, S. C., Srinivas, R. L. & Doyle, P. S. Bar-coded hydrogel microparticles for protein detection: Synthesis, assay and scanning. *Nat. Protoc.* **6,** 1761–

1774 (2011).

200. Yıldırım, M., Sarılmaz, A. & Özel, F. Investigation of optical and device parameters of colloidal copper tungsten selenide ternary nanosheets. *J. Mater. Sci. Mater. Electron.* **29,** 762–770 (2018).

201. Champion, J. A., Katare, Y. K. & Mitragotri, S. Particle Shape: A New Design Parameter for Micro- and Nanoscale Drug Delivery Carriers. *J. Control Release* **121,** 3–9 (2014).

202. Madivala, B., Vandebril, S., Fransaer, J. & Vermant, J. Exploiting particle shape in solid stabilized emulsions. *Soft Matter* **5,** 1717 (2009).

203. Meiring, J. E. *et al.* Hydrogel biosensor array platform indexed by shape. *Chem. Mater.* **16,** 5574–5580 (2004).

204. Ksouri, S. I., Aumann, A., Ghadiri, R. & Ostendorf, A. Optical micro-assembling of non-spherical particles. **8637,** 86370Z (2013).

205. Benedikt, S. *et al.* Highly efficient water-soluble visible light photoinitiators. *J. Polym. Sci. Part A Polym. Chem.* **54,** 473–479 (2016).

206. Okubo, M., Konishi, Y. & Minami, H. Production of hollow polymer particles by suspension polymerization. *Colloid Polym. Sci.* **276,** 638–642 (1998).

207. Colver, P. J., Colard, C. A. L. & Bon, S. A. F. Multilayered Nanocomposite Polymer Colloids Using Emulsion Polymerization Stabilized by Solid Particles. *J. Am. Chem. Soc.* **130,** 16850–16851 (2008).

208. Abedin, R., Pojman, J. A., Knopf, F. C. & Rice, R. G. Suspended Droplet Polymerization in an Unstable, Vibrating Shallow-Bed Reactor. *Ind. Eng. Chem. Res.* **55,** 2493–2503 (2016).

209. Jiang, P., Bertone, J. F. & Colvin, V. L. A lost-wax approach to monodisperse colloids and their crystals. *Science (80-.).* **291,** 453–457 (2001).

210. Hernandez, C. J. & Mason, T. G. Colloidal alphabet soup: Monodisperse dispersions of shape-designed LithoParticles. *J. Phys. Chem. C* **111,** 4477–4480 (2007).

211. Rolland, J. P. *et al.* Direct fabrication and harvesting of monodisperse, shape-specific nanobiomaterials. *J. Am. Chem. Soc.* **127,** 10096–10100 (2005).

212. Merkel, T. J. *et al.* Using mechanobiological mimicry of red blood cells to extend

circulation times of hydrogel microparticles. *Proc. Natl. Acad. Sci.* **108,** 586–591 (2011).

213. Dendukuri, D., Pregibon, D. C., Collins, J., Hatton, T. A. & Doyle, P. S. Continuous-flow lithography for high-throughput microparticle synthesis. *Nat. Mater.* **5,** 365–369 (2006).

214. Chung, S. E. *et al.* Optofluidic maskless lithography system for real-time synthesis of photopolymerized microstructures in microfluidic channels. *Appl. Phys. Lett.* **91,** (2007).

215. Le Goff, G. C., Lee, J., Gupta, A., Hill, W. A. & Doyle, P. S. High-Throughput Contact Flow Lithography. *Adv. Sci.* **2,** 1–7 (2015).

216. Merkel, T. J. *et al.* Scalable, shape-specific, top-down fabrication methods for the synthesis of engineered colloidal particles. *Langmuir* **26,** 13086–13096 (2010).

217. Saha, S. K., Divin, C., Cuadra, J. A. & Panas, R. M. Effect of Proximity of Features on the Damage Threshold During Submicron Additive Manufacturing Via Two-Photon Polymerization. *J. Micro Nano-Manufacturing* **5,** 31002 (2017).

218. Fischer, J., Von Freymann, G. & Wegener, M. The materials challenge in diffraction-unlimited dired-laser-writing optical lithography. *Adv. Mater.* **22,** 3578–3582 (2010).

219. Song, Y., Panas, R. M. & Hopkins, J. B. A review of micromirror arrays. *Precis. Eng.* **51,** 729–761 (2018).

220. Numerical Aperture. at <https://www.microscopyu.com/microscopy-basics/numerical-aperture>

221. Gaussian Beam Optics. at <https://www.cvilaseroptics.com/file/general/All_About_Gaussian_Beam_OpticsWEB.pdf>

222. Technical Note: Gaussian Beam Optics. at <https://www.newport.com/n/gaussian-beam-optics>

223. Shanblatt, E. R. & Grier, D. G. Extended and knotted optical traps in three dimensions. *Opt. Express* **19,** 5833–5838 (2011).